

Swift/UVOT discovery of Swift J221951-484240: a UV luminous ambiguous nuclear transient

S. R. Oates^{1*}, N. P. M. Kuin², M. Nicholl^{3,1}, F. Marshall⁴, E. Ridley¹, K. Boutsia⁵, A. A. Breeveld², D. A. H. Buckley^{6,7,8}, S. B. Cenko^{4,9}, M. De Pasquale¹⁰, P. G. Edwards¹¹, M. Gromadzki¹², R. Gupta^{13,14}, S. Laha^{4,15,16}, N. Morrell⁵, M. Orìo^{17,18}, S. B. Pandey¹³, M. J. Page², K.L. Page¹⁹, T. Parsotan^{4,15,16}, A. Rau²⁰, P. Schady²¹, J. Stevens²², P. J. Brown²³, P.A. Evans¹⁹, C. Gronwall^{24,25}, J.A. Kennea²⁴, N.J. Klingler^{4,15,16}, M. H. Siegel²⁴, A. Tohuvavohu²⁶, E. Ambrosi²⁷, S.D. Barthelmy⁴, A.P. Beardmore¹⁹, M.G. Bernardini²⁸, C. Bonnerot¹, S. Campana²⁸, R. Caputo⁴, S. Cioi³⁰, G. Cusumano²⁷, A. D’Ai²⁷, P. D’Avanzo²⁸, V. D’Elia^{29,31}, P. Giommi³¹, D.H. Hartmann³², H.A. Krimm³³, D. B. Malesani^{34,35,36}, A. Melandri²⁹, J. A. Nousek²⁴, P.T. O’Brien¹⁹, J.P. Osborne¹⁹, C. Pagani¹⁹, D.M. Palmer³⁷, M. Perri^{31,29}, J. L. Racusin⁴, T. Sakamoto³⁸, B. Sbarufatti^{28,24}, J. E. Schlieder⁴, G. Tagliaferri²⁸, E. Troja^{39,40} & D. Xu^{40,41}

Accepted...Received...

ABSTRACT

We report the discovery of *Swift* J221951-484240 (hereafter: J221951), a luminous slow-evolving blue transient that was detected by the Neil Gehrels Swift Observatory Ultra-violet/Optical Telescope (*Swift*/UVOT) during the follow-up of Gravitational Wave alert S190930t, to which it is unrelated. *Swift*/UVOT photometry shows the UV spectral energy distribution of the transient to be well modelled by a slowly shrinking black body with an approximately constant temperature of $T \sim 2.5 \times 10^4$ K. At a redshift $z = 0.5205$, J221951 had a peak absolute magnitude of $M_{u,AB} = -23$ mag, peak bolometric luminosity $L_{max} = 1.1 \times 10^{45}$ erg s⁻¹ and a total radiated energy of $E > 2.6 \times 10^{52}$ erg. The archival *WISE* IR photometry shows a slow rise prior to a peak near the discovery date. Spectroscopic UV observations display broad absorption lines in NV and O VI, pointing toward an outflow at coronal temperatures. The lack of emission in the higher H Lyman lines, NI and other neutral lines is consistent with a viewing angle close to the plane of the accretion or debris disc. The origin of J221951 can not be determined with certainty but has properties consistent with a tidal disruption event and the turn-on of an active galactic nucleus.

Key words: gravitational waves, black hole physics, galaxies: nuclei, transients: tidal disruption events, ultraviolet: general

1 INTRODUCTION

The Advanced Laser Interferometer Gravitational Wave Observatory (LIGO; LIGO Scientific Collaboration; Aasi et al. 2015) and the Advanced Virgo detector (Virgo; the Virgo Scientific Collaboration; Acernese et al. 2015) began the third observing run (“O3”) in search of Gravitational Wave

(GW) events on 2019 April 1 (The LIGO Scientific Collaboration and the Virgo Collaboration. 2019). The Neil Gehrels Swift Observatory (henceforth *Swift*; Gehrels et al. 2004) participated in the search for the electromagnetic (EM) counterpart of GW sources. In total *Swift* observed, with varying degrees of coverage, 18 of the GW candidate alerts released by the LIGO-Virgo Collaboration (LVC). One effect of scanning very large areas of the sky for the EM counterpart is the discovery of a multitude of transient phe-

* E-mail: s.r.oates@bham.ac.uk

nomena that are not necessarily related to the GW itself. During the O3 run the *Swift* Ultra-violet/Optical Telescope (UVOT; 1600–8000 Å; Roming et al. 2005) serendipitously found 27 optical transients that changed in magnitude at 3σ level compared with archival *u* or *g*-band catalogued values (Oates et al. 2021). Determining the nature of all the optical/UV transients that reside in GW error regions is important to confirm or rule out their possible association with the GW trigger and these serendipitous UV sources detected may also be of interest in their own right. Indeed this is the case for *Swift* J221951-484240 (henceforth J221951; Oates et al. 2019a,b), which we investigate further in this paper. This source was observed by the *Swift*/UVOT telescope as part of the follow-up campaign to identify the EM counterpart to the GW trigger S190930t, which was initially classified as a neutron star - black hole (NS-BH) merger (LIGO Scientific Collaboration & Virgo Collaboration 2019).

Since detection, *Swift* has continued to monitor this source and we have obtained additional photometric and spectral observations with *HST* ACS+COS, SALT, Magellan/IMACS, VLT/X-shooter, ATCA, *AstroSat* and GROND. With the *HST* COS spectrum, we identify J221951 at a redshift of $z = 0.5205 \pm 0.0003$ (see §3.6), which is outside the distance range of the GW source reported on GraceDB, ruling out its association with S190930t. At this redshift it had a peak absolute magnitude of $M_{u,AB} = -23$ mag and total energy release in the optical/UV over the 2.5 years of observations of $> 2.6 \times 10^{52}$ erg, making it one of the most luminous transients ever recorded. In the following, we report on these observations and investigate the nature of this extremely luminous UV transient, ultimately comparing it to tidal disruption events (TDEs¹) and active galactic nuclei (AGN).

This paper is organized as follows. We provide the data analysis in § 2, results in § 3 and discussion and conclusions follow in § 4 and § 5. All uncertainties throughout this paper are quoted at 1σ unless otherwise stated. Throughout, we assume the Hubble parameter $H_0 = 70 \text{ km s}^{-1} \text{ Mpc}^{-1}$ and density parameters $\Omega_\Lambda = 0.7$ and $\Omega_m = 0.3$. All magnitudes are given in the AB system, except for *WISE* photometry which is provided in the Vega system.

2 OBSERVATIONS

S190930t triggered LIGO/Virgo at 14:34:08 UT on the 2019 September 30, $T_{0,GW}$ (LIGO Scientific Collaboration & Virgo Collaboration 2019). It was reported to be at a distance of 108 ± 38 Mpc, on GraceDB² using the BAYESTAR skymap. S190930t had a high false alarm probability of 2.05 yr^{-1} . At the time of the announcement, this trigger met the *Swift* follow-up criteria and *Swift*/UVOT observed 50.1 deg^2 , equating to 2 per cent of the total localization probability; determined from a convolution of the LIGO-Virgo probability map and the 2MASS Photometric Redshift catalogue (Bilicki et al. 2014; Evans et al. 2016). As this GW event was only detected by a single detector, this event did

not meet the criteria to be included in the Gravitational-Wave Transient Catalog (GWTC-2) of compact binary coalescences observed by Advanced LIGO and Advanced Virgo (Abbott et al. 2020).

J221951 was identified in the UVOT GW pipeline as a Q0 source³ and given the initial identification Q0_src93 (Oates et al. 2021). J221951 was detected at a *u*-band magnitude of 19.48 ± 0.20 mag at $T_{0,GW} + 14.37$ ks (Oates et al. 2019a). The UVOT position is RA, Dec(J2000) = $334.96599, -48.71116$ deg with an estimated uncertainty of 0.7 arcsec (radius, 90 per cent confidence). Examining archival images, no source was detected at the location in GALEX NUV or FUV images (Bianchi, Conti & Shiao 2014; Bianchi, Shiao & Thilker 2017). However, a faint source consistent with this position was identified in the DSS archival image and in the catalogues of the Dark Energy Survey (DES; Abbott et al. 2018, 2021), VISTA (McMahon et al. 2013) and *WISE* (Cutri & et al. 2012; Cutri et al. 2021). The source appears nuclear when comparing our ACS imagery (see below) to DES images going back to 2014.

Initially, it was suggested that this source was a flare of a red dwarf star (Oates et al. 2019a). However, follow-up observations, performed by UVOT at $T_{0,GW} + 2.1$ days (Oates et al. 2019b), showed the source was blue and at a magnitude consistent with the initial detection ($u = 19.67 \pm 0.22$). At the time of detection, follow-up observations were also performed by J-GEM (Kamei et al. 2019), Chilescope observatory (Belkin et al. 2019) and spectrally with SALT (Buckley et al. 2019). However, no spectral features could be identified and therefore the redshift of this source could not be constrained.

Below we summarize the archival data and the photometry and spectroscopy obtained for J221951. The photometry is provided in Fig. 1 and Supplementary Table S.1. A log of the spectroscopic observations is given in Table 1.

2.1 *Swift* BAT Observations

We analyzed all of the publicly available (on HEASARC⁴) BAT “survey” mode data, from 29th Oct 2019 to 21st April 2022, which are also known as detector plane histograms or DPHs. BAT survey data are accumulated in histograms onboard the spacecraft, with typical integration times of between 300 seconds and around 2000 seconds. An 80-channel binned spectrum is recorded for each of the active detectors, which are saved in the DPH files. For a detailed explanation of the reprocessing and analysis of the BAT survey mode data see Laha et al. (2022b). We do not detect a signal at the 3σ level above the background in any of the BAT exposures. Integrating from the time of detection until the last observation we find the average 5σ upper limit on the $14 - 195 \text{ keV}$ flux is $6 \times 10^{-9} \text{ erg cm}^{-2} \text{ s}^{-1}$.

¹ A TDE is a bright flare that arises as a consequence of a star being torn apart as it passes too close to the centre of a super-massive black hole (Hills 1975; Rees 1988; Loeb & Ulmer 1997).

² <https://gracedb.ligo.org/>

³ For a source to be given a Q0 identification it implies that in the detection image it must be brighter than 19.9 mag and is either a new source or a known source that is two magnitudes brighter than a catalogued value (see Oates et al. 2021, for further details on the *Swift*/UVOT GW pipeline and quality flags).

⁴ <https://heasarc.gsfc.nasa.gov/docs/archive.html>

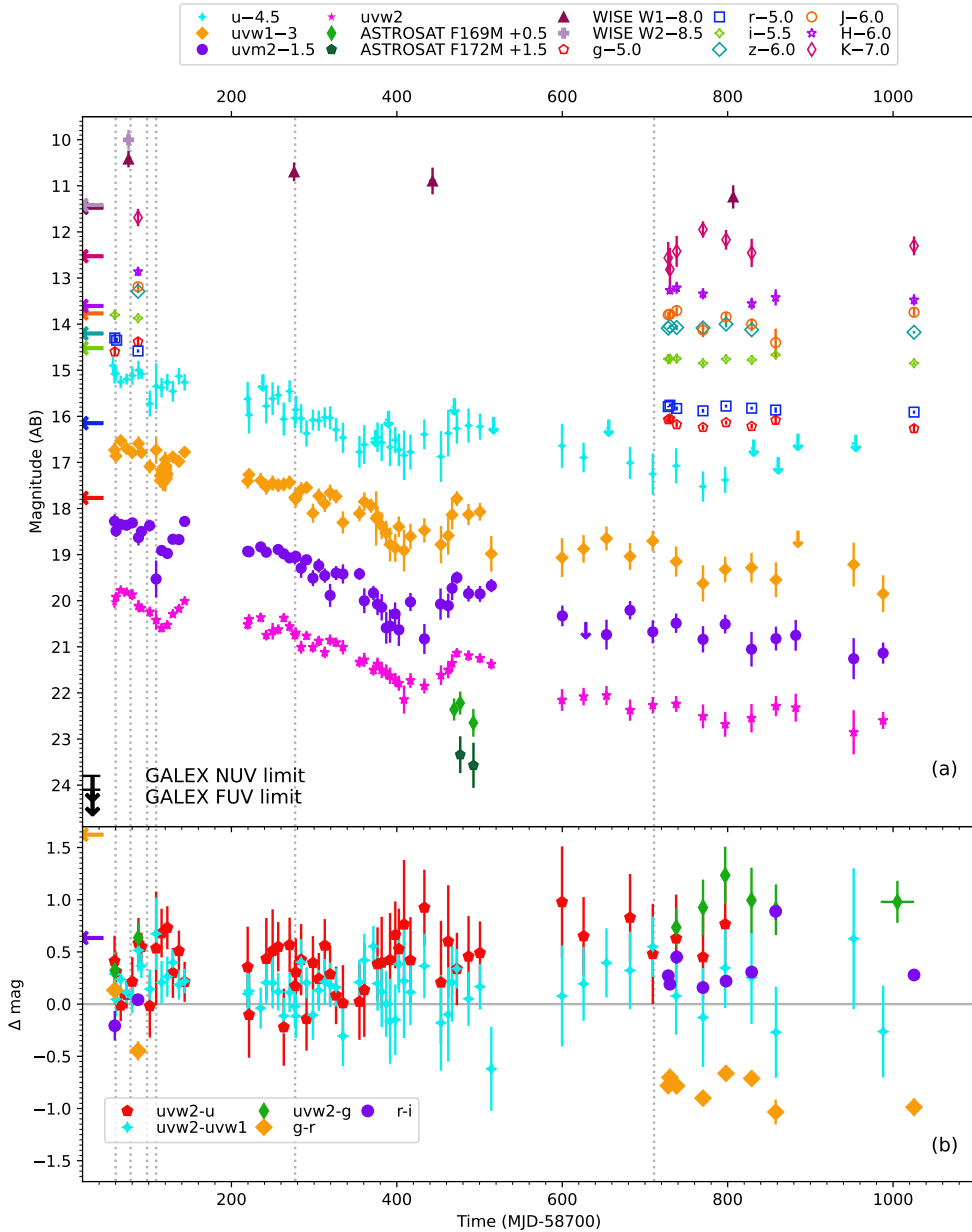


Figure 1. Panel (a) displays the 4 UVOT UV filter light curves of J221951 together with data from *AstroSat*, GROND, GALEX, *WISE*, J-GEM and Chilescope observatory; data from the latter two telescopes are from GCNs (Kamei et al. 2019; Belkin et al. 2019). The different filter light curves have been scaled, with the scaling given in the legend. No correction for Galactic extinction, corresponding to a reddening of $E(B - V) = 0.012$ (Schlafly & Finkbeiner 2011) has been applied. Upper limits for the GALEX FUV and NUV observations are given by black down-pointing arrows. Included as left pointing arrows are the archival detections for the different filters, obtained from DES, VISTA and *WISE*. No correction has been made to the photometry of J221951 for this archival source. The dotted vertical lines indicate the times at which spectra were taken. The light curve shows a gradual decrease in brightness over the course of observations. The light curve brightens three times (~ 58766 , 58843 and 59172 MJD), which appear to reset the brightness level. At peak J221951 is brighter than archival values at all UV/optical/IR wavelengths, by more than 1-3 mag. Superimposed on the decay, most apparent in the *uvw2* light curve, are three rebrightenings which show changes in magnitude of ~ 0.5 mag, after which, the light curve continues to decay but at an elevated brightness compared to that pre-brightening. Panel (b) displays the change over time of 5 different colours, which are given in the legend. The colour curves have been corrected for Galactic extinction and host subtracted. The left-pointing arrows indicate archival colours. Compared to historic values J221951 is much bluer, changing in $g - r$ by -0.68 mag by the first observation. Within errors, $uvw2 - uvw1$ is constant in colour, while $g - r$ and $r - i$ become bluer and $uvw2 - g$ becomes redder with time.

2.2 *Swift*/XRT Observations

We processed the XRT data using the online analysis tools provided by the UK *Swift* Science Data Centre (Evans et al. 2007, 2009). J221951 is not detected in single visits or in a stacked image created from the 279 ks of observations taken over 2.5 years, from 2019 Sep 30 to 2022 Apr 21. Individual visits are typically of a few ks duration, with limiting count rates of $(2 - 3) \times 10^{-3}$ counts s^{-1} (0.3-10 keV). This is equivalent to an unabsorbed flux density of $< 1 \times 10^{-13}$ erg cm^{-2} s^{-1} and luminosity $< 10^{44}$ erg s^{-1} in the 0.3-10 keV energy range, assuming a photon index of $\Gamma = 1.7$, a Galactic absorbing column $N_H = 9.8 \times 10^{19}$ cm^{-2} and an intrinsic absorbing column of $N_H = 3 \times 10^{20}$ cm^{-2} . Stacking all the XRT images, we find a deeper limiting count rate of 1.4×10^{-4} counts s^{-1} (0.3-10 keV), in 279 ks, equivalent to an unabsorbed flux density of $< 5.5 \times 10^{-15}$ erg cm^{-2} s^{-1} and a luminosity of $L_X < 6 \times 10^{42}$ erg s^{-1} . Assuming this limit over the duration of *Swift* observations this places an upper limit on the total energy released in X-rays (0.3-10 keV) as $E_X < 5 \times 10^{50}$ erg.

2.3 *Swift*/UVOT Observations

After the detection of J221951 in the *u* band on 2019 September 30, UVOT continued to observe J221951 in all six optical/UV filters until 2021 Aug 11, after which observations were performed in the *u* and UV filters. Observations were taken in image mode only. To begin with, observations were performed every few days to a week cadence, which decreased to approximately a monthly cadence as the source faded. On the 3rd of December 2020, we observed with a higher cadence to investigate variability. All images were downloaded from the *Swift* data archive⁵. The source counts were extracted from single or summed exposures using a source region of 5 arcsec radius. Background counts were extracted using an annular region with an inner radius of 15 arcsec and an outer radius of 35 arcsec. The count rates were obtained from the images using the *Swift* tool UVOTSOURCE. Finally, the count rates were converted to AB magnitudes using the UVOT photometric zero-points (Poole et al. 2008; Breeveld et al. 2011). The analysis pipeline used UVOT calibration 20201215. The UVOT detector is less sensitive in a few small patches⁶ for which a correction has not yet been determined. Therefore, we have checked to see if any of the sources of interest fall on any of these patches in any of our images and exclude 15 individual UV exposures for this reason.

2.4 Dark Energy Survey

DES (Abbott et al. 2018) observed the field of J221951 over several occasions in the *g*, *r*, *i*, *z* and *Y* filters, starting November 2013. Images from 2013 until 2018 are available for J221951 in NOIRLab Astro Data Lab⁷.

We used a custom wrapper for PHOTUTILS to perform

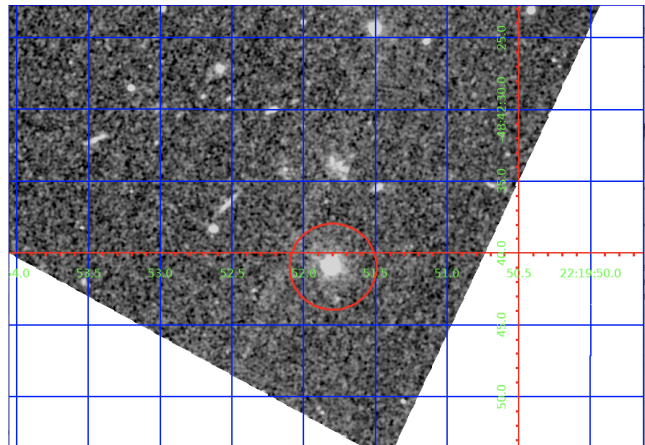


Figure 2. *HST* ACS image of J221951. J221951, indicated by a red circle, is consistent with being a point source.

both aperture and point spread function (PSF) fitting photometry at the location of J221951 in these DECam images, finding consistent results between the two approaches. We calibrated the zeropoint of each image using local stars in the Pan-STARRS DR2 catalogue (Flewelling et al. 2020). At the location of J221951, a red point-like source is well detected in all epochs taken prior to the detection of J221951 by UVOT. The source shows no significant temporal variability.

2.5 HST COS & ACS

We observed J221951 with the Cosmic Origins Spectrograph (Green, Wilkinson & Morse 2003; Dixon & Niemi 2010) on the Hubble Space Telescope (Bahcall 1986) on the 8th May 2020. In two orbits we obtained medium resolution spectra with the G130M and G140L gratings (program ID 16076, P.I. S. Oates). The spectra were processed with the standard pipeline (OPUS_VER=HSTDP 2020_5; calibration software system version caldp_20201012; and CALCOS code version 3.3.10) on MJD 59139.38. The spectra were spliced together using the IRAF ‘splice’ task. We also obtained an image, split in 4 exposures, with the Advanced Camera for Surveys (Clampin et al. 2000) (total exposure time = 2256 s) during one orbit using the F475W filter (4746 Å; width 420 Å) which led to an improved position for J221951 of RA=22:19:51.80, Dec=-48:42:40.90 (J2000), Fig. 2. The source magnitude was $M(F475W) = 20.255 \pm 0.002$ mag. Standard observation and processing were used. We investigated if the source was nuclear by comparing to DES DECam “Resampled” images in *g*, *r*, *z* and *Y* bands from 2014 onward by overlaying the ACS. We find that J221951 is centred on the nucleus in DECam to within 0.045 arcsec (3-sigma) which is equivalent to an angular separation of < 0.3 kpc.

2.6 GROND

On 2019 October 31, *g'r'i'z'JHK* observations of J221951 were taken with the Gamma-Ray Optical/Near-infrared Detector (GROND; Greiner et al. 2008) mounted on the MPG 2.2m telescope at the ESO La Silla observatory, Chile. The

⁵ <https://www.swift.ac.uk/archive/index.php>

⁶ https://heasarc.gsfc.nasa.gov/docs/heasarc/caldb/swift/docs/uvot/uvotcaldb_sss_01b.pdf

⁷ <https://datalab.noirlab.edu/>

source was re-observed with GROND on a further seven occasions between August and December of 2021, and again in May 2022. The data were reduced and analysed with the standard tools and methods described in Krühler et al. (2008). The optical and NIR magnitudes were obtained using aperture photometry and absolute calibration was performed using field stars within the GROND field of view covered by the Sky Mapper Southern Sky Survey (Keller et al. 2007) and the Two Micron Sky Survey (2MASS; Skrutskie et al. 2006) for the $g'r'i'z'$ and the JHK bands respectively.

2.7 AstroSat

The Ultra-violet Imaging Telescope (UVIT) onboard *AstroSat* (Pati et al. 2003) observed J221951 thrice on the 16th November 2020, 23rd November 2020, and a few days later on the 9th December 2020 (proposal ID A10.024, P.I. S. B. Pandey). Observations were taken with the F169M Sapphire (central wavelength of $\lambda = 1608\text{\AA}$, and width $\Delta\lambda = 290\text{\AA}$) and F172M Silica (central wavelength of $\lambda = 1717\text{\AA}$, and width $\Delta\lambda = 125\text{\AA}$) filters, respectively. We aligned the images by comparing field stars against those also found in GALEX FUV images. We performed the aperture photometry on Level 2 UVIT images to extract the source brightness. We used the standard zero points provided in Tandon et al. (2017). J221951 was detected at all three epochs (see Fig. 1).

2.8 SALT

The South African Large Telescope (SALT; Buckley, Swart & Meiring 2006) using the Robert Stobie Spectrograph (RSS, Burgh et al. 2003) obtained several spectra with the PG0300 grating starting 2019 October 4 (1800 s), then 2019 October 22 (2×1200 s), and on 2020 May 11 (1500 s); the latter on the same day of the *HST* COS observation though with full moon. The mean resolving power of $R \sim 420$ (14.8 \AA resolution). To reduce the spectra we used the PyRAF-based PySALT package (Crawford et al. 2010)⁸, which includes corrections for gain and cross-talk, and performs bias subtraction. We extracted the science spectrum using standard IRAF⁹ tasks, including wavelength calibration (Argon calibration lamp exposures were taken, one immediately before and one immediately after the science spectra), background subtraction, and 1D spectra extraction. Due to the SALT design, absolute flux calibration is not possible¹⁰. However, by observing spectrophotometric standards during twilight, we were able to obtain relative flux calibration, i.e. allowing recovery of the correct spectral shape and relative line strengths.

⁸ <https://astronomers.salt.ac.za/software/>

⁹ <https://iraf-community.github.io/>

¹⁰ The pupil (i.e. the view of the mirror from the tracker) moves during all SALT observations, causing the effective area of the telescope to change during exposures. Therefore, absolute flux calibration cannot be done. See Buckley et al. (2006) and Crawford et al. (2010) for details.

2.9 Las Campanas Observatory

On 2019 November 11 a low-resolution spectrum was taken, consisting of 2×1200 s exposures in the range 3700-9250 \AA , using the IMACS instrument on the Baade Telescope of Las Campanas Observatory. The S/N at 1.16 $\text{\AA}/\text{pix}$ resolution is low, 5-6, and there is a gap between 6430 \AA and 6524 \AA due to the location of the spectrum on the detector, which lies across two of the eight CCDs. The spectrum is blue and fairly featureless. Calibration was done using a standard star spectrum.

2.10 ATCA

On 2020 Jan 11, we observed the source position with the Australia Telescope Compact Array (ATCA), which consists of six 22 m diameter dishes (Wilson et al. 2011). Observations, made under project code C1730, were made when the telescope was in its 6A array configuration, with a maximum baseline of 5.9 km. The observing bands were centred at 5.5 and 9.0 GHz, with a 2 GHz bandwidth in both bands. Four 10-minute scans of J221951 were made, with each scan bookended by 2.5 minute scans on the phase calibrator PKS 2204-540. PKS 1934-638 was used as the primary flux density calibrator. Data reduction was carried out following the standard procedures in miriad (Sault, Teuben & Wright 2011, 1995). No source was detected at the position of J221951 with 3σ upper limits of 117 μJy at 5.5 GHz and 90 μJy at 9 GHz. Assuming a flat spectrum, the 5.5 GHz flux is equivalent to a luminosity of $\sim 2 \times 10^{39}$ erg s⁻¹, across a bandwidth of 2 GHz.

2.11 GALEX

GALEX observed the field of J221951 6 times in the NUV and 4 times in the FUV between 2004 and 2008 for a total of 2.5 ks and 2.6 ks. No source is detected in either band at the location of J221951. Using the Galex Merged catalog of sources (MCAT; Morrissey et al. 2007) we derive 3σ magnitude upper limits in the NUV and FUV of 23.8 and 24.1, respectively. For comparison, the *GALEX* NUV filter spans 1771-2831 \AA , which is broader than the individual UVOT UV filters. The NUV filter covers a similar wavelength range as the UVOT's *uvw1* and *uvm2* filters. The FUV filter spans 1344-1786 \AA , which is bluer than UVOT *uvw2*.

2.12 WISE

In the ALLWISE catalogue (Cutri et al. 2021) a source is detected within 1.6 arcsec in the W1 and W2 filters only, with non-detections in the W3 and W4 filters (W1 = 16.90, W2 = 16.78, W3 > 12.47, W4 > 9.12). *WISE/NEOWISE* (Wright et al. 2010; Mainzer et al. 2011) has been observing the field of J221951 biannually since May 2014. At the time of writing, the most recent data release provides observations until October 2021. We obtained photometry for the individual exposures from the IRSA/IPAC infrared data science archive. The individual images during a single visit are taken within a 1-2 day period. A weak source is detected at the location of J221951 in most of the W1 images. In W2, a weak source is detected in approximately half of the exposures. In the single exposure photometry, there appears to be

a slight increase in flux in observations taken between 2019 October 18 and 2019 October 21 close to the time J221951 was detected by *Swift*/UVOT, however, the data are noisy. We, therefore, used the coadder tool¹¹ to produce stacked images. We used *SEXTRACTOR* (Bertin & Arnouts 1996) to obtain the photometry. We display all the *WISE* visits in Fig. 3. We created a stack of the W1 and W2 images taken from May 2010 until May 2014 and measure a magnitude of 16.81 ± 0.10 and 16.61 ± 0.30 , in W1 and W2, respectively, consistent with that reported in the ALLWISE catalogue (Cutri et al. 2021). In a stack of the October 2019 observations, the first *WISE* visit after J221951 was detected by UVOT, the source is 1.1, and 1.4 magnitudes brighter in the W1 and W2 filters, respectively, compared to the stacks of the data taken prior to May 2014. J221951 is not detected in later W2 per visit stacks. In W1 it fades in the first 6 months by ~ 0.3 magnitudes and by October 2021 is consistent with pre-2014 level.

2.13 X-shooter

We observed J221951 with the X-shooter echelle spectrograph (Vernet et al. 2011), mounted on the European Southern Observatory (ESO) Very Large Telescope, on 16th July 2021 (PI Oates, program ID 107.22RT). X-shooter provides continuous coverage from $\approx 3000 - 25000 \text{ \AA}$ in the observer frame. Data were obtained in on-slit nodding mode and reduced using the ESO REFLEX pipeline. The pipeline applies de-biasing, flat-fielding, geometric transformations of the echelle orders, wavelength calibration, cosmic ray removal, and extraction to a one-dimensional spectrum. Flux calibration is achieved using standard star observations in the same setup.

3 RESULTS

3.1 Temporal Evolution

In the top panel of Fig. 1, we display the IR/optical/UV photometry of J221951 obtained by UVOT (only the 3 UV and *u* filters are displayed), GROND, *AstroSat*, *WISE*, J-GEM and the Chilescope observatory (the latter two from GCNs; Kamei et al. 2019; Belkin et al. 2019) along with archival values obtained with *GALEX*, DES and *WISE*. Overall, the light curve shows a gradual decrease in brightness with time. In addition to the decaying nature of the light curve, there are three rebrightenings (~ 58766 , 58843 and 59172 MJD) which show changes in magnitude of ~ 0.5 mag and which appear to reset the brightness level. The light curve continues to decay from the peak of the flare, rather than returning to the value expected from the extrapolation of the power-law observed pre-flare. These flaring episodes are most clearly observed in the *uvw2* filter. The long-term light curve of J221951, including photometry taken pre-and post-UVOT detection, is displayed in Fig. 3. At peak J221951 is brighter than archival values at all UV/optical/IR wavelengths, by more than 1-3 mags, with the largest change observed in the blue filters. There is some marginal evidence to

suggest the rise of the optical/UV emission lags the IR emission, though this cannot be claimed with certainty due to the lack of optical/UV emission between 58429 and 58759 MJD. The most recent observations, around 1000 days after the initial detection, indicate J221951 continues to be brighter than archival values in the UV through to the *r*-band, while in redder filters, J221951 is comparable in brightness with historic values.

The start time of J221951 is uncertain, but constraints can be placed using individual DES, J-GEM *i* band measurements. The last visit by DES taken in November 2018 is at a brightness consistent with historic values, suggesting J221951 began no earlier than 10 months prior to September 2019 (see Fig. 3). This implies the start time T_0 is within a ~ 330 day window between 58429 and 58759 MJD. For comparison with other types of objects, we will take the mid-time of this range, 58594 MJD, as T_0 .

Using T_0 as the start time, we fit the *uvw2* count rate (CR) light curve, with a series of functions of increasing complexity. We initially fit a power-law ($CR = Nt^\alpha$, where N is the normalisation, and α is the temporal decay index), which gives $\alpha = -1.32 \pm 0.06$, although the fit is poor with $\chi^2/d.o.f = 286/62$. With a broken power-law (two power-laws connected by a break at t_{break}), the fit traces the general underlying behaviour. The fit has improved, but the $\chi^2/d.o.f$ is still poor with $\chi^2/d.o.f = 229/60$. An F-test suggests the break is required with a confidence of 3σ . The broken power-law fit has parameters $\alpha_1 = -0.84^{+0.17}_{-0.09}$, the break time $t_{break} = 58935^{+30}_{-18}$ MJD and $\alpha_2 = -1.82 \pm 0.15$. The poor $\chi^2/d.o.f$ is likely due to the rebrightenings, which appear to reset the brightness level. The uncertainty on the T_0 will also affect our estimate of the decay indices of the fits. For instance setting T_0 as $T_{0,GW}$ and fitting a power-law results in an $\alpha = -0.39 \pm 0.01$, but with a much worse $\chi^2/d.o.f = 847/62$.

In the bottom panel of Fig. 1 we display the colour evolution. The *uvw2* – *uvw1* and *uvw2* – *u* colours do not show strong evolution with time although there is some variation, which appears to correspond to the peaks and troughs of the light curve behaviour in the panel above. However, the error bars are large compared to the colour curves built with the ground-based data. For the *uvw2* – *g*, *g* – *r*, *r* – *i* we notice there is a strong change in colour between the first two data points, becoming redder for *uvw2* – *g* and *r* – *i*, but bluer for *g* – *r*. There is a gap in these colour curves, until 59420 MJD, after which the colour curves remain approximately at the same level until the end of observations, however, this level is slightly redder for *uvw2* – *g* and *r* – *i* and slightly bluer for *g* – *r*, compared to the last data point before the gap. Also shown in Fig. 1 is the archival *g* – *r* colour (indicated by an arrow). Compared to historic values J221951 has become bluer, changing in *g* – *r* by -0.68 mag by the first observation post-detection.

The *WISE* W1 – W2 colour changes from 0.20 ± 0.32 pre-outburst to 0.56 ± 0.28 near the peak. The W1 – W2 has been used to provide a rough assessment of the AGN or stellar dominance of a galaxy ($W1 - W2 > 0.8$ for AGN-like or $W1 - W2 < 0.5$ for galaxy-like; Stern et al. 2012; Yan et al. 2013). A value of 0.20 mag is consistent with being galaxy-like and not dominated by an AGN. The change to 0.56 at peak, suggests that the surrounding dust is being heated, but W1 – W2 is still less than that observed in AGN.

¹¹ <https://irsa.ipac.caltech.edu/applications/ICORE/>

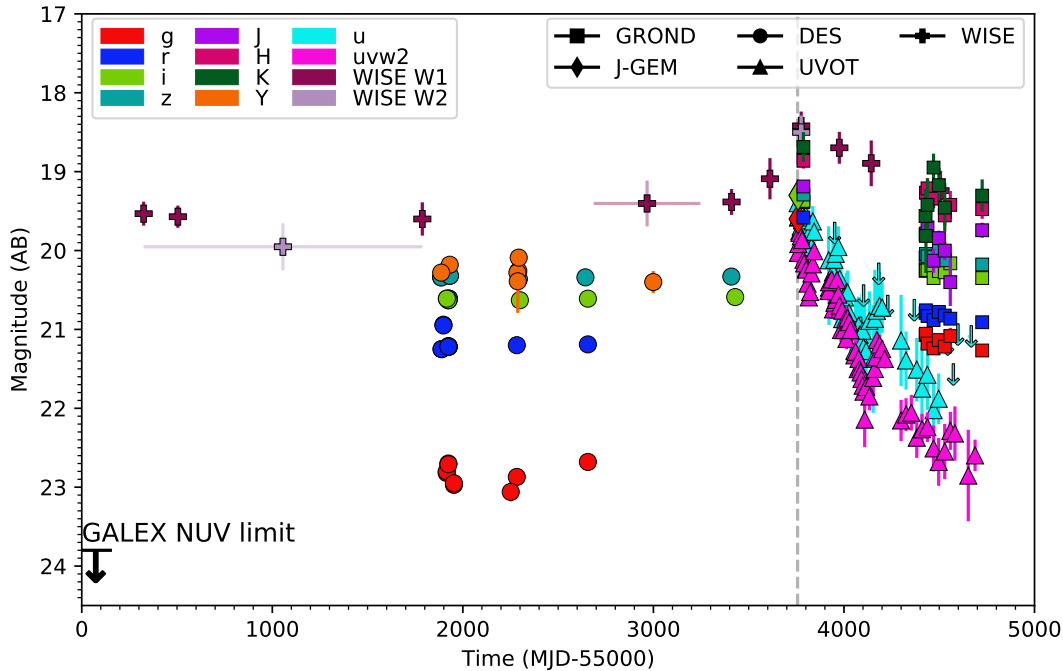


Figure 3. Long term light curve of J221951 containing data from DES, *WISE*, GROND, UVOT and J-GEM. The grey dotted line represents $T_{0,GW}$, the trigger time of the gravitational wave event S190930t. The *GALEX* observations took place between 53248 MJD and 54679 MJD (August 2004 and July 2008).

Table 1. Log of the spectroscopic observations

UT Start	Time (MJD)	Telescope	Instrument	Grating	Exposure Time (s)
2019-10-04	58760	SALT	RSS	PG0300	1800
2019-10-22	58778	SALT	RSS	PG0300	2×1200
2019-11-11	58798	Magellan-Baade	IMACS	Spectroscopic2/Gri-300-17.5	2×1200
2019-11-22	58809	SALT	RSS	PG0300	1600
2020-05-08	58977	SALT	RSS	PG0300	1500
2020-05-08	58977	<i>HST</i>	COS/FUV	G140L	300
2020-05-08	58977	<i>HST</i>	COS/FUV	G130M	2275
2021-07-15	59411	VLT	X-shooter	UVB,VIS,NIR	2500,2400,2600

In Fig. 4, we compare the $u - g$, $g - r$ and $r - i$ colours determined from archival photometry and the photometry taken during the evolution of J221951. The $u - g$ vs $g - r$ colour evolves downwards with time, while the $g - r$ vs $r - i$ colour moves towards the top left corner with time. In both instances, the strongest colour evolution is observed in the first few days after detection. Initially, the colour of the transient is similar to that of the candidate AGN from Oates et al. (2021) and quasars (QSOs) and it changes in colour away from these objects as it evolves with time. Note there is a substantial gap in GROND observations and so we only have colour information in these panels from observations at very early and very late times.

3.2 Spectral Energy Distributions

We also constructed spectral energy distributions (SEDs) for 8 epochs where we have quasi-simultaneous data from facilities in addition to *Swift*. To each data point of each

SED, which includes UVOT and ground observations we add a 5% systematic error. We fit the SEDs with XSPEC version 12.12.0 (Arnaud 1996). In these SEDs, we use host subtracted photometry, with the host values taken as the archival DES, VISTA and *WISE* values. The UVOT data are not host subtracted; this is reasonable given that J221951 is > 1 magnitude brighter than the underlying host galaxy in the redder g-band at all epochs and similarly J221951 is brighter than the NUV *GALEX* limit of 23.7 by > 1 mag at all epochs. Two of the SEDs were built using values from GCNs, *gri* for 58758 MJD (Kamei et al. 2019) and *r* for 58760 MJD (Belkin et al. 2019). For the *gri* filters in the SED at 58758 MJD, we assume an error of 0.1 mag since photometric errors are not provided in Kamei et al. (2019). The remaining 6 SEDs were built using the optical/UV UVOT filters and GROND filters. For the MJD 58787 SED, we also include host subtracted *WISE* W1 and W2 photometry. We fit each SED with a power-law and then with a single blackbody. In both cases, we include a dust compo-

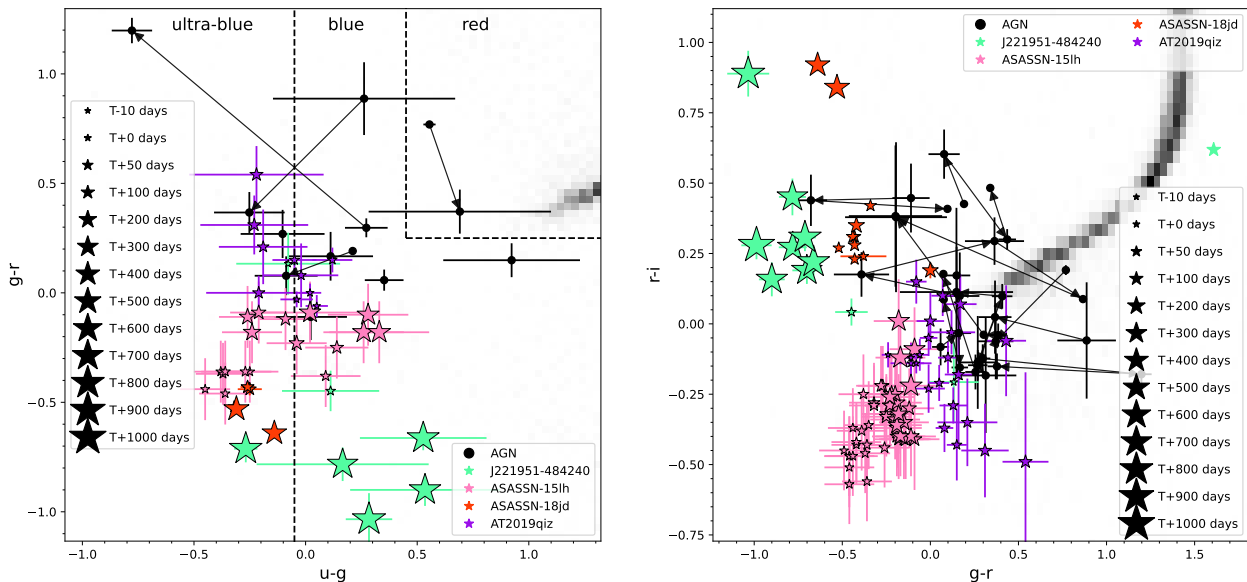


Figure 4. Colour-colour diagram of the photometry of J221951, together with ambiguous nuclear transients (ANTs) ASASSN-15lh (Leloudas et al. 2016) and ASASSN-18jd (Neustadt et al. 2020), a classic tidal disruption event AT2019qiz (Nicholl et al. 2020b) and the UV transient sources followed-up by *Swift*/UVOT during the O3 follow-up and identified as candidate AGN, see Oates et al. (2021). Left: $u-g$ versus $g-r$. Right: $g-r$ versus $r-i$. In both panels, the size of the markers for the black-edged data points indicates the time since peak or time since discovery in days, the key is given in the legend. For J221951, we use the time since UVOT discovery, MJD 58756. For the AGN arrows connect points of the same source in chronological order. In the left panel, the dotted lines divide the figure into regions identifying objects as red, blue and ultra-blue, adapted from Lawrence et al. (2016). In both panels, the grey region indicates the colour location of 90 per cent of SDSS spectroscopic quasars (see Lawrence et al. 2016, for details), and we display a 2-D histogram, given in grey, of the SDSS colours of 10,000 stars from the *Gaia* DR2 catalogue, selected from a region at high Galactic latitude. In the right panel, the blue region represents the location of the blue cloud galaxies, and the red region represents the red sequence galaxies, both out to $z = 0.22$ (adapted from Lawrence et al. 2016). The green star, without a black edge, in the right-hand panel (on the right-hand side of the figure) is the pre-outburst colour of J221951 and represents the colour of the host galaxy. All the other gri values have been host corrected. All values have been corrected for Galactic extinction. We have not corrected for host extinction. Correction for host extinction would move points down and to the left in both panels.

ment with Galactic reddening of $E(B-V) = 0.012$ (Schlafly & Finkbeiner 2011). We tested whether a host extinction component improved the fits. The host $E(B-V)$ was consistent with zero, similar to that derived from the X-shooter spectrum. The X-shooter spectrum does not display a dip at 2175 \AA in the rest-frame, implying that either the object has a Small Magellanic Cloud type extinction law without extra absorption at 2175 \AA or a very low $E(B-V)$ of the host. We, therefore, do not use a second dust component in our SED modelling.

For the first 3 SEDs, a power-law is preferred over a single blackbody, while for the latter 5 epochs, a single blackbody is preferred. However, the $\chi^2/d.o.f$ for both the power-law and single blackbody fits for the SEDs from MJD 58787 (the third SED) onwards were poor. We therefore also tried fitting a model consisting of two blackbodies. For the MJD 58787 SED, this model is marginally preferred over the single power-law at 2.5σ . For the subsequent SEDs, the two blackbody model does not provide a better fit. We note that by these late epochs, the brightness of J221951 in the reddest filters is comparable to the host making it difficult to constrain the second blackbody component. In Fig. 5, we display the SEDs of MJD 58787 and MJD 59437, together with the

three models. The necessity of two blackbody components for the MJD 58787 SED is apparent. For the MJD 59437 SED, the H-band data point is well above the extrapolation of the single component blackbody model, suggesting that the second thermal component is required. The temperature of the second component decreases with time. The spectral fits are provided in Table 2, with the convention for flux density, $F \propto \nu^{-\beta}$.

We also constructed SEDs using UVOT data only for each observation performed by *Swift*/UVOT for which at least three filters were obtained. We fit two simple models to each UVOT SED: a power-law and a blackbody, again including in both instances a dust component with Galactic reddening. From 64 SEDs, we find a weighted average index of $\beta = 0.49 \pm 0.04$, which is 4σ shallower than the $\beta = 2/3$ predicted for a standard thin accretion disc at UV/optical wavelengths (Shakura & Sunyaev 1973). For the blackbody fits the average temperature is $23000 \pm 410 \text{ K}$. The mean and standard deviation of the $\chi^2/d.o.f$ of the power-law fits and the blackbody fits is 0.80 ± 0.65 and 0.89 ± 0.62 , respectively.

Table 2. The best-fit parameters to eight SEDs with ground-based photometry in addition to 6 filter UVOT photometry. The parameters given are: spectral index β , intrinsic blackbody temperature T_{BB} and the $\chi^2/d.o.f.$

Time (MJD)	Model	β	$T_{BB,1}$ (K)	$T_{BB,2}$ (K)	$\chi^2/d.o.f.$	Null Hypothesis
58758	Pow	0.19 ± 0.10	-	-	5/7	6.1×10^{-1}
58758	Bbody	-	21300 ± 1000	-	7/7	4.3×10^{-1}
58760	Pow	0.25 ± 0.10	-	-	2/5	8.1×10^{-1}
58760	Bbody	-	21100 ± 1000	-	7/5	1.9×10^{-1}
58787	Pow	0.03 ± 0.06	-	-	35/11	2.2×10^{-4}
58787	Bbody	-	20200 ± 700	-	38/11	6.8×10^{-5}
58787	Bbody Bbody	-	20800 ± 700	2800 ± 400	13/9	1.6×10^{-1}
59437	Pow	0.12 ± 0.12	-	-	29/11	2.2×10^{-3}
59437	Bbody	-	20500 ± 1100	-	18/11	8.7×10^{-2}
59437	Bbody Bbody	-	20700 ± 1200	2300 ± 500	15/9	1.0×10^{-1}
59470	Pow	0.15 ± 0.14	-	-	51/9	6.4×10^{-8}
59470	Bbody	-	19400 ± 1300	-	36/9	4.4×10^{-5}
59470	Bbody Bbody	-	19500 ± 1300	1200 ± 100	28/7	2.2×10^{-4}
59497	Pow	0.33 ± 0.11	-	-	46/8	1.9×10^{-7}
59497	Bbody	-	18300 ± 1000	-	22/8	5.2×10^{-3}
59497	Bbody Bbody	-	18300 ± 1000	580 ± 50	20/6	2.8×10^{-3}
59528	Pow	0.12 ± 0.13	-	-	46/9	6.9×10^{-7}
59528	Bbody	-	18900 ± 1200	-	21/9	1.1×10^{-2}
59558	Pow	0.12 ± 0.13	-	-	46/9	6.9×10^{-7}
59558	Bbody	-	18900 ± 1200	-	21/9	1.1×10^{-2}

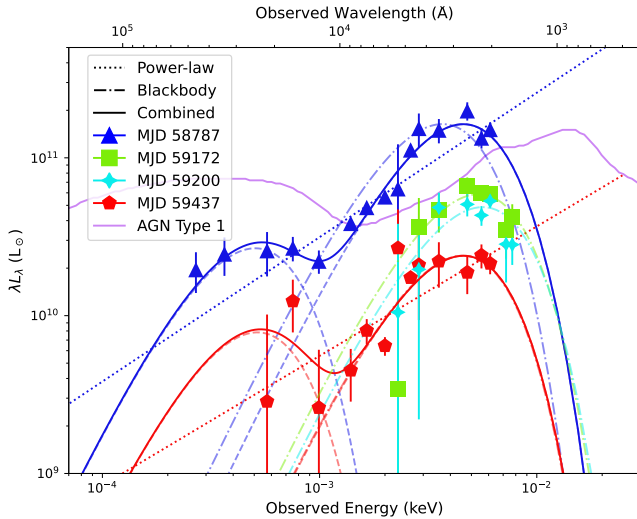


Figure 5. Spectral energy distributions of J221951 at MJD 58787 (blue), MJD 59172 (green), MJD 59200 (cyan) and MJD 59437 (red). For the MJD 58787 and MJD 59437 we overlay three models: power-law (dotted), single blackbody (dot-dashed) and two blackbodies (dashed and solid lines). For the two blackbody model we display the two single blackbodies (dashed) and the combination of these components (solid). A two blackbody model is the best fit for the MJD 58787 SED. Visually a two blackbody appears to be the best fit for the MJD 59437 SED, although is not statistically required. The MJD 59172, MJD 59200 SEDs include *AstroSat* data and show the turnover of the higher temperature black body. We only overlay the best-fit blackbody for these two SEDs. The typical AGN Type 1 spectrum (Richards et al. 2006), divided by a factor of 10, is given in purple. Overall, the SEDs of J221951 do not resemble the typical AGN Type 1 SED.

3.3 Optical to X-ray flux ratio, α_{OX}

For both TDEs and AGN, the UV to X-ray spectral slope, α_{OX} (Tananbaum et al. 1979; Wevers 2020), can be measured as:

$$\alpha_{OX} = -\frac{\log(f_{\nu,X}/f_{\nu,O})}{\log(\nu_X/\nu_O)} \quad (1)$$

where $f_{\nu,X}$ and $f_{\nu,O}$ are the X-ray and optical flux densities at rest-frame 2 keV and 2500 Å, respectively, and ν_X and ν_O are the X-ray and optical rest-frame frequencies at 2 keV and 2500 Å, respectively. Using the extinction-corrected observed *u*-band flux ($\lambda_{central} = 3501$ Å), at peak brightness, as a proxy for $f_{\nu,O}$ at rest-frame 2500 Å and the X-ray unabsorbed flux limit from an individual XRT visit, scaled to rest-frame 2 keV, assuming a photon index of $\Gamma = 1.7$, we obtain a value of $\alpha_{OX} \gtrsim 1.6$ at 58788 MJD.

3.4 Bolometric Light curve

We construct the bolometric light curve of J221951 from the *Swift*/UVOT data using SUPERBOL (Nicholl et al. 2018). The method allows us to integrate under the SED inferred from the multi-colour data at each epoch, and fit a blackbody function to estimate the temperature, radius, and missing energy outside of the observed wavelength range. For TDEs, a blackbody is an excellent approximation of the near-UV and optical emission (e.g. van Velzen et al. 2021). However, we note that the radius is computed under the assumption of spherical symmetry, which may not reflect the potentially complex geometry in TDEs. We include Galactic extinction but do not correct for the host extinction, which for this source is likely to be negligible (see §3.2). The bolometric light curve is plotted in Fig. 6. In the middle and bottom panels of Fig. 6, we display the effective temperature and radius of J221951. The maximum luminosity is $L_{max} = (1.1 \pm 0.7) \times 10^{45} \text{ erg s}^{-1} = (2.9 \pm 1.1) \times 10^{11} L_{\odot}$. The bumps seen in the photometry are also seen in the luminosity evolution, although the increase in the size of the errors makes these features less apparent. The effective temperature of J221951 has remained roughly constant throughout with an average temperature of $T = 2.8 \times 10^4 \text{ K}$, with a typical error for each inferred temperature of $\sim 7000 \text{ K}$. This is consistent with the values determined in §3.2. The blackbody radius evolves in a similar fashion as the luminosity of J221951. Trapezoidal integration of the blackbody luminosity over the span of *Swift* observations in rest frame days gives a total emitted energy of $E = 2.6 \times 10^{52} \text{ erg}$, a lower limit since we miss the peak of the light curve. This corresponds to a lower limit on the accreted mass of $M_{acc} = 0.14 M_{\odot}$, for an accretion efficiency of $\eta = 0.1$.

In Fig. 7, we compare the luminosity of J221951 with a sample of TDEs. J221951 is more luminous than the bulk population of TDEs and is on par with the luminosity of ASASSN-15lh, ASASSN-17jz and ASASSN-18jd (Dong et al. 2016; Holoien et al. 2021; Neustadt et al. 2020), which are luminous members of the population of ambiguous nuclear transients (ANTs; Holoien et al. 2021; Margutti et al. 2017a). ANTs are transients for which it is not clear if they are TDEs or related to AGN activity, with properties consistent with both classes. The temporal evolution of J221951 most closely resembles ASASSN-15lh after its initial peak. Other objects showing similar slowly declining light curve behaviour are the ANTs ASASSN-18el (Trakhtenbrot et al. 2019; Ricci et al. 2020; Laha et al. 2022a; Hinkle et al. 2022b) and ASASSN-20hx (Hinkle et al. 2022a), though they are overall an order of magnitude fainter. J221951 continues to be detected and, whether it is a TDE or an ANT, it is one of the longest observed to date (see also van Velzen et al. 2019b).

3.5 TDE model fit

If we assume J221951 is a TDE, we can derive physical parameters from our multiband light curves using the Modular Open Source Fitter for Transients (MOSFIT; Guillochon et al. 2018) with the TDE model from Mockler, Guillochon & Ramirez-Ruiz (2019). This model assumes a mass fallback rate derived from simulated disruptions of polytropic stars by a super massive black hole (SMBH) of $10^6 M_{\odot}$ (Guil-

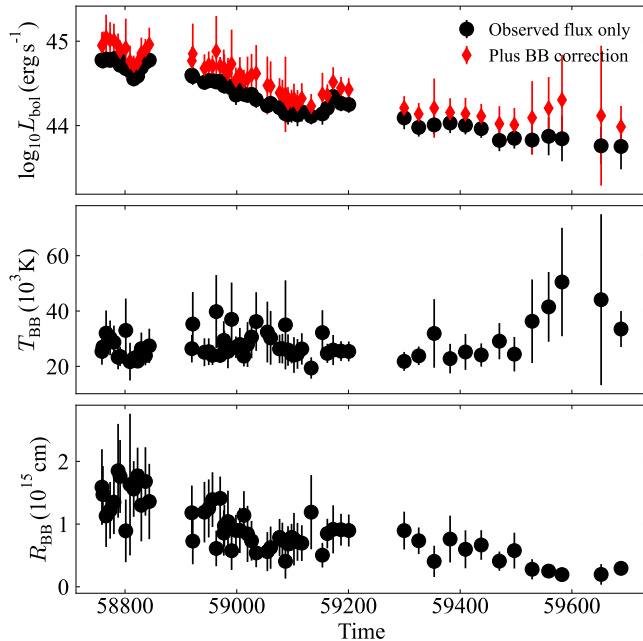


Figure 6. Top: the bolometric light curve of J221951 derived from the UVOT photometry. Middle: temperature evolution. Bottom: evolution of the blackbody radius. The luminosity and blackbody radius evolve similarly, while the temperature is approximately constant. Time is given in MJD.

lochon, Manukian & Ramirez-Ruiz 2014), and uses scaling relations and interpolations for a range of black hole masses, star masses, and impact parameters. The free parameters of the model, as defined by Mockler, Guillochon & Ramirez-Ruiz (2019), are the masses of the black hole, M_{BH} , and star, M_* ; the scaled impact parameter b ; the efficiency η of converting accreted mass to energy; the normalisation and power-law index, $R_{ph,0}$ and l_{ph} , connecting the radius to the instantaneous luminosity; the viscous delay time T_ν (the time taken for matter to circularise and/or move through the accretion disc) which acts approximately as a low pass filter on the light curve; the time of first fallback, t_0 , which is equivalent to our T_0 , assuming the TDE model is correct; the extinction, proportional to the hydrogen column density N_H in the host galaxy; and a white noise parameter, σ . The priors follow those used by Nicholl et al. (2022), and reflect the range of SMBH masses where optically-bright TDEs are expected (e.g. van Velzen 2018), the range of impact parameters covering both full and partial disruptions, accretion efficiencies for non-rotating to maximally-rotating black holes, and a broad range of possible photospheres and viscous timescales (see Mockler, Guillochon & Ramirez-Ruiz 2019, or details). In addition, we use the time of the last DES i-band archival observation as a lower limit on the T_0 prior.

The fits are applied using the python package, DYNASTY (Speagle 2020), which implements dynamic nested sampling methods to evaluate the posterior distributions of the model parameters. We plot the median and 16th-84th percentiles of the light curve posterior distribution from 100 realisations of the Markov Chain in Fig. 8. The model provides a good fit to the optical/UV bands but is unable to reproduce the undulations that are most clearly observed in

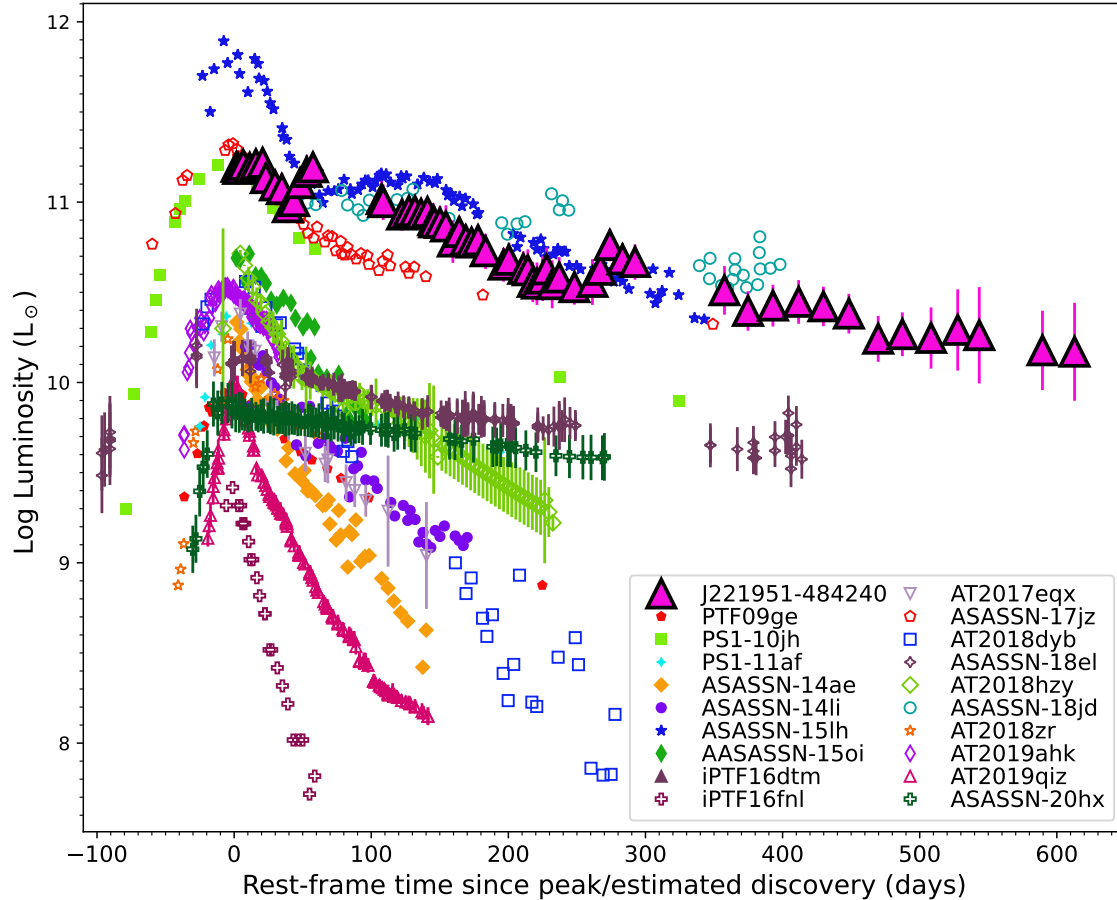


Figure 7. The bolometric light curve of J221951, with peak time taken as the UVOT discovery date, MJD 58756, together with a sample of tidal disruption events: PTF09ge (Arcavi et al. 2014); PS1-10jh (Gezari et al. 2012); PS1-11af (Chornock et al. 2014); ASASSN-14ae (Holoien et al. 2014); ASASSN-14li (Holoien et al. 2016b); ASASSN-15oi (Holoien et al. 2016a); iPTF16fnl (Blagorodnova et al. 2017); AT2017eqx (Nicholl et al. 2019); AT2018dyb (Leloudas et al. 2019); AT2018hzy (Short et al. 2020; Gomez et al. 2020); AT2018zr (van Velzen et al. 2019a); AT2019ahk (Holoien et al. 2019b); AT2019qiz (Nicholl et al. 2020b) and ambiguous nuclear transients: ASASSN-15lh (Dong et al. 2016; Leloudas et al. 2016; Godoy-Rivera et al. 2017; Brown et al. 2014), ASASSN-18jd (Neustadt et al. 2020), ASASSN-17jz (Holoien et al. 2021), ASASSN-18el (Trakhtenbrot et al. 2019), PS16dtm (Blanchard et al. 2017), ASASSN-20hx (Hinkle et al. 2022a). J221951 is comparable in luminosity to ASASSN-15lh and ASASSN-18jd.

the UV bands. Mockler, Guillochon & Ramirez-Ruiz (2019) also found for ASASSN-14li and ASASSN-15oi, that the observed photometry deviates from the decline of the model light curve. They suggest that for these TDEs additional late-time components may contribute, which are not modelled by MOSFIT. From the fit to J221951 we derive the posterior probability distributions of the parameters, listed in Table 3, with two-dimensional posteriors plotted in Supplementary Figure S.1. With the light curve observed to decay from the start of observations, the start time, T_0 , inferred with MOSFIT is MJD $58579.85^{+33.70}_{-31.41}$. The physical parameters point to the disruption of a $\sim 0.6M_{\odot}$ star by a black hole of mass $\log(M_{BH}/M_{\odot}) = 7.12$. The scaled impact parameter, $b = 0.63^{+0.08}_{-0.05}$, corresponds to a median physical impact parameter $\beta = R_t/R_p = 1.04$, where R_t is the tidal radius and R_p is the orbital pericentre. For the inferred SMBH mass, $R_t = 3.4R_S$, where R_S is the Schwarzschild radius, which is equivalent to 4.3×10^{-6} pc. Using the remnant

mass versus β curve from Ryu et al. (2020, their Fig. 4) for a $0.5\text{--}0.7 M_{\odot}$ star, up to ~ 25 per cent of the star could have survived this encounter.

Comparing these parameters to those derived in the same fashion for a sample of 32 TDEs (Nicholl et al. 2022), we find the black hole mass at the high end, star mass in the normal range and that the impact parameter is more consistent with the TDE-H spectroscopic class than the TDE-H+He¹². Compared to other TDEs from Mockler, Guillochon & Ramirez-Ruiz (2019) and Nicholl et al. (2022), the T_{ν} posterior is flat up to relatively high values, ~ 10 days, though there is similar posterior support for lower values \lesssim days. This broad distribution is likely due to the lack of

¹² TDEs may be divided into sub-classes spectroscopically (van Velzen et al. 2021). These classes are: TDE-H: TDEs with H I lines, TDE-He: TDEs with He II lines only, and TDE-H+He: TDEs with a mixture of H I, He II and N III lines.

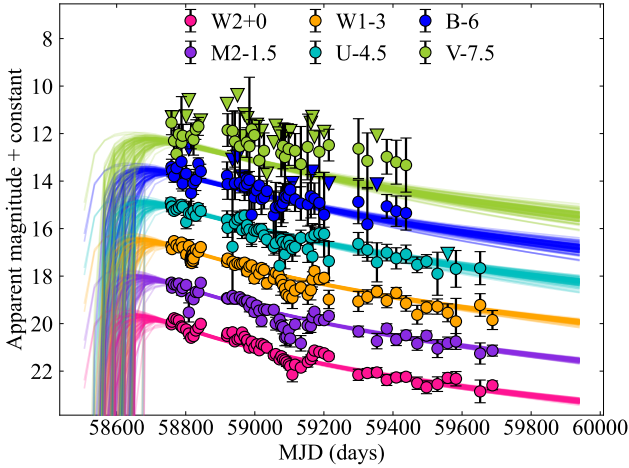


Figure 8. Fits to the multicolour light curve using the TDE model in MOSFIT (Guillochon et al. 2018; Mockler, Guillochon & Ramirez-Ruiz 2019). We plot the median and 16th-84th percentiles of the light curve posterior distribution from 100 realisations of the Markov Chain.

Table 3. Priors and marginalized posteriors for the MOSFIT TDE model. Priors are flat within the stated ranges, except for M_* , which uses a Kroupa initial mass function. The quoted results are the median of each distribution, and the error bars are the 16th and 84th percentiles. These errors are purely statistical; Mockler, Guillochon & Ramirez-Ruiz (2019) provide estimates of the systematic uncertainty. t_0 is observer frame days before the first detection.

Parameter	Prior	Posterior	Units
$\log(M_{BH}/M_\odot)$	[5,8]	$7.12^{+0.12}_{-0.09}$	
M_*	[0.001,100]	$0.62^{+0.41}_{-0.16}$	M_\odot
b	[0,2]	$0.63^{+0.08}_{-0.05}$	
$\log \epsilon$	[-2.3, -0.4]	$-0.60^{+0.13}_{-0.22}$	
$\log R_{ph,0}$	[-4,4]	0.43 ± 0.07	
l_{ph}	[0,4]	$0.63^{+0.09}_{-0.08}$	
$\log T_\nu$	[-3,3]	$-0.20^{+1.01}_{-1.30}$	d
t_0	[-500,0]	-177^{+34}_{-31}	d
$\log N_{H,host}$	[19,23]	$18.79^{+1.01}_{-1.42}$	cm^{-2}
$\log \sigma$	[-4,2]	$-0.76^{+0.03}_{-0.04}$	

constraints on the rise time of this source, together with the slow decay rate of the light curve. Viscous delays would broaden the light curve (relative to the fallback rate) around the peak, and the wide range of possible rise times allows for a wider range of viscous reprocessing than in faster-evolving TDEs with early data.

3.6 Spectroscopic Analysis

From the *HST* UV spectrum, given in Fig. 9, we are able to determine the redshift of J221951. The UV spectrum shows the cutoff caused by the Lyman limit absorption and, exceptionally, also the higher level Lyman lines, up to Ly-11, giving a redshift of $z = 0.5205 \pm 0.0003$. We use the higher level Lyman lines for the redshift determination since they are cleaner (not saturated or blended with other lines) than Ly- α and Ly- β . A P-Cygni profile is observed in the Ly- α line core, indicative of an outflow. Ly- β

is blended with the absorption edge of the nearby O VI resonance doublet. A fit with Voigt profiles of the Lyman lines from Ly- α up to Ly-11 shows that the Lyman lines are broadened by velocities of $\approx 90 \text{ km s}^{-1}$ with natural line broadening from interstellar hydrogen in the host galaxy $N_{HI} \approx 1 \times 10^{18} \text{ cm}^{-2}$. For the fit an additional emission at a level of $2.510^{-17} \text{ erg cm}^{-2} \text{ s}^{-1} \text{ \AA}^{-1}$ has been adopted and velocity broadening for the Lyman continuum of 1800 km s^{-1} .

We also see absorption lines of S VI at 933.4, 944.5 Å, N V at 1238.8, 1242.8 Å and O VI at 1031.9, 1037.6 Å. The red wings of the 1242.8 Å and 1037.6 Å lines match and we see extended absorption in the blue, consistent with a velocity of -1800 km s^{-1} in the absorption of O VI and -1750 km s^{-1} in the NV lines, with an accuracy of about 50 km s^{-1} . The absorption in these high ionisation lines extends to much larger velocities than we see in Ly- α . Notably, the emission on the red part of the lines is small, suggesting no simple spherical geometry for the emitting region.

In addition to the Ly- α core P-Cygni profile which extends over only a $400 \text{ km s}^{-1}/1.6 \text{ \AA}$ range, a broader emission feature, which is likely also Ly- α , surrounds that profile, best seen in Fig. 13. The emission extends from -2000 to 2000 km s^{-1} in the form of many peaks, or a broad emission that is cut through by many absorption lines, see Fig. 9.

Apart from the previously mentioned lines, we find absorption lines of NI 964.1 Å, C III 977.0 Å. An emission feature at 1073 Å might be a blend of Mg I 1073.5 Å with Si IV 1072.96 Å; increasing noise makes further identifications in the COS spectrum unreliable. Together these lines indicate various stages of ionisation. Emission features are seen, but cannot be identified as being either from host or Galaxy in origin. A prominent absorption line at a rest wavelength of 940.6 Å cannot be identified.

The optical spectra, except for the X-shooter spectrum, are presented in Fig. 10. The continuum changes colour with time, in general becoming bluer. However, the Magellan spectrum observed on 2019 November 11 is considerably bluer than all other spectra but coincides with a minimum in the UV light curves. We checked if there were any issues with the acquisition or reduction of this spectrum by overlaying the blue band flux measurement derived from the *B* band magnitude ($B = 20.0 \pm 0.1 \text{ mag}$) of the IMACS acquisition images, taken immediately beforehand. The *B* band flux from the acquisition image matches well, suggesting the flux calibration at the *B* band is correct, however, we cannot rule out the shape difference as being due to calibration issues because we lack photometric measurements at multiple wavelengths taken at the same time.

The evolution of the Mg II 2800 Å and H β line profiles is shown in Fig. 11. Mg II is observed to be initially double peaked, with the peaks narrowing over time and moving closer together, while the H β shows a reduction in the emission of its red wing with time. A possible explanation for the double peaked Mg II is emission from a bipolar source or an accretion or debris disc. However, this does not explain why the H β profile is different to that of Mg II. An alternative possibility is that it is a broad Mg II emission line with central Mg II absorption from the interstellar medium. If we examine Mg II and H β at the time of the *HST* observation, we see the width is consistent with the width of the broad Ly α profile observed in the *HST* spectrum. This suggests

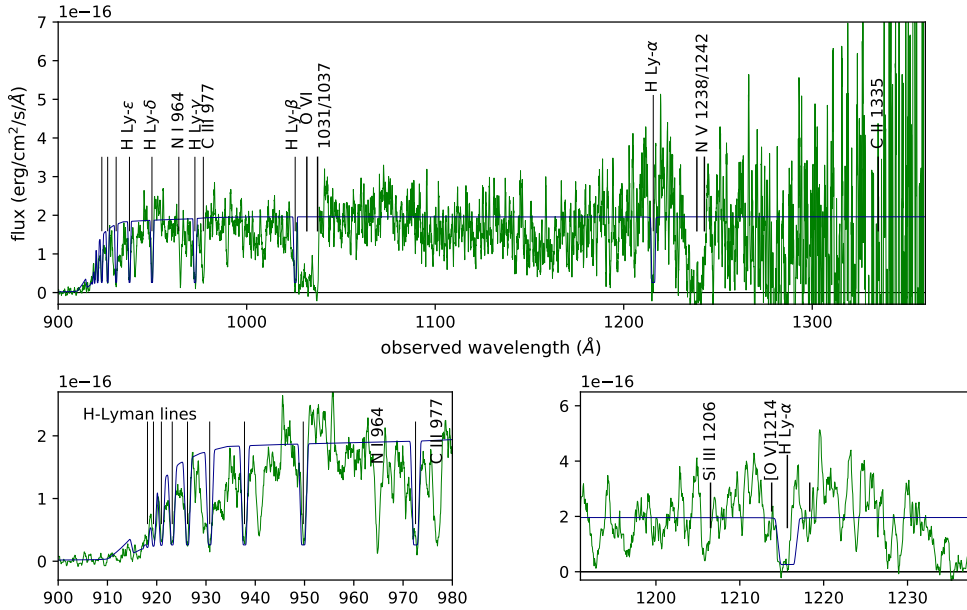


Figure 9. The *HST* COS spectrum between 900-1360Å. The blue line is a Voigt profile fit to all the Lyman lines for $N_{HI}=1 \times 10^{18}$ cm^{-2} and a line-broadening velocity of 90 km s^{-1} . The bottom figures show details. Left: the Lyman series can be seen up to quite high numbers. Right: The Ly- α absorption is all confined to the blue wing, the red wing shows weak emission. A blue shifted absorption from Ly- α at higher velocity of 650 km s^{-1} seems to be present blue-ward of the [O V] 1213.8 Å emission line. There are similar high-velocity features in Ly- β and Ly- γ

that all three are broad emission lines with narrow absorption from the interstellar medium superimposed.

At the location of [O III] 5007 Å line, the spectra are affected by telluric absorption. Since this [O III] line is important in identifying the presence of an AGN, we used a SALT spectrum of Feige 110, observed at a similar air-mass as the SALT spectra of J221951, to derive a telluric correction. In the telluric corrected spectra of J221951, we do not see evidence for strong [O III] 5007 Å emission. Using the 58760 MJD spectrum, we measure a 3σ upper limit of $4.3 \times 10^{-17} \text{ erg cm}^{-2} \text{ s}^{-1}$ on the flux of the [O III] 5007 Å emission line. Dividing this by the continuum flux $3.1 \times 10^{-17} \text{ erg cm}^{-2} \text{ s}^{-1} \text{ Å}^{-1}$ at 4861 Å, following the method of Boroson & Green (1992), we find an equivalent width for the [O III] 5007 Å emission line of < 1.4 Å.

The X-shooter spectrum, taken at a much later time, is given in Fig. 12. The spectrum shows a broad H α emission line, though the S/N is low because it falls at the edge of the VIS arm of the spectrograph. We also detect emission from Mg II 2800 Å as shown also in Fig. 11. A red excess is observed in the X-shooter spectrum. This is consistent with a second blackbody component observed in the SEDs, see §3.2.

We compare the SALT spectrum of J221951 taken at 58760 MJD and the X-shooter spectrum taken at 59411 MJD with a sample of spectra from other objects, including QSOs, known TDEs and ANTs in Fig. 13 and Fig. 14. Examining the UV spectra of J221951, the broad emission features resemble those found in the spectra of three TDEs, which were also shown to have broad absorption features: ASASSN-14li, iPTF15af, iPTF16fnl, and the low ionization broad absorption line QSO (BALQSO). The most significant absorptions in the J221951 spectrum, NV and O VI, are ob-

served in the optical spectrum of the ANTs ASASSN-15lh and ASASSN-17jz, however, the absorptions in the spectrum of J221951 are much broader. When examining the optical spectra of J221951, it most closely resembles the optical spectrum of the ANT, ASASSN-18jd.

3.7 Host Galaxy Properties

We built a host SED using archival observations from *GALEX*, *DES*, *VISTA* and *WISE*. We apply the stellar population synthesis models in PROSPECTOR (Leja et al. 2017, 2018) to the archival photometry, demonstrating that it is that of an underlying galaxy. We derive key physical parameters of the galaxy, which include the stellar mass, metallicity, current star-formation rate and the widths of five equal-mass bins for the star-formation history, and three parameters controlling the dust fraction and reprocessing (see Leja et al. 2017, for details). Leja et al. (2017) identify important degeneracies between age-metallicity-dust, and the dust mass-dust attenuation curve. PROSPECTOR is specifically designed to account for such degeneracies in parameter estimation using Markov Chain Monte Carlo analysis to fully explore the posterior probability density. The best-fitting model is shown compared to the archival photometry in Fig. 15 and the two-dimensional posteriors are plotted in Supplementary Figure S.2. We find a stellar mass $\log(M_*/M_\odot) = 10.8 \pm 0.1$ and a metallicity below or marginally consistent with solar, $\log Z/Z_\odot = -1.24^{+0.56}_{-0.47}$. PROSPECTOR fits to TDE hosts have also favoured low metallicities (Ramsden et al. 2022; Hammerstein et al. 2023). This may be expected since these galaxies tend to be below the mass of the Milky Way. We also find a low specific star-formation rate, $\log sSFR = -12.0 \pm 1 \text{ yr}^{-1}$ in the last 50 Myr, where

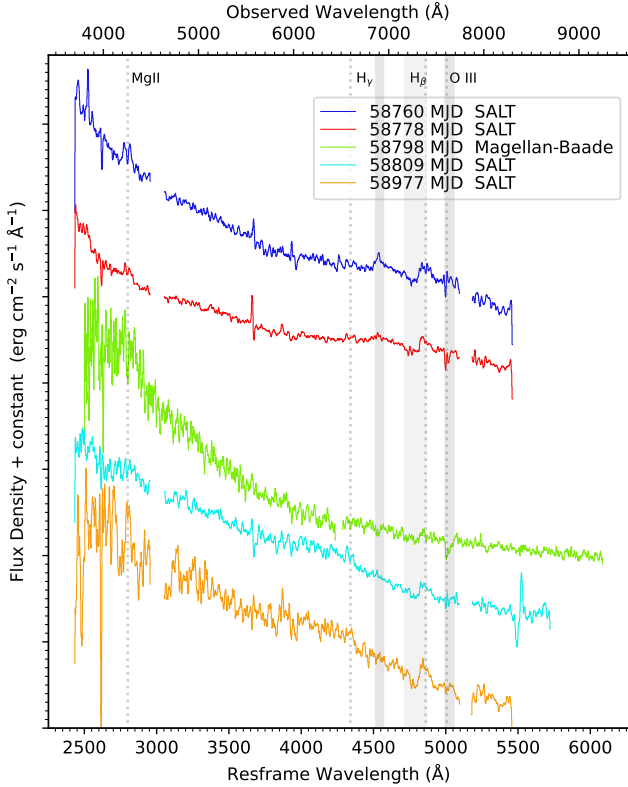


Figure 10. SALT and LCO-Magellan-Baade optical spectra of J221951. The spectra have been smoothed using a 1D Box filter kernel, with a kernel width of 5 for the SALT spectra, and a kernel width of 10 for the LCO-Magellan-Baade spectrum. The LCO-Magellan-Baade spectrum is markedly different in shape compared to the SALT spectra. The B band flux from the acquisition image matches well, suggesting the flux calibration at the B band is correct, however, we cannot rule out the shape difference as being due to calibration issues because we lack photometric measurements at multiple wavelengths taken at the same time. The grey bands show the telluric bands. The darker grey bands absorb more strongly than the light grey band. The SALT spectra have a telluric correction applied.

the reported values and uncertainties are the median and 16th/84th percentiles of the marginalized posterior distributions. The host galaxy SED is consistent with no AGN contribution, with the fraction of bolometric luminosity from an AGN, $f_{AGN} < 0.06$. This is consistent with the *WISE* W1-W2 colour of 0.20 mag, which suggests the archival IR emission is galaxy-like and not dominated by an AGN (Stern et al. 2012; Yan et al. 2013). Overall, the PROSPECTOR fit suggests that the host galaxy is consistent with a recently quenched galaxy with high star formation rate between 200-700 Myr ago and no strong AGN activity.

We compute the BH mass using the BH mass - bulge mass relation, $M_{BH} - M_{bulge}$ (Kormendy & Ho 2013; McConnell & Ma 2013; Ramsden et al. 2022). We are unable to decompose the host galaxy light into bulge and disc components since the host is too faint. We estimate the bulge mass from the total mass of the galaxy using the average bulge to total light (B/T) ratio, for a $\log(M_*/M_\odot) \sim 10.8$ the ratio is ~ 0.67 (Stone et al. 2018), indicating that a

large fraction of the mass of the galaxy is within the bulge. This gives $\log(M_{bulge}/M_\odot) \sim 10.6$. We first use the relationship derived from TDE host galaxies in Ramsden et al. (2022) and then compare this to the value produced by Kormendy & Ho (2013), which has been calibrated mainly at BH masses greater than those able to produce a TDE. Using the relationship derived using TDE host galaxies (Ramsden et al. 2022), we obtain an expected value of the SMBH mass of $\log(M_{BH}/M_\odot) = 6.9$. This value is consistent with the mass derived from the TDE model in §3.5. This mass is at the top end of the SMBH masses associated with TDEs (Wevers et al. 2017, 2019b; Nicholl et al. 2022) and within the theoretically expected mass range for TDEs (Kochanek 2016). If we use the Kormendy & Ho (2013) $M_{BH} - M_{bulge}$ relation the value of the SMBH mass we obtain a higher expected value of $\log(M_{BH}/M_\odot) = 8.2$, such a value is larger than the Hills mass for a $1 M_\odot$ star (Hills 1975)¹³, suggesting that if this is the correct BH mass, either the mass of the disrupted star is larger than $1 M_\odot$, contrary to the modelling in §3.5, or that J221951 is not a TDE as the star should have been swallowed whole without disruption.

4 DISCUSSION

With an absolute magnitude of $M_{u,AB} = -23$ mag, peak bolometric luminosity $L_{max} = (1.1 \pm 0.7) \times 10^{45} \text{ erg s}^{-1}$ and total radiated energy of $E > 2.6 \times 10^{52} \text{ erg}$, J221951 is one of the brightest, most energetic and long-lived UV transients observed to date. Based on some of the basic properties of this event, we are immediately able to draw conclusions on the nature of J221951 and exclude some classes of transient. The long-duration of the light curve and lack of an X-ray counterpart tends to rule out fast-evolving transients, including on-axis Gamma-ray bursts and most supernovae (SNe), except the long duration SN type IIn, which interact strongly with the circumstellar medium (e.g. Schlegel 1990; Smith 2017).

The broad absorption seen in NV and OVI, and the lack of undulations due to singly or doubly ionised metals are not expected in SNe (Baron et al. 2000; Foley & Kirshner 2013; Yan et al. 2017). The total radiated energy of J221951 of $> 2.6 \times 10^{52} \text{ erg}$ is also in tension with SN IIn theory (Sukhbold & Woosley 2016) and even the brightest confirmed interacting superluminous supernovae (SLSNe; Nicholl et al. 2020a), although there is a population of nuclear transients with similar total radiated energies that have some properties consistent with supernovae (e.g. PS1-10adi; Kankare et al. 2017, see §4.2 for further discussion). J221951 has a constant temperature at $\sim 2.3 \times 10^4 \text{ K}$. Supernovae have been shown to have similar initial temperatures, however SNe cool below 10^4 K within a few weeks (Holoien et al. 2019a). The *WISE* W2 peak luminosity ($\sim 10^{44} \text{ erg s}^{-1}$) is also of order a factor 100 brighter than the brightest known SN in the IR (see Fig. 8 of Jiang et al. 2019). The large bolometric luminosity suggests an association with a black hole, belonging to one of two main classes of events that also

¹³ The Hills mass is the largest BH mass for a given stellar mass that will result in a TDE and not swallow the star whole without disruption (Hills 1975). For a star of $0.1 - 1 M_\odot$, the Hills mass of a Schwarzschild BH is $10^7 - 10^8 M_\odot$.

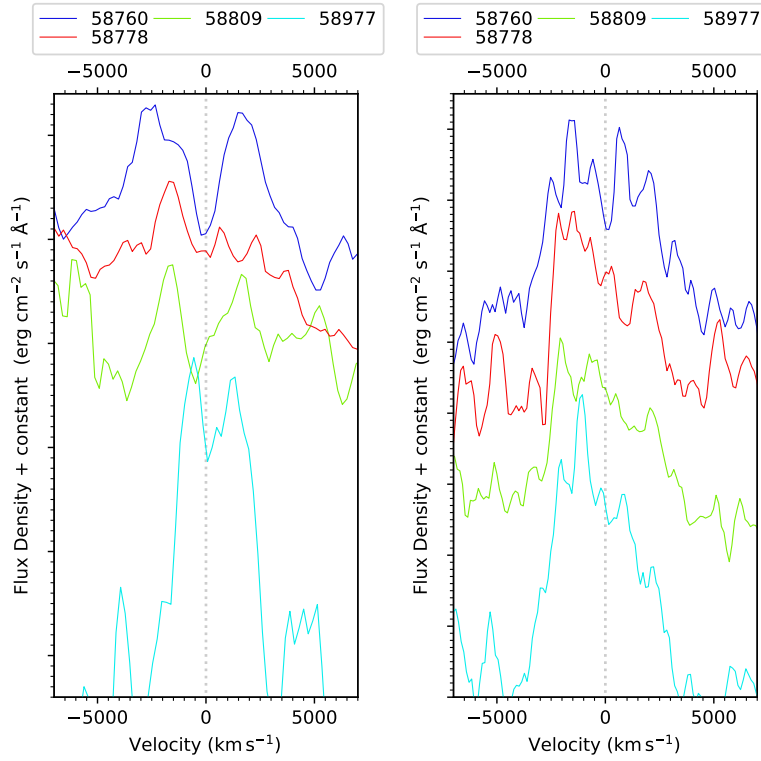


Figure 11. Time evolution, in MJD, of the Mg II (left) and H β (right) line profiles.

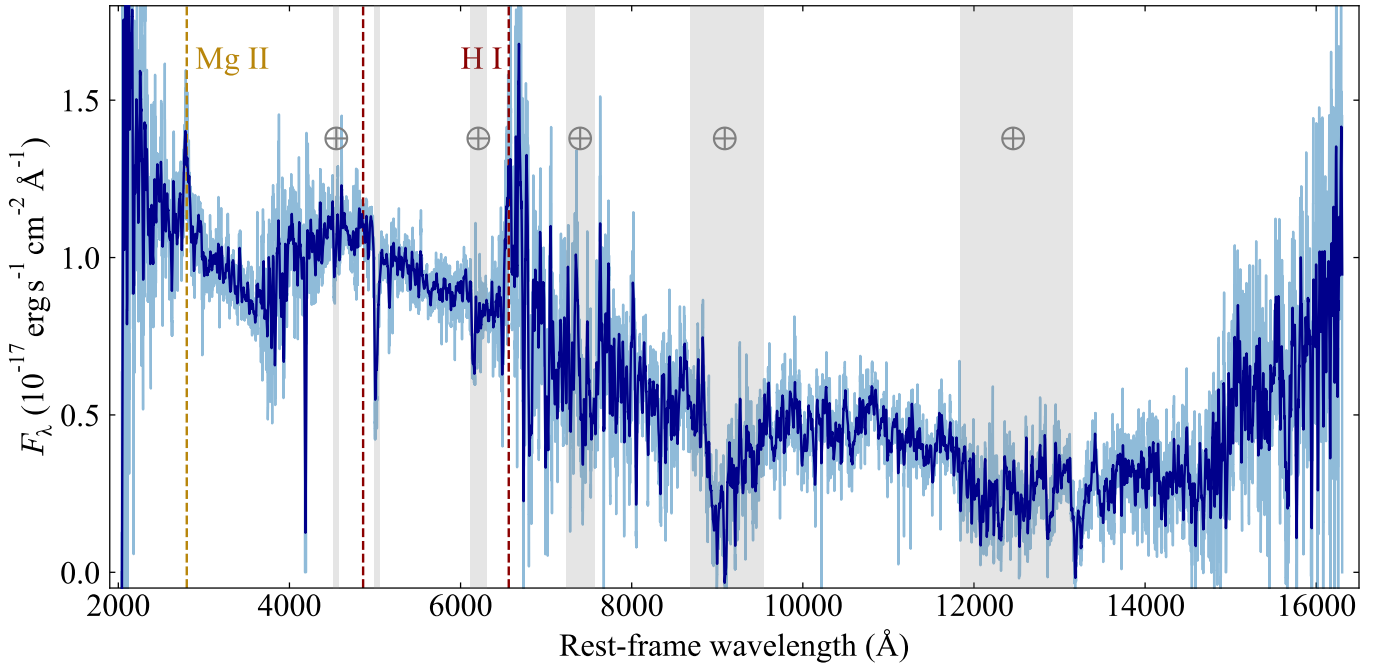


Figure 12. X-shooter spectrum taken on 59411 MJD. The spectrum has been binned using a 10 Å median filter (light blue) and then smoothed with a Savitsky-Golay filter (dark blue). H α 6565 Å and Mg II 2800 Å emission lines have been labeled. The spectrum turns up at the IR end, consistent with a second thermal component observed in the SEDs, e.g Fig. 5.

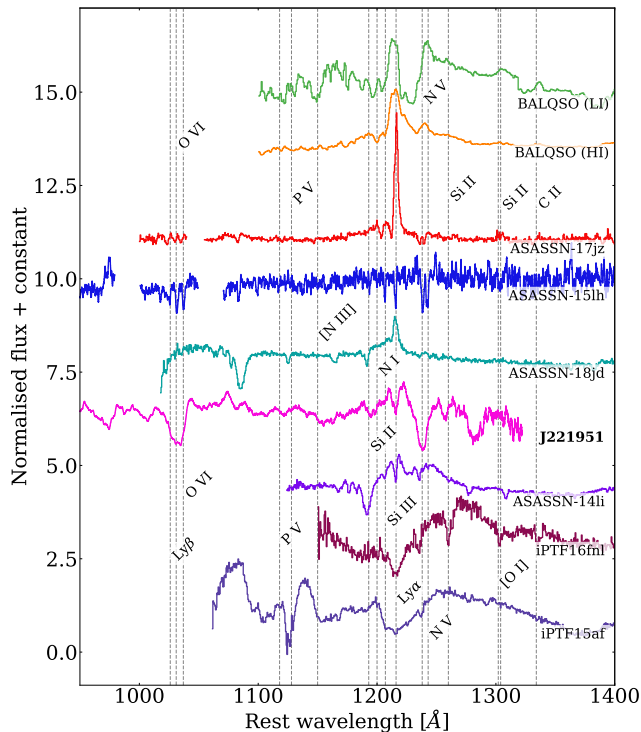


Figure 13. Comparison of the *HST* COS FUV spectrum of J221951, taken on 58977 MJD, with FUV spectra of other transient objects: ASASSN-14li (Holoien et al. 2016b), ASASSN-15lh (Brown et al. 2016), iPTF15af (Blagorodnova et al. 2019), iPTF16fnl (Brown et al. 2018), ASASSN-18jd (Neustadt et al. 2020), BALQSO low and high ionizations (LI and HI); Brotherton et al. 2001). J221951 most closely resembles the UV spectra of the TDEs: ASASSN-14li, iPTF15af, iPTF16fnl and the low ionization BALQSO, which all have broad absorption features.

display broad absorption line features: TDEs or AGN. In the following, we investigate these two main classes of event and then discuss the origin of the second, lower-temperature blackbody component.

4.1 Tidal disruption events

J221951 is positionally coincident with the nucleus of its host galaxy and is therefore consistent with a TDE origin. In TDEs, approximately half of the disrupted material falls back onto the SMBH, likely forming an accretion disc, while the other half is unbound (Rees 1988; Lacy, Townes & Hollenbach 1982). The spectra of TDEs are typically blue and thermal in nature (e.g. van Velzen et al. 2020). J221951 is consistent with this picture with the SEDs well fit by a blackbody with a typical temperature of $T \sim 23000$ K. With $H\alpha$ and weak $H\beta$ being observed in the optical spectra, J221951 would be classified as a H-only TDE in terms of the van Velzen et al. (2021) spectral classification scheme for optical TDEs. In addition, the overall light curve evolution can be fit reasonably well with a TDE model. Comparing the model parameters of J221951 to a sample of TDEs (Nicholl et al. 2022) suggests that for J221951 the BH mass is at the high end, the star mass is typical, and the low impact parameter is most similar to that of a H-only TDE rather than a He or Bowen TDE, consistent with the spectral classification

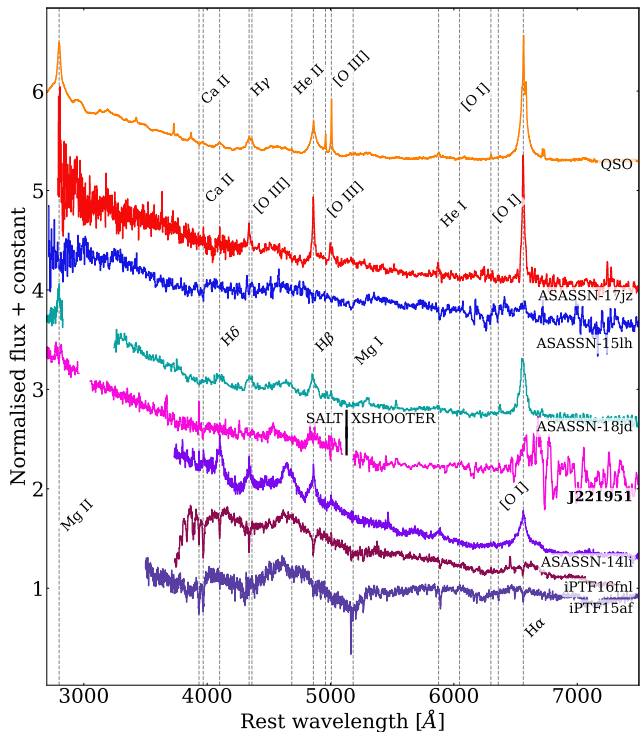


Figure 14. Comparison of the optical spectra of J221951 (SALT spectrum taken on 58760 MJD and X-shooter taken on 59411 MJD) with optical spectra of other transient objects: QSO (Vanden Berk et al. 2001), ASASSN-14li (Holoien et al. 2016b), iPTF15af (Blagorodnova et al. 2019), ASASSN-15lh (Brown et al. 2016), iPTF16fnl (Blagorodnova et al. 2017), ASASSN-17jz (Holoien et al. 2021), ASASSN-18jd (Neustadt et al. 2020). In terms of continuum shape and spectral lines, J221951 most closely resembles the optical spectra of the ANT ASASSN-18jd.

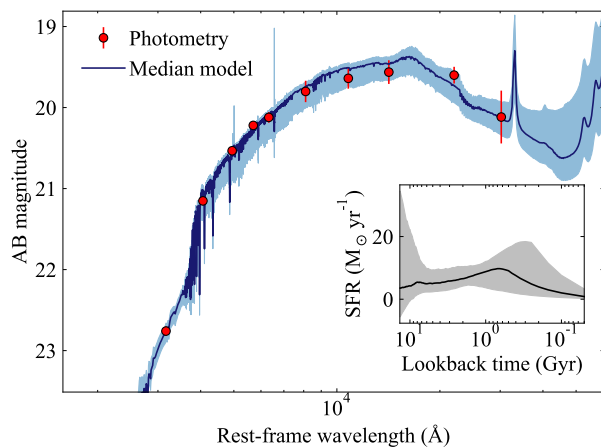


Figure 15. Archival photometry of the host galaxy of J221951, and SED fit using PROSPECTOR. The best-fitting model, as well as the 1σ dispersion in model realizations, is shown. The inset shows the derived star-formation history, which peaks at $10 M_{\odot} \text{ yr}^{-1}$ between a lookback time of 0.1 and 1 Gyr, and has a steep drop in the last ~ 0.5 Gyr. The shaded areas give the 1σ uncertainty on their respective parameter.

obtained from the spectra. The radio luminosity of J221951 is consistent with radio-quiet TDEs (Alexander et al. 2020). If J221951 does contain a jetted synchrotron source, we are unlikely to be viewing it on-axis.

We can use the SMBH mass estimates and the peak luminosity to determine the Eddington ratio. Using the lower mass estimate for the SMBH, based on the assumption that J221951 is a TDE ($\log(M/M_\odot) \sim 7.1$; see §3.5 & 3.7), we derive an Eddington luminosity of $L_{Edd} = 1.6 \times 10^{45} \text{ erg s}^{-1}$, and an Eddington ratio of $L_{max}/L_{Edd} = 0.70$. This is consistent with the typical Eddington ratios measured for a sample of TDEs with well-constrained SMBH masses, for which the peak luminosities are $\sim L_{Edd}$ (Wevers et al. 2019b). The L_{max}/L_{Edd} value computed for J221951 is likely to be an underestimate of the true ratio since we may not have observed the event at peak brightness and therefore the peak luminosity was probably larger and closer to L_{Edd} . However, if we use the larger black hole estimate of $\log(M_{BH}/M_\odot) \sim 8.2$ determined from the Kormendy & Ho (2013) BH mass – bulge mass relation (see §3.7), which challenges the formation of a TDE in the first place, then this increases $L_{Edd} = 2 \times 10^{46} \text{ erg s}^{-1}$ and reduces $L_{max}/L_{Edd} = 0.06$.

For a (minimum) total energy of $E \sim 3 \times 10^{52} \text{ erg}$, the accreted mass needed to radiate this energy is $\sim 0.14 M_\odot$ for a typical efficiency $\epsilon = 0.1$. This is much larger than the accreted mass estimates of most TDEs e.g. $< 0.01 M_\odot$ (Holoien et al. 2016a, 2019a; Hung et al. 2021) and is consistent with radiatively efficient accretion of the bound stellar debris (van Velzen et al. 2019b).

The peak luminosity of J221951 of $L_{max} = 1.1 \times 10^{45} \text{ erg s}^{-1}$ is larger than the bulk population of TDEs and is on par with the luminosity and energy of ASASSN-15lh, ASASSN-17jz and ASASSN-18jd (Dong et al. 2016; Holoien et al. 2021; Neustadt et al. 2020). The light curve shows bumps, which are not typical of TDE light curves (Neustadt et al. 2020), but are also seen in ASASSN-15lh (Brown et al. 2016) and ASASSN-18jd. TDEs tend to show smooth monotonic declining behaviour, though some do show variability and moderate rebrightening episodes (e.g. AT 2018fyk; Wevers et al. 2019a). ASASSN-15lh, ASASSN-17jz and ASASSN-18jd are ANTs (Holoien et al. 2021) and so their nature is also uncertain and under debate. Neustadt et al. (2020) discuss ASASSN-18jd as being either due to a TDE or as a rapid turn-on AGN. Holoien et al. (2021) suggest ASASSN-17jz was a SN II occurring in or near the disc of an existing AGN, and that the late-time emission is caused by the AGN transitioning to a more active state. For ASASSN-15lh, the literature is more extensive. Initially, ASASSN-15lh was deemed to be a hydrogen poor superluminous supernova (SLSN-I; Dong et al. 2016), but with an absolute peak magnitude more than 1 magnitude brighter than typical SLSNe-I. While some studies agreed with the SLSNe interpretation (Godoy-Rivera et al. 2017; Brown et al. 2016), there is a larger consensus that the properties of the UV light curve, spectra and the host galaxy together implies ASASSN-15lh is more consistent with a TDE origin (e.g. Brown et al. 2016; Leloudas et al. 2016; Margutti et al. 2017b; Krühler et al. 2018). Recently, an even more luminous ANT has been discovered, AT2021lwx (Subrayan et al. 2023; Wiseman et al. 2023). It is located at a redshift of 0.995, even higher than J221951. As with the other events discussed in this paragraph, there is debate

over whether AT2021lwx is a TDE or some other accretion event around a SMBH, particularly so in this case, because the light curve fit with MOSFIT requires the unlikely disruption of a $\sim 14 M_\odot$ star by a $10^8 M_\odot$ SMBH (Subrayan et al. 2023; Wiseman et al. 2023). This stellar mass is unusually large, whereas the MOSFIT parameters derived for J221951 are more consistent with likely TDE configurations.

The host galaxies of J221951, ASASSN-15lh ASASSN-17jz and ASASSN-18jd are also similar. For J221951 we determine the host mass to be $\log(M/M_\odot) = 10.8 \pm 0.1$ and the specific star formation rate $\log sSFR = -12 \pm 1 \text{ yr}^{-1}$. For ASASSN-15lh, Leloudas et al. (2016) showed the host to be a massive red galaxy with a small rate of ongoing star formation with host mass $\log(M/M_\odot) = 10.95^{+0.15}_{-0.11}$, a star formation rate $SFR < 0.02 M_\odot \text{ yr}^{-1}$ and a specific star formation rate of $\log sSFR < -12.5 \text{ yr}^{-1}$. For ASASSN-18jd the host mass is $\log(M/M_\odot) = 11.23^{+0.03}_{-0.33}$ and a star formation rate of $SFR = 0.6^{+0.1}_{-0.3} M_\odot \text{ yr}^{-1}$ (Neustadt et al. 2020). For ASASSN-17jz the host mass is $\log(M/M_\odot) = 10.74^{+0.11}_{-0.14}$, age = $2.2^{+1.2}_{-1.0} \text{ Gyr}$, and a star formation rate of $SFR = 2.9^{+0.4}_{-0.5} M_\odot \text{ yr}^{-1}$ (Holoien et al. 2021). The black hole mass at the centre of the host galaxy for ASASSN-15lh has been estimated from galactic scaling relationships to be $\sim 10^9 M_\odot$ (Leloudas et al. 2016; Krühler et al. 2018) and is consistent with the value derived from TDE light curve model fits (Mummery & Balbus 2020). For ASASSN-18jd, the black hole mass is $\log(M_{BH}/M_\odot) = 7.6 \pm 0.4$ (Neustadt et al. 2020) and for ASASSN-17jd the black hole mass is $\log(M_{BH}/M_\odot) \sim 7.5$ (Holoien et al. 2021). For J221951 we estimate a lower value of $\log(M_{BH}/M_\odot) \sim 7.1$ and an upper value of $\log(M_{BH}/M_\odot) \sim 8.2$ depending on the scaling relation. For ASASSN-15lh, the black hole mass is larger than the Hills mass and the same is true for the upper value of the black hole mass for J221951. For a black hole, bigger than this Hills mass, the star should have been swallowed whole without disruption. For ASASSN-15lh, to overcome this in order to allow the tidal disruption to occur, it has been suggested that the black hole is a rapidly spinning Kerr SMBH (Leloudas et al. 2016; Krühler et al. 2018; Mummery & Balbus 2020). In this case, the Hills mass increases by approximately an order of magnitude for extreme Kerr spins (Kesden 2012). There is some evidence to suggest that TDEs fade more slowly as the SMBH mass increases (Blagorodnova et al. 2017; Wevers et al. 2017; van Velzen et al. 2019b). Considering J221951 as a TDE, it would be consistent with this picture since the black hole mass of J221951 is at the high end of the TDE black hole mass distribution (Nicholl et al. 2022) and the decay rate is shallower than typical TDE light curves (see Fig. 7).

X-ray-selected TDEs have harder spectra with $\alpha_{OX} \sim 1.5$ and optically selected TDEs are softer with $\alpha_{OX} \sim 2.4$. In TDEs, high (soft) values of α_{OX} , associated with high Eddington ratios, are thought to arise from disc dominated spectra, while low (hard) values of α_{OX} , associated with low Eddington ratios, indicate power-law spectra (Wevers 2020). The latter may be more consistent with a jet rather than a disc. For J221951, α_{OX} is > 1.6 upon initial detection. This excludes the hardest spectra, allowing for either a thermal spectrum or a mixture of power-law and thermal components.

Examining the light curve behaviour of J221951, the light curve decays approximately as a broken power-law,

with a change to a steeper decay after 200 days. Around this time, the bolometric light curve behaviour of J221951 appears to have a similar decay rate to that of ASASSN-15lh after its second light curve peak. Mummery & Balbus (2020) and Leloudas et al. (2016) showed that this part of the light curve of ASASSN-15lh, at T+100 days, is consistent with being disc-dominated. Usually, the transition from fallback-dominated to disc-dominated emission is expected as a flattening of the TDE light curves and has been observed for a number of optical/UV TDEs (>few hundred days; van Velzen et al. 2019b). However, Mummery & Balbus (2020) showed that disc-dominated light curves may not be flat and may actually decay. If ASASSN-15lh and J221951 are similar in origin, this suggests that the late-time behaviour of J221951 may also be disc dominated. However, Mummery & Balbus (2020) note that their model is unable to reproduce the very latest UV emission of ASASSN-15lh, which is above their model prediction. Instead, they suggest that the late emission in ASASSN-15lh may be due to AGN activity (Krühler et al. 2018), additional material from the initial disruption returning to the disc, or even a state transition within the disc at low Eddington ratio (Mummery & Balbus 2020).

Comparing the UV spectrum of J221951 with other objects in Fig. 13, we see that J221951 is different to ASASSN-18jd and ASASSN-15lh. ASASSN-18jd shows weak N V emission at 1238.8, 1242.8 Å while we see it in absorption for J221951. ASASSN-15lh does not show any broad absorption features (Brown et al. 2016), though it does show N V and O VI absorptions, which are broad in the spectrum of J221951, but narrow for ASASSN-15lh. In terms of the broad absorption lines, J221951 most closely resembles TDEs ASASSN-14li (Cenko et al. 2016) and iPTFi6fnl (Brown et al. 2018) and that of the low-ionisation BALQSO. In general, the UV spectra of the other objects do not typically extend bluer than 1000-1100 Å, however, the UV spectrum of ASASSN-15lh (Brown et al. 2016) does cover a similar wavelength range to that of J221951. In both spectra, absorption from the Lyman series is observed although the features are more evident for J221951.

Comparing the optical spectra of J221951 with other objects in Fig. 14, we see that J221951 lacks the narrow line features that are present in the composite QSO spectrum. In contrast to the UV comparison J221951 looks least like ASASSN-14li and iPTF16fnl. No absorption features are present in the optical spectrum of J221951, while they are present in that of iPTF16fnl and the emission features in ASASSN-14li are much stronger than J221951. Overall, J221951 most closely resembles ASASSN-18jd in the optical, though has less prominent hydrogen Balmer lines. The emission lines of J221951 with $FWHM \sim 2200 \text{ km s}^{-1}$ are much narrower than typically observed for TDEs ($\sim 10^4 \text{ km s}^{-1}$), but are consistent with that observed for ASASSN-18jd (Neustadt et al. 2020).

Parkinson et al. (2020) investigated why some TDEs show broad absorption lines (BALs) while others display broad emission lines (BELs) in their UV spectra, using synthetic UV spectra for disc and wind-hosting TDEs, produced by a state-of-the-art Monte Carlo ionization and radiative transfer code. Using a variety of disc wind geometries and kinematics they naturally reproduce both BALs and BELs with winds. Sight lines looking into the wind cone, at low

angles relative to the plane of the disc, preferentially produce BALs, while other orientations preferentially produce BELs. Clumpy winds may also be a factor as clumping increases both the emission measure and the abundance of the relevant ionic species. Clumpier winds tend to produce stronger UV emission and absorption lines. This model suggests that we are viewing this event at high inclinations, towards the plane of a disc, if J221951 is indeed a TDE with a wind. In the scheme of Charalampopoulos et al. (2022), which assumes a reprocessing scenario whereby the optical emission of the TDE is produced by reprocessed X-rays, at high inclinations TDEs would only be H-only and lack X-ray emission, which is consistent with that observed for J221951. This inclination would also suggest we may not observe the relativistic jet, if present, which is also consistent with the lack of strong X-ray and radio emission.

Using the properties of the spectrum we can form a picture of this event if it is indeed a TDE. The Ly- α profile shows two broad emission peaks on either side in addition to a saturated central absorption (see Fig. 13). The absorption is likely to be located in our line of sight far from the ionising source. The emission peaks would be produced through recombination of hydrogen much closer into the core and may be from a rotating disc-like object (Sanbuichi, Fukue & Kojima 1994). The wavelength separation of each of the broad peaks of H Ly α from the centre suggests a velocity of $\approx 2000 \text{ km s}^{-1}$. We can determine the location of the emitting material that is causing the broad emission, specifically in the Hydrogen lines. Assuming it is orbiting the SMBH in a circular orbit, such that the kinetic energy equals the gravitational potential energy, then using the SMBH mass estimates from §3.7 and the velocity of the broad H Ly α emission, the radius would be $R \sim 5 \times 10^{16} - 1 \times 10^{18} \text{ cm}$ (0.017 - 0.36 pc).

The Ly- β absorption profile blends with the blue absorption trough of the O VI 1031.9 Å line. The O VI 1037.6 Å line shows a blue-shifted absorption profile. The extent of the absorption to the blue of Ly- β is much smaller than the velocities derived from the blue wing of the absorption in O VI of -1800 km s^{-1} , consistent with the lower ionisation lines being from a different component. The N V lines have a velocity edge consistent with a 1750 km s^{-1} outflow, so both are formed in the same component.

Examination of Fig. 11 shows that over time the red wing of H β becomes fainter and eventually the profile appears as an asymmetric blue-peaking hump. The He I 5017 Å line is present but weak and no He II lines were found. The P-Cygni lines of O VI, N V, etc. in the hotter outflows reach projected outflow velocities of 1800 km s^{-1} , but there is also a cooler outflow or turbulence of $\approx 90 \text{ km s}^{-1}$ as seen in Hydrogen absorption lines. The hotter outflow is likely produced in the inner region, within a fast outflow, while the velocities in the low-ionisation lines are located further out. Ly- α is optically thick enough to show an outflow. There, the higher Lyman lines are optically thin, at least from the Ly- γ on, which suggest a H column density of $\sim 10^{18} \text{ cm}^{-2}$. Entrained in the hot outflow is ionised H, which recombines, giving the broad emission seen in Ly α . The slow decay of the emission may suggest on-going accretion, while the evolution of the width of the Mg II resonance line emission suggests decreasing densities reduce opacity in the line wings and a possible expansion of the disc-like structure. A possible

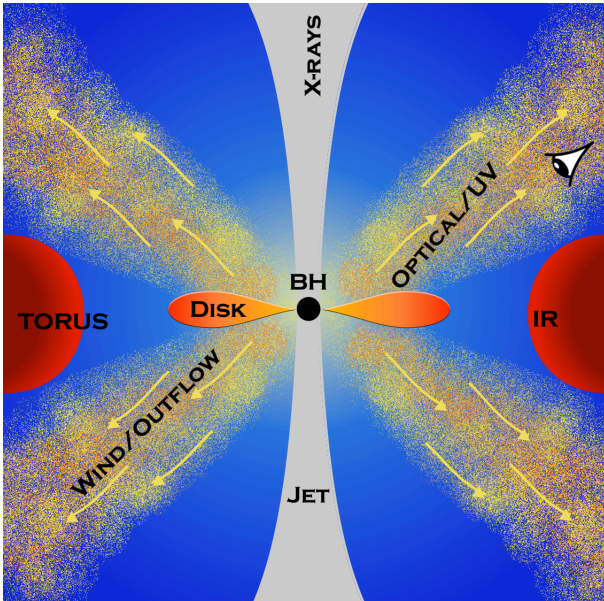


Figure 16. Artist impression of the geometry of the source. We likely see closer to the equatorial plane since we do not see the X-rays from the jet. The centre is a SMBH, the disc surface has wind that causes the blue absorptions in resonance lines, and near the equatorial plane, the disc is cooler and provides the narrow absorption lines seen in the low ionisation lines. Over time the disc expands and accretion decreases.

model (Fig. 16) can be envisioned based on the data taking the central source to be a SMBH with a disc of material that is flared, a wind outflow and with the observer looking at a high inclination, close to the plane of the disc, consistent with the scheme of Charalampopoulos et al. (2022). Over time the disc expands outward, becoming cooler on the outside, whilst maintaining the inner disc radius.

Overall, the peak luminosity of J221951 is higher than the bulk TDE population, consistent with the luminosity of ANTs: ASASSN-15lh ASASSN-17jz and ASASSN-18jd, suggesting J221951 is not a standard TDE. However, TDE light curve modelling suggests that J221951 is a TDE, with a typical star mass but with a BH mass at the high end. The spectra and modelling suggest it is a H-only TDE. J221951 has spectral properties consistent with ASASSN-18jd, in the optical, and BAL TDEs in the UV. The broad emission line features and lack of X-ray and radio emission may be because we are observing at a high inclination, close to the plane of the disc.

4.2 Active Galactic Nucleus

Given the potential nuclear nature of J221951, we now look at whether an AGN may be the cause of this transient. The optical spectra of J221951 show a double-peaked Mg II 2800 Å profile. Mg II 2800 Å is an emission line common to AGN, but not usually TDEs. ASASSN-18jd, suspected to be either a TDE or a rapid turn-on AGN, also has Mg II in emission (Neustadt et al. 2020). The narrow line widths, observed for J221951, of order 2000 km s^{-1} , are also commonly observed in AGN spectra. In addition, the broad absorption in the UV NV and O VI resonance lines, suggestive of outflows, also mimic the behaviour seen in C IV 1550 Å in the rest-frame

UV of BALQSOs. However, the lack of a strong [O III] 5007 Å emission line, with an EW of $< 1 \text{ Å}$, is not typical of AGN (Shen et al. 2011). Out of 105000 QSOs in the SDSS DR7 catalogue, 532 have a bolometric luminosity less than $L_{\text{bol}} = 10^{45} \text{ erg s}^{-1}$ and of these none has an EW $\lesssim 3 \text{ Å}$ (Shen et al. 2011); their average EW is 57 Å. The UV to X-ray spectral slope, for J221951 is $\alpha_{OX} > 1.6$, this is not consistent with QSOs but is consistent with BALQSOs; for QSOs $\alpha_{OX} \sim 1.4$ (see e.g. Marconi et al. 2004); for X-ray BALQSOs, $\alpha_{OX} \sim 1.90$; and for optical BALQSOs $\alpha_{OX} \sim 2.20$ (Blustin et al. 2008).

Based on an argument used for ASASSN-18jd, outlined by Neustadt et al. (2020) using the SDSS survey of quasars (MacLeod et al. 2012), it is unlikely that the variability of J221951 is due to normal QSO variability. J221951 is 3.4 magnitudes brighter than the archival g -band value (which is also likely a lower limit due to host contamination); the probability of achieving a $|\Delta m_g| > 3.5 \text{ mag}$ on a timescale of $< 5 \text{ years}$ is $P < 2 \times 10^{-6}$ (MacLeod et al. 2012). Graham et al. (2017) use CRTS data to provide even tighter constraints on the likelihood of observing large-magnitude changes. For $\Delta m = 3.0 \text{ mag}$, they find that the probability of achieving this change after 3200 days is 10^{-7} , which would be even larger for shorter time lags. These probabilities make it unlikely that the variability of J221951 is due to normal QSO variability.

However, just because such a large flare is unlikely, it is not impossible, and observations of AGN have discovered new and more extreme forms of variability, indicating that we are yet to discover the full range in AGN variability. A class of slow-blue transients, with $\Delta m > 1.5 \text{ mag}$ over \sim years, were identified in Lawrence et al. (2016) and a similar population was discovered by Graham et al. (2017). Lawrence et al. (2016) state that around 1 AGN in 10^4 displays such behaviour at any given time. The origin of these large magnitude changes is unknown and may be due to rare eruptive events from accretion, or microlensing (Lawrence et al. 2016). Although some instead may be attributed to stellar-related activity, such as TDEs, SLSNe and mergers of binary black holes (Graham et al. 2017).

While J221951 does share some characteristics of AGN, the lack of narrow line features, together with no AGN required in the host SED fitting and the $WISE W1 - W2$ colour, we can conclude that the host galaxy of J221951 did not host a strong AGN prior to the transient. This suggests that there has been no recent AGN activity prior to it turning on; the narrow line region (NLR) has not been ionized. We can estimate the distance from the SMBH to the NLR and thus estimate the minimum time that the AGN must have been inactive for us to observe no [O III] 5007 Å emission. Using the same argument, we can also estimate when we would expect to see the [O III] 5007 Å emission line in the spectrum if the AGN has newly turned on. Baskin & Laor (2005) state that for a single zone model, the distance to the $R_{NLR} = 40 L_{44}^{0.45} \text{ pc}$ where L_{44} is $\nu L_{\nu} / 10^{44} \text{ erg s}^{-1}$ at 4861 Å. From the first optical spectrum of J221951, we derive $\nu L(4861 \text{ Å}) = 1.61 \times 10^{44} \text{ erg s}^{-1}$. This results in a distance to the NLR, R_{NLR} of 49.5 pc. This implies that the AGN has not been active for at least 160 years. Therefore, we can conclude that if J221951 is due to AGN activity, it is ‘turning on’. In this case, we may have to wait decades before the [O III] 5007 Å emission line is detectable. Historically,

several AGN have been noted to ‘turn-on’ (Frederick et al. 2019; Yan et al. 2019), whereby galaxies transition from being LINERS to more active galaxies, such as narrow-line Seyfert 1s or radio-quiet QSOs (Gezari et al. 2017; Frederick et al. 2019). Some such objects show similar temporal behaviour to J221951 (e.g. SDSS1115+0544A; Yan et al. 2019).

Overall, J221951 did not host a strong AGN prior to the transient but has properties consistent with an AGN turning on. The clearest evidence of an AGN nature would be for J221951 to deviate from its current steadily decaying behaviour and to show a sustained period of increased flux - not just a bump or flare. Continuous UV monitoring of this source will therefore be important for monitoring the late-time behaviour. Deep X-ray observations of this source, for instance with *Chandra* or *XMM-Newton*, would provide tighter constraints on the X-ray brightness of the AGN.

4.3 Origin of the low-temperature blackbody

One interesting feature of J221951, is that there is evidence of two blackbody components in at least two of the SEDs. Two blackbody components were also observed in PS1-10adi (van Velzen et al. 2016; Kankare et al. 2017), PS16dtm (Jiang et al. 2017; Petrushevska et al. 2023) and most recently AT2021lwx (Wiseman et al. 2023). PS1-10adi is an AGN-associated transient that may be produced by a TDE, SNe or AGN activity (Kankare et al. 2017). Spectroscopically, the transient has features similar to a narrow line Seyfert 1 galaxy and to certain types of supernovae. For PS1-10adi, the blackbody temperatures (11000 K and 8000 K evolving to 2500 K and 1200 K) are lower than those observed for J221951. Jiang et al. (2019) argue that the IR excess observed in PS1-10adi is a dust echo of a TDE in an AGN, with the UV emission from the TDE heating and sublimating the dust in the AGN torus. PS16dtm is a TDE in a narrow line Seyfert 1 galaxy (Blanchard et al. 2017). It similarly displayed a MIR flare that was also interpreted as a dust echo of a TDE in an AGN (Jiang et al. 2017). MIR flares have also been found in other TDEs (van Velzen et al. 2016; Onori et al. 2022) and a systematic search of *WISE* observations of galaxies discovered over 100 with IR outbursts, thought to be the dust echoes of transient accretion events of SMBHs (Jiang et al. 2021). Jiang et al. (2017) noted that PS16dtm seemed to be detected a few days earlier in the MIR compared to the optical/UV. This may also be the case for J221951, see Fig. 3, however, it is difficult to confirm this given the large errors on the *WISE* data and the lack of optical data points in between the last DES visit and the UVOT detection. For PS16dtm, Jiang et al. (2017) note that the blackbody temperature in the MIR decreases with time, to a value below the sublimation temperature.

For J221951, a two blackbody component best fits only one of our SEDs which includes photometry redder than the *v* band. While a model with two blackbodies can be fitted to the three subsequent SEDs, it does not provide a better fit for any, although the fits do suggest that the temperature of this second component is decreasing as was observed for PS16dtm (Jiang et al. 2017). Assuming the IR excess observed in the 58787 MJD SED and the X-shooter spectrum of J221951 is also due to UV heating of nearby dust, then with a temperature of $\sim 2800 \pm 400$ K, the dust is consistent

with the sublimation temperature. Using the formula for the sublimation radius given in Namekata & Umemura (2016), their Eqn. 2, we can calculate the distance of the inner edge of the dusty torus from J221951. Taking the peak bolometric luminosity of $L_{bol} = 8.91 \times 10^{44}$ erg s $^{-1}$, assuming a grain radius of $0.1 \mu\text{m}$ and a sublimation temperature of ~ 2000 K, we compute a sublimation radius of 3×10^{17} cm corresponding to 0.09pc or 110 light days. This distance is typical of the distances expected of the inner edge of an AGN torus (Suganuma et al. 2006) and suggests that any preexisting dust within this radius will have been evaporated by UV emission from J221951.

Another TDE candidate observed to have low temperature blackbody component is Arp 299-B AT1, which was discovered in the galaxy merger Arp 299 and is associated with an AGN (Mattila et al. 2018). For Arp 299-B AT1, the temperature remains constant at 800 K beyond 2000 days after the transient was first observed to rise. At late times ($T_0 > +800$), the flux of J221951 is comparable to the host value in the reddest filters making it difficult to constrain the temperature of the second blackbody component. Observations with JWST would be important in enabling us to measure the IR flux and determine how the temperature of this second blackbody component evolves with time.

5 CONCLUSION

J221951 was discovered during the follow-up of a gravitational event: S190930t. It brightened by > 3 magnitudes in the UV compared to archival data and coincides with the centre of an optical/IR archival source, previously observed by DES and VISTA, which we show to be an underlying galaxy. Our spectroscopic redshift of 0.5205 rules out its association with the gravitational wave event. However, J221951 is a very unusual and long-lived UV-luminous nuclear transient. In this paper, we presented our follow-up of this transient and investigated its nature, whether it is a supernova, tidal disruption event or related to AGN activity. Below we summarise our key findings:

- A *HST* UV spectrum determines a redshift 0.5205 and reveals broad absorption lines from ionised species such as NV and OVI, along with narrow, low-ionisation lines of H and NI.
- J221951 has been observed at regular cadence for ~ 1000 days and continues to be detected in the UV, making it one of the longest observed UV transients with one of the best-sampled UV light curves.
- In the optical/UV the light curve decays from the start of observations. Several bumps that are more pronounced in the UV are present and appear to reset the brightness level, such that the light curve resumes its decay from close to the peak of the bump.
- A supernova explosion is ruled out by a total radiated energy of $\gtrsim 3 \times 10^{52}$ erg, as well as the lack of broad absorption lines in the optical spectrum
- Coincident *Swift*/XRT observations, do not detect X-ray emission from J221951, providing an upper limit to the X-ray luminosity of $L_X < 6 \times 10^{42}$ erg s $^{-1}$ (0.3-10 keV). Radio observations by ACTA also do not detect any radio emission with 3σ upper limits of 117 μJy at 5.5 GHz and 90 μJy at 9 GHz, with a 5.5GHz luminosity of $< 2 \times 10^{39}$ erg s $^{-1}$.

- The optical spectra are blue and relatively featureless, displaying only H β and Mg II in emission.

- Spectral energy distributions, created from UVOT data only (with filters *uvw2* through to *v*) for which we have the most epochs, are well fit by a power-law with a slope of $\beta = 0.49 \pm 0.04$ or a blackbody with an average temperature of 23000 ± 410 K. In SEDs constructed using UVOT and ground-based photometry, a two blackbody model is preferred in one SED, with evidence for two blackbody components observed in at least one other SED. The temperature of the second component is $\sim 2800 \pm 400$ K, which potentially cools across later SEDs.

- Examining the archival photometry, we determine the host galaxy to be a massive red galaxy, with a host galaxy stellar mass $\log(M/M_{\odot}) = 10.8 \pm 0.1$ and a low specific star formation rate $\log sSFR = -12 \pm 1 \text{ yr}^{-1}$ in the last 50 Myr.

- From the host SED fitting and the *WISE* *W1* – *W2* colour, we can conclude that the host galaxy of J221951 did not host a strong AGN prior to the transient.

- Using the Kormendy & Ho (2013) black hole mass – bulge mass scaling relation we estimate that the mass of the BH is $\log(M_{BH}/M_{\odot}) \sim 8.2$, bigger than this Hills mass, which implies for a $\sim 0.6M_{\odot}$ star it should have been swallowed whole without disruption and no emission should have been observed. One solution to this may be that the black hole is a rapidly spinning Kerr SMBH (Leloudas et al. 2016; Krühler et al. 2018; Mummery & Balbus 2020). However, using the black hole mass – bulge mass scaling relation derived from TDE host galaxies in Ramsden et al. (2022), we estimate a BH mass of $\log(M_{BH}/M_{\odot}) = 6.9$, which is consistent with the value derived from the TDE light curve model fits, $\log(M_{BH}/M_{\odot}) \sim 7.1$.

- The probability of seeing such a large flare from normal AGN activity is $P < 2 \times 10^{-6}$, characterising this as one of the most extreme nuclear flares to date.

- If due to AGN activity, the lack of narrow emission lines together with the host fitting and the *WISE* colour, implies it is caused by the AGN ‘turning on’.

The progenitor of J221951 is unclear. The optical and UV spectra show features resembling both TDEs and AGN. Overall its spectral, temporal and host properties and its energetics are closest in nature to ASASSN-15lh and ASASSN-18jd. ASASSN-15lh, ASASSN-18jd and J221951 belong to an increasing population of luminous blue transients, dubbed ambiguous nuclear transients for which the progenitors are not well constrained, but may be TDEs or due to AGN activity. Observing the late time evolution of J221951 will provide important clues as to its nature. For instance, if this source is associated with an AGN turning on we may expect it to deviate from its current steadily decaying behaviour. The clearest evidence of an AGN nature would be for J221951 to show a sustained period where it increased in flux - not just a bump or flare. Deep X-ray observations of this source, for instance with *Chandra* or *XMM-Newton*, would provide tight constraints on the X-ray brightness, a late-time continued detection would be indicative of an AGN and disfavour a TDE origin. Observations with JWST would be important in enabling us to understand the nature of the second lower-temperature blackbody component, potentially due to a dusty torus, and how it evolves with time.

The increase in the number of ambiguous nuclear transients, such as J221951, is blurring the boundary between what is considered TDE and AGN activity. Sources such as J221951 are important to pinpoint SMBHs that are otherwise hidden and provide the means to study SMBHs across various degrees of activity.

6 ACKNOWLEDGMENTS

This research has made use of data obtained from the High Energy Astrophysics Science Archive Research Center (HEASARC) and the Leicester Database and Archive Service (LEDAS), provided by NASA’s Goddard Space Flight Center and the School of Physics and Astronomy, University of Leicester, UK, respectively. This publication makes use of data products from the Wide-field Infrared Survey Explorer, which is a joint project of the University of California, Los Angeles, and the Jet Propulsion Laboratory/California Institute of Technology, funded by the National Aeronautics and Space Administration. This research has made use of the VizieR catalogue access tool, CDS, Strasbourg, France (DOI : 10.26093/cds/vizieR). The original description of the VizieR service was published in 2000, A&AS 143, 23. This research has made use of the NASA/IPAC Infrared Science Archive, which is funded by the National Aeronautics and Space Administration and operated by the California Institute of Technology. This paper includes data gathered with the 6.5 meter Magellan Telescopes located at Las Campanas Observatory, Chile. Some of the observations reported in this paper were obtained with the Southern African Large Telescope (SALT). This research is based on observations made with the NASA/ESA Hubble Space Telescope obtained from the Space Telescope Science Institute, which is operated by the Association of Universities for Research in Astronomy, Inc., under NASA contract NAS 5–26555. These observations are associated with program #16076. The Australia Telescope Compact Array is part of the Australia Telescope National Facility (<https://ror.org/05qajvd42>) which is funded by the Australian Government for operation as a National Facility managed by CSIRO. We acknowledge the Gomeri people as the traditional owners of the ATCA observatory site. This research uses services or data provided by the Astro Data Lab at NSF’s National Optical-Infrared Astronomy Research Laboratory. NOIRLab is operated by the Association of Universities for Research in Astronomy (AURA), Inc. under a cooperative agreement with the National Science Foundation. This publication uses the data from the *AstroSat* mission of the Indian Space Research Organisation (ISRO), archived at the Indian Space Science Data Centre (ISSDC). Part of the funding for GROND (both hardware as well as personnel) was generously granted from the Leibniz-Prize to Prof. G. Hasinger (DFG grant HA 1850/28-1). This research made use of Astropy, a community-developed core Python package for Astronomy (Astropy Collaboration et al. 2013). AAB, NPMK, MJP, KLP, PAE, APB and JPO acknowledge funding from the UK Space Agency. MDP acknowledges support for this work by the Scientific and Technological Research Council of Turkey (TÜBİTAK), Grant No: MFAĞ-119F073. RG and SBP acknowledge the financial support of ISRO under *AstroSat* archival Data utilization program (DS.2B-

13013(2)/1/2021-Sec.2). RG and SBP are also thankful to the *AstroSat* UVIT team for helping with UVIT data analysis. EA, MGB, SC, GC, AD, PDA, AM and GT acknowledge funding from the Italian Space Agency, contract ASI/INAF n. I/004/11/4. This work is also partially supported by a grant from the Italian Ministry of Foreign Affairs and International Cooperation Nr. MAE0065741. PDA acknowledges support from PRIN-MIUR 2017 (grant 20179ZF5KS). DBM is supported by research grant 19054 from Villum Fonden. MN is supported by the European Research Council (ERC) under the European Union’s Horizon 2020 research and innovation programme (grant agreement No. 948381) and by a Fellowship from the Alan Turing Institute. MG is supported by the EU Horizon 2020 research and innovation programme under grant agreement No 101004719. ET acknowledges support from the European Research Council (ERC) under the European Union’s Horizon 2020 research and innovation programme (grant agreement 101002761). DBM is supported by the European Research Council (ERC) under the European Union’s Horizon 2020 research and innovation programme (grant agreement No. 725246). The Cosmic Dawn Center is supported by the Danish National Research Foundation.

7 DATA AVAILABILITY

The *Swift* data underlying this article are available in the *Swift* archives at https://www.swift.ac.uk/swift_live/, <https://heasarc.gsfc.nasa.gov/cgi-bin/W3Browse/swift.pl>, <https://www.ssd.csiro.au/mmia/index.php?mission=swiftmastr>. The photometry of J221951 is available in the online supplementary material. The ATCA data are available from the Australia Telescope Online Archive – <https://atoa.atnf.csiro.au/>. The *HST* and *GALEX* observations are available from the MAST Portal – <https://mast.stsci.edu/portal/Mashup/Clients/Mast/Portal.html>. The X-shooter spectrum and GROND data are available from the ESO main archive – http://archive.eso.org/eso/eso_archive_main.html.

REFERENCES

- Aasi J. et al., 2015, *Classical and Quantum Gravity*, 32, 115012
- Abbott R. et al., 2020, arXiv e-prints, arXiv:2010.14527
- Abbott T. M. C. et al., 2018, *ApJ Suppl.*, 239, 18
- , 2021, *ApJ Suppl.*, 255, 20
- Acernese F. et al., 2015, *Classical and Quantum Gravity*, 32, 024001
- Alexander K. D., van Velzen S., Horesh A., Zauderer B. A., 2020, *Space Sci. Rev.*, 216, 81
- Arcavi I. et al., 2014, *ApJ*, 793, 38
- Arnaud K. A., 1996, in *Astronomical Society of the Pacific Conference Series*, Vol. 101, *Astronomical Data Analysis Software and Systems V*, Jacoby G. H., Barnes J., eds., p. 17
- Astropy Collaboration et al., 2013, *A&A*, 558, A33
- Bahcall N. A., 1986, *Annals of the New York Academy of Sciences*, 470, 331
- Baron E. et al., 2000, *ApJ*, 545, 444
- Baskin A., Laor A., 2005, *MNRAS*, 358, 1043
- Belkin S., Pozanenko A., Krugov M., Mazaeva E., Volnova A., IKI-FuN Follow-Up Collaboration, 2019, *GRB Coordinates Network*, 25963, 1
- Bertin E., Arnouts S., 1996, *A&A Suppl.*, 117, 393
- Bianchi L., Conti A., Shiao B., 2014, *Advances in Space Research*, 53, 900
- Bianchi L., Shiao B., Thilker D., 2017, *ApJ Suppl.*, 230, 24
- Bilicki M., Jarrett T. H., Peacock J. A., Cluver M. E., Steward L., 2014, *ApJ Suppl.*, 210, 9
- Blagorodnova N. et al., 2019, *ApJ*, 873, 92
- , 2017, *ApJ*, 844, 46
- Blanchard P. K. et al., 2017, *ApJ*, 843, 106
- Blustin A. J. et al., 2008, *MNRAS*, 390, 1229
- Boroson T. A., Green R. F., 1992, *ApJ Suppl.*, 80, 109
- Breeveld A. A., Landsman W., Holland S. T., Roming P., Kuin N. P. M., Page M. J., 2011, in *American Institute of Physics Conference Series*, Vol. 1358, *American Institute of Physics Conference Series*, J. E. McEnery, J. L. Racusin, & N. Gehrels, ed., pp. 373–376
- Brotherton M. S., Arav N., Becker R. H., Tran H. D., Gregg M. D., White R. L., Laurent-Muehleisen S. A., Hack W., 2001, *ApJ*, 546, 134
- Brown J. S. et al., 2018, *MNRAS*, 473, 1130
- Brown P. J., Breeveld A. A., Holland S., Kuin P., Pritchard T., 2014, *Ap&SS*, 354, 89
- Brown P. J. et al., 2016, *ApJ*, 828, 3
- Buckley D., Dong S., Ciroti S., Gromadzki M., Origo M., Mao J., Xu D., Manick R., 2019, *GRB Coordinates Network*, 25962, 1
- Buckley D. A. H., Swart G. P., Meiring J. G., 2006, in *Society of Photo-Optical Instrumentation Engineers (SPIE) Conference Series*, Vol. 6267, *Society of Photo-Optical Instrumentation Engineers (SPIE) Conference Series*, p. 62670Z
- Burgh E. B., Nordsieck K. H., Kobulnicky H. A., Williams T. B., O’Donoghue D., Smith M. P., Percival J. W., 2003, in *Society of Photo-Optical Instrumentation Engineers (SPIE) Conference Series*, Vol. 4841, *Instrument Design and Performance for Optical/Infrared Ground-based Telescopes*, Iye M., Moorwood A. F. M., eds., pp. 1463–1471
- Cenko S. B. et al., 2016, *ApJL*, 818, L32
- Charalampopoulos P. et al., 2022, *A&A*, 659, A34
- Chornock R. et al., 2014, *ApJ*, 780, 44
- Clampin M. et al., 2000, in *Society of Photo-Optical Instrumentation Engineers (SPIE) Conference Series*, Vol. 4013, *UV, Optical, and IR Space Telescopes and Instruments*, Breckinridge J. B., Jakobsen P., eds., pp. 344–351
- Crawford S. M. et al., 2010, in *Society of Photo-Optical Instrumentation Engineers (SPIE) Conference Series*, Vol. 7737, *Observatory Operations: Strategies, Processes, and Systems III*, Silva D. R., Peck A. B., Soifer B. T., eds., p. 773725
- Cutri R. M., et al., 2012, *VizieR Online Data Catalog*, II/311
- Cutri R. M. et al., 2021, *VizieR Online Data Catalog*, II/328
- Dixon W. V., Niemi S.-M., 2010, in *COS Instrument Handbook v. 2.0*, Vol. 2, p. 2
- Dong S. et al., 2016, *Science*, 351, 257
- Evans P. A. et al., 2009, *Mon. Not. R. Astr. Soc.*, 397, 1177
- , 2007, *Astron. Astrophys.*, 469, 379
- , 2016, *MNRAS*, 462, 1591

- Flewelling H. A. et al., 2020, *ApJ Suppl.*, 251, 7
- Foley R. J., Kirshner R. P., 2013, *ApJL*, 769, L1
- Frederick S. et al., 2019, *ApJ*, 883, 31
- Gehrels N. et al., 2004, *Astrophys. J.*, 611, 1005
- Gezari S. et al., 2012, *NATURE*, 485, 217
- , 2017, *ApJ*, 835, 144
- Godoy-Rivera D. et al., 2017, *MNRAS*, 466, 1428
- Gomez S. et al., 2020, *MNRAS*, 497, 1925
- Graham M. J., Djorgovski S. G., Drake A. J., Stern D., Mahabal A. A., Glikman E., Larson S., Christensen E., 2017, *MNRAS*, 470, 4112
- Green J. C., Wilkinson E., Morse J. A., 2003, in *Society of Photo-Optical Instrumentation Engineers (SPIE) Conference Series*, Vol. 4854, *Future EUV/UV and Visible Space Astrophysics Missions and Instrumentation.*, Blades J. C., Siegmund O. H. W., eds., pp. 72–80
- Greiner J. et al., 2008, *Publ. Astr. Soc. Pacif.*, 120, 405
- Guillochon J., Manukian H., Ramirez-Ruiz E., 2014, *ApJ*, 783, 23
- Guillochon J., Nicholl M., Villar V. A., Mockler B., Narayan G., Mandel K. S., Berger E., Williams P. K. G., 2018, *ApJ Suppl.*, 236, 6
- Hammerstein E. et al., 2023, *ApJ*, 942, 9
- Hills J. G., 1975, *NATURE*, 254, 295
- Hinkle J. T. et al., 2022a, *ApJ*, 930, 12
- , 2022b, *arXiv e-prints*, [arXiv:2206.04071](https://arxiv.org/abs/2206.04071)
- Holoien T. W. S. et al., 2019a, *ApJ*, 880, 120
- , 2016a, *MNRAS*, 463, 3813
- , 2016b, *MNRAS*, 455, 2918
- Holoien T. W. S. et al., 2021, *arXiv e-prints*, [arXiv:2109.07480](https://arxiv.org/abs/2109.07480)
- Holoien T. W. S. et al., 2014, *MNRAS*, 445, 3263
- Holoien T. W. S. et al., 2019b, *ApJ*, 883, 111
- Hung T. et al., 2021, *ApJ*, 917, 9
- Jiang N. et al., 2021, *ApJ Suppl.*, 252, 32
- Jiang N., Wang T., Mou G., Liu H., Dou L., Sheng Z., Wang Y., 2019, *ApJ*, 871, 15
- Jiang N. et al., 2017, *ApJ*, 850, 63
- Kamei Y., Abe F., Tristram P. J., Murata K. L., Onozato H., Utsumi Y., J-GEM Collaboration, 2019, *GRB Coordinates Network*, 25941, 1
- Kankare E. et al., 2017, *Nature Astronomy*, 1, 865
- Keller S. C. et al., 2007, *Publ. Astr. Soc. Australia*, 24, 1
- Kesden M., 2012, *Phys. Rev. D*, 85, 024037
- Kochanek C. S., 2016, *MNRAS*, 461, 371
- Kormendy J., Ho L. C., 2013, *Ann. Rev. Astron. Astrophys.*, 51, 511
- Krühler T. et al., 2018, *A&A*, 610, A14
- , 2008, *ApJ*, 685, 376
- Lacy J. H., Townes C. H., Hollenbach D. J., 1982, *ApJ*, 262, 120
- Laha S. et al., 2022a, *ApJ*, 931, 5
- , 2022b, *ApJ*, 929, 173
- Lawrence A. et al., 2016, *MNRAS*, 463, 296
- Leja J., Johnson B. D., Conroy C., van Dokkum P., 2018, *ApJ*, 854, 62
- Leja J., Johnson B. D., Conroy C., van Dokkum P. G., Byler N., 2017, *ApJ*, 837, 170
- Leloudas G. et al., 2019, *ApJ*, 887, 218
- , 2016, *Nature Astronomy*, 1, 0002
- LIGO Scientific Collaboration, Virgo Collaboration, 2019, *GRB Coordinates Network*, 25876, 1
- Loeb A., Ulmer A., 1997, *ApJ*, 489, 573
- MacLeod C. L. et al., 2012, *ApJ*, 753, 106
- Mainzer A. et al., 2011, *ApJ*, 731, 53
- Marconi A., Risaliti G., Gilli R., Hunt L. K., Maiolino R., Salvati M., 2004, *MNRAS*, 351, 169
- Margutti R. et al., 2017a, *ApJL*, 848, L20
- , 2017b, *ApJ*, 836, 25
- Mattila S. et al., 2018, *Science*, 361, 482
- McConnell N. J., Ma C.-P., 2013, *ApJ*, 764, 184
- McMahon R. G., Banerji M., Gonzalez E., Kuposov S. E., Bejar V. J., Lodieu N., Rebolo R., VHS Collaboration, 2013, *The Messenger*, 154, 35
- Mockler B., Guillochon J., Ramirez-Ruiz E., 2019, *ApJ*, 872, 151
- Morrissey P. et al., 2007, *ApJ Suppl.*, 173, 682
- Mummery A., Balbus S. A., 2020, *MNRAS*, 497, L13
- Namekata D., Umemura M., 2016, *MNRAS*, 460, 980
- Neustadt J. M. M. et al., 2020, *MNRAS*, 494, 2538
- Nicholl M. et al., 2018, *ApJL*, 866, L24
- , 2020a, *Nature Astronomy*, 4, 893
- , 2019, *MNRAS*, 488, 1878
- Nicholl M., Lanning D., Ramsden P., Mockler B., Lawrence A., Short P., Ridley E. J., 2022, *MNRAS*
- Nicholl M. et al., 2020b, *MNRAS*, 499, 482
- Oates S. R. et al., 2019a, *GRB Coordinates Network*, 25901, 1
- , 2019b, *GRB Coordinates Network*, 25939, 1
- , 2021, *MNRAS*, 507, 1296
- Onori F. et al., 2022, *MNRAS*, 517, 76
- Parkinson E. J., Knigge C., Long K. S., Matthews J. H., Higginbottom N., Sim S. A., Hewitt H. A., 2020, *MNRAS*, 494, 4914
- Pati A. K., Mahesh P. K., Nagabhushana S., Subramanian V. K., 2003, *Bulletin of the Astronomical Society of India*, 31, 479
- Petrushevska T. et al., 2023, *A&A*, 669, A140
- Poole T. S. et al., 2008, *Mon. Not. R. Astr. Soc.*, 383, 627
- Ramsden P., Lanning D., Nicholl M., McGee S. L., 2022, *arXiv e-prints*, [arXiv:2201.02650](https://arxiv.org/abs/2201.02650)
- Rees M. J., 1988, *NATURE*, 333, 523
- Ricci C. et al., 2020, *ApJL*, 898, L1
- Richards G. T. et al., 2006, *ApJ Suppl.*, 166, 470
- Roming P. W. A. et al., 2005, *Space Science Reviews*, 120, 95
- Ryu T., Krolik J., Piran T., Noble S. C., 2020, *ApJ*, 904, 100
- Sanbuichi K., Fukue J., Kojima Y., 1994, *PASJ*, 46, 605
- Sault R. J., Teuben P., Wright M. C. H., 2011, *MIRIAD: Multi-channel Image Reconstruction, Image Analysis, and Display. Astrophysics Source Code Library*, record [ascl:1106.007](https://www.ascl.net/1106.007)
- Sault R. J., Teuben P. J., Wright M. C. H., 1995, in *Astronomical Society of the Pacific Conference Series*, Vol. 77, *Astronomical Data Analysis Software and Systems IV*, Shaw R. A., Payne H. E., Hayes J. J. E., eds., p. 433
- Schlafly E. F., Finkbeiner D. P., 2011, *ApJ*, 737, 103
- Schlegel E. M., 1990, *MNRAS*, 244, 269
- Shakura N. I., Sunyaev R. A., 1973, *A&A*, 500, 33
- Shen Y. et al., 2011, *ApJ Suppl.*, 194, 45
- Short P. et al., 2020, *MNRAS*, 498, 4119
- Skrutskie M. F. et al., 2006, *Astron. J.*, 131, 1163

Smith N., 2017, in Handbook of Supernovae, Alsabti A. W., Murdin P., eds., p. 403

Speagle J. S., 2020, MNRAS, 493, 3132

Stern D. et al., 2012, ApJ, 753, 30

Stone N. C., Generozov A., Vasiliev E., Metzger B. D., 2018, MNRAS, 480, 5060

Subrayan B. M. et al., 2023, arXiv e-prints, arXiv:2302.10932

Suganuma M. et al., 2006, ApJ, 639, 46

Sukhbold T., Woosley S. E., 2016, ApJL, 820, L38

Tananbaum H. et al., 1979, ApJL, 234, L9

Tandon S. N. et al., 2017, Astron. J., 154, 128

The LIGO Scientific Collaboration and the Virgo Collaboration., 2019, GRB Coordinates Network

Trakhtenbrot B. et al., 2019, ApJ, 883, 94

van Velzen S., 2018, ApJ, 852, 72

van Velzen S. et al., 2019a, ApJ, 872, 198

—, 2021, ApJ, 908, 4

van Velzen S., Holoien T. W. S., Onori F., Hung T., Arcavi I., 2020, Space Sci. Rev. , 216, 124

van Velzen S., Mendez A. J., Krolik J. H., Gorjian V., 2016, ApJ, 829, 19

van Velzen S., Stone N. C., Metzger B. D., Gezari S., Brown T. M., Fruchter A. S., 2019b, ApJ, 878, 82

Vanden Berk D. E. et al., 2001, Astron. J., 122, 549

Vernet J. et al., 2011, A&A, 536, A105

Wevers T., 2020, MNRAS, 497, L1

Wevers T. et al., 2019a, MNRAS, 488, 4816

—, 2019b, MNRAS, 487, 4136

Wevers T., van Velzen S., Jonker P. G., Stone N. C., Hung T., Onori F., Gezari S., Blagorodnova N., 2017, MNRAS, 471, 1694

Wilson W. E. et al., 2011, MNRAS, 416, 832

Wiseman P. et al., 2023, arXiv e-prints, arXiv:2303.04412

Wright E. L. et al., 2010, Astron. J., 140, 1868

Yan L. et al., 2013, Astron. J., 145, 55

—, 2017, ApJ, 840, 57

—, 2019, ApJ, 874, 44

8 AFFILIATIONS

¹ School of Physics and Astronomy & Institute for Gravitational Wave Astronomy, University of Birmingham, B15 2TT, UK

² University College London, Mullard Space Science Laboratory, Holmbury St. Mary, Dorking, RH5 6NT, UK

³ Astrophysics Research Centre, School of Mathematics and Physics, Queens University Belfast, Belfast BT7 1NN, UK

⁴ Astrophysics Science Division, NASA Goddard Space Flight Center, Greenbelt, MD 20771, USA

⁵ Las Campanas Observatory, Carnegie Observatories, Colina El Pino, Casilla 601, La Serena, Chile

⁶ South African Astronomical Observatory, PO Box 9, Observatory 7935, Cape Town, South Africa

⁷ Department of Astronomy, University of Cape Town, Private Bag X3, Rondebosch 7701, South Africa

⁸ Department of Physics, University of the Free State, PO Box 339, Bloemfontein 9300, South Africa

⁹ Joint Space-Science Institute, Computer and Space Sciences Building, University of Maryland, College Park,

MD 20742, USA

¹⁰ University of Messina, MIFT Department, Polo Papardo, Viale F.S. D’Alcontres 31, 98166 Messina, Italy

¹¹ Australia Telescope National Facility, CSIRO Space and Astronomy, PO Box 76, Epping, NSW 1710, Australia

¹² Astronomical Observatory, University of Warsaw, Al. Ujazdowskie 4, 00-478 Warszawa, Poland

¹³ Aryabhata Research Institute of Observational Sciences (ARIES), Manora Peak, Nainital-263002, India

¹⁴ Department of Physics, Deen Dayal Upadhyaya Gorakhpur University, Gorakhpur-273009, India

¹⁵ Center for Space Science and Technology, University of Maryland Baltimore County, 1000 Hilltop Circle, Baltimore, MD 21250, USA.

¹⁶ Center for Research and Exploration in Space Science and Technology, NASA/GSFC, Greenbelt, Maryland 20771, USA

¹⁷ Department of Astronomy, University of Wisconsin, 475 N. Charter Str., Madison, WI 53704, USA

¹⁸ INAF-Osservatorio di Padova, vicolo dell Osservatorio 5, I-35122 Padova, Italy

¹⁹ School of Physics and Astronomy, University of Leicester, LE1 7RH, UK

²⁰ Max-Planck-Institut für Extraterrestrische Physik, Giessenbachstraße 1, 85748 Garching, Germany

²¹ Department of Physics, University of Bath, Bath, BA2 7AY, UK

²² Australia Telescope National Facility, CSIRO Space and Astronomy, 1828 Yarrrie Lake Road, Narrabri, NSW 2390, Australia

²³ George P. and Cynthia Woods Mitchell Institute for Fundamental Physics and Astronomy, Mitchell Physics Building,

Texas A.&M. University, Department of Physics and Astronomy, College Station, TX 77843, USA

²⁴ Department of Astronomy and Astrophysics, The Pennsylvania State University, University Park, PA 16802, USA

²⁵ Institute for Gravitation and the Cosmos, The Pennsylvania State University, University Park, PA 16802, USA

²⁶ Department of Astronomy and Astrophysics, University of Toronto, Toronto, ON, Canada

²⁷ INAF – IASF Palermo, Via Ugo La Malfa 153, I-90146, Palermo, Italy

²⁸ INAF – Osservatorio Astronomico di Brera, Via Bianchi 46, I-23807 Merate, Italy

²⁹ INAF-Osservatorio Astronomico di Roma, Via Frascati 33, I-00040 Monteporzio Catone, Italy

³⁰ University of Padova, Italy

³¹ Space Science Data Center (SSDC) - Agenzia Spaziale Italiana (ASI), I-00133 Roma, Italy

³² Department of Physics and Astronomy, Clemson University, Kinard Lab of Physics, Clemson, SC 29634-0978, USA

³³ National Science Foundation, Alexandria, VA 22314, USA

³⁴ Department of Astrophysics/IMAPP, Radboud University, 6525 AJ Nijmegen, The Netherlands.

³⁵ Cosmic Dawn Center (DAWN), Denmark.

³⁶ Niels Bohr Institute, University of Copenhagen, Jagtvej 128, 2200 Copenhagen N, Denmark.

³⁷ Los Alamos National Laboratory, B244, Los Alamos, NM, 87545, USA

³⁸ Department of Physics and Mathematics, Aoyama

Gakuin University, Sagami-hara, Kanagawa, 252-5258,
Japan

³⁹ Department of Physics, University of Rome Tor Vergata,
via della Ricerca Scientifica 1, I-00100 Rome, Italy

⁴⁰ INAF, Via del Fosso del Cavaliere, 100, 00133, Rome

⁴¹ Key Laboratory of Space Astronomy and Technology,
National Astronomical Observatories, Chinese Academy of
Sciences, Beijing, 100101, China

Supplementary Material: *Swift/UVOT discovery of Swift J221951-484240: a UV luminous ambiguous nuclear transient*

4 July 2023

S.1 SUPPLEMENTARY SECTION

arXiv:2307.01044v1 [astro-ph.HE] 3 Jul 2023

J221951

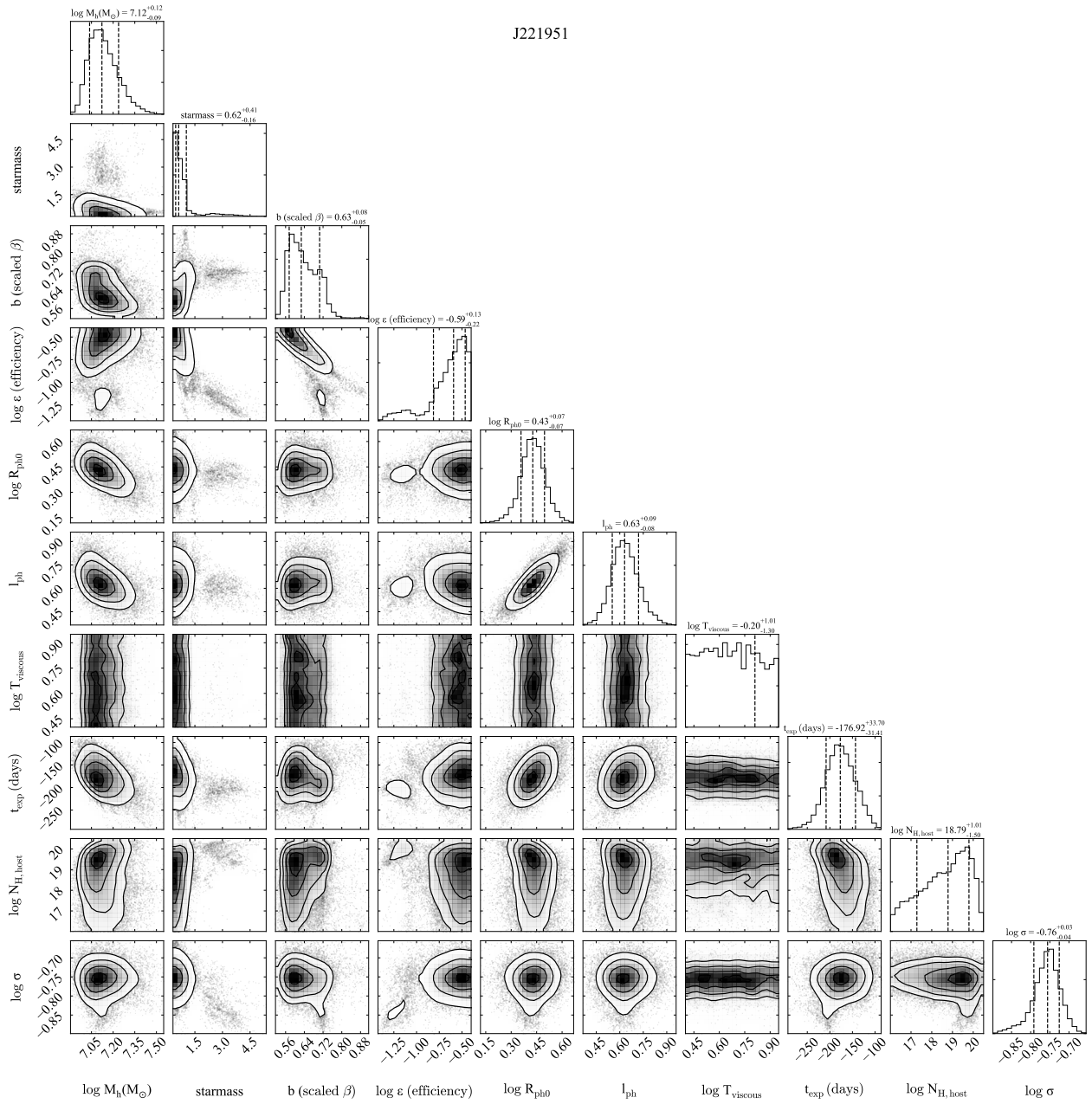


Figure S.1. Posterior probability density functions for the free parameters of the model light curves in Fig. 8 of the main paper.

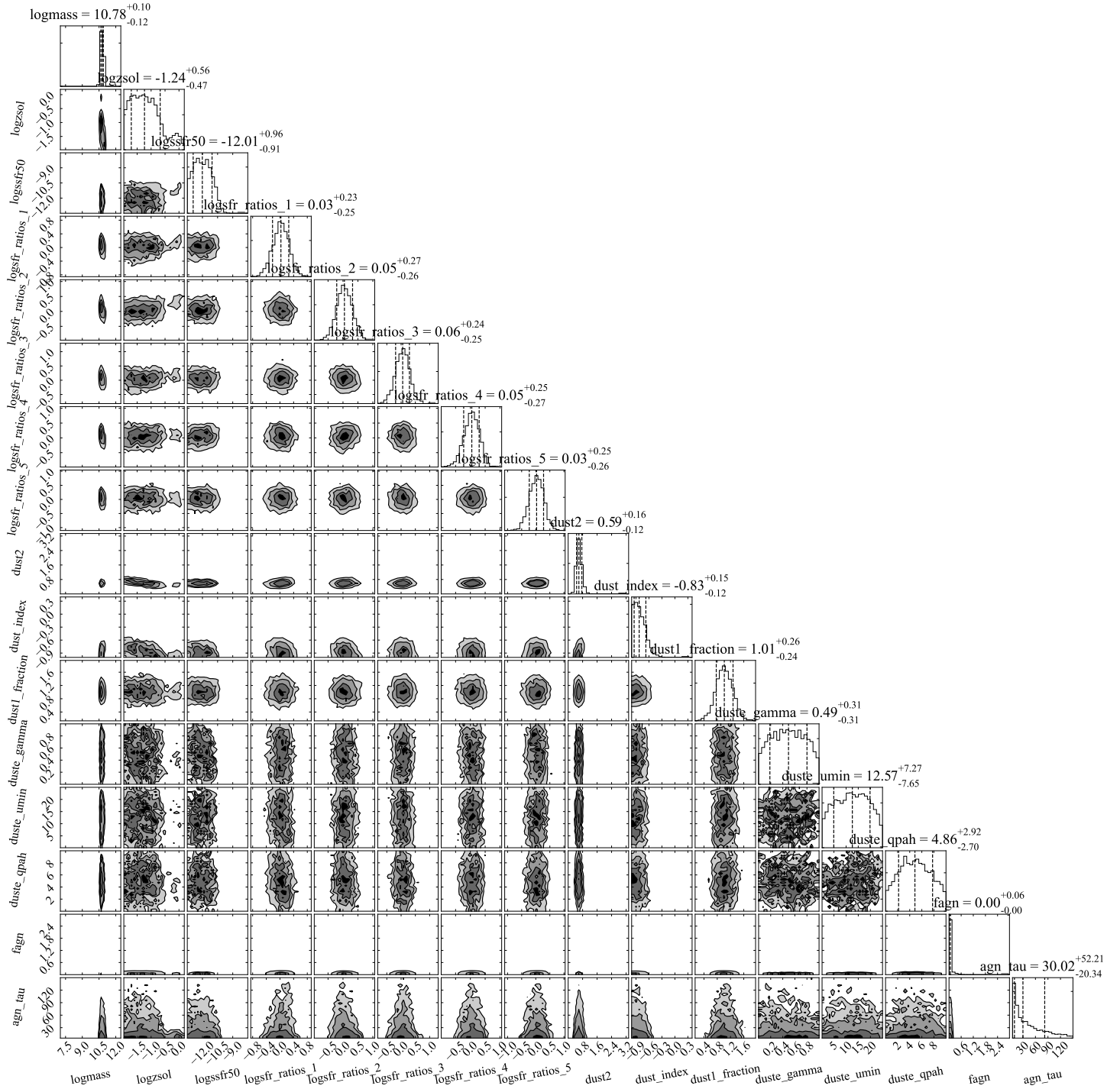


Figure S.2. Posterior probability density functions for the free parameters of the PROSPECTOR fit to the host photometry as shown in Fig. 15 of the main paper.

Table S.1: Log of the photometric observations. All magnitudes are given in AB, except the WISE magnitudes, which are Vega. No correction for extinction has been applied. Three sigma upper limits are given for data with signal-to-noise < 2.

Mid Time (MJD)	Bin Width (days)	Magnitude	Filter	Telescope	Reference
58758.68465	0.00046	19.04 ^{+0.62} _{-0.39}	<i>v</i>	<i>Swift</i>	–
58760.44175	0.16689	> 18.82	<i>v</i>	<i>Swift</i>	–
58766.12753	0.06537	19.80 ^{+0.72} _{-0.43}	<i>v</i>	<i>Swift</i>	–
58773.26051	0.09620	> 19.11	<i>v</i>	<i>Swift</i>	–
58780.19608	0.00160	19.52 ^{+0.50} _{-0.34}	<i>v</i>	<i>Swift</i>	–
58787.60099	0.09998	> 18.43	<i>v</i>	<i>Swift</i>	–
58791.15503	0.79531	19.59 ^{+0.57} _{-0.37}	<i>v</i>	<i>Swift</i>	–
58801.08327	0.03526	> 18.78	<i>v</i>	<i>Swift</i>	–
58808.94396	0.00029	> 18.10	<i>v</i>	<i>Swift</i>	–
58815.55075	0.43356	19.60 ^{+0.68} _{-0.41}	<i>v</i>	<i>Swift</i>	–
58822.49320	0.47062	> 18.72	<i>v</i>	<i>Swift</i>	–
58829.20136	0.13200	19.33 ^{+0.49} _{-0.34}	<i>v</i>	<i>Swift</i>	–
58836.50985	0.39919	19.20 ^{+0.44} _{-0.31}	<i>v</i>	<i>Swift</i>	–
58843.44692	0.10026	> 18.95	<i>v</i>	<i>Swift</i>	–
58919.64104	0.33148	> 18.26	<i>v</i>	<i>Swift</i>	–
58921.29634	0.06691	> 18.28	<i>v</i>	<i>Swift</i>	–
58935.40477	0.29896	> 18.22	<i>v</i>	<i>Swift</i>	–
58942.18132	0.16527	> 18.48	<i>v</i>	<i>Swift</i>	–
58949.84458	0.00010	> 17.89	<i>v</i>	<i>Swift</i>	–
58956.58525	0.35982	> 18.65	<i>v</i>	<i>Swift</i>	–
58963.29886	0.09964	> 19.62	<i>v</i>	<i>Swift</i>	–
58970.36505	0.19878	> 18.70	<i>v</i>	<i>Swift</i>	–
58976.76503	0.03359	> 18.86	<i>v</i>	<i>Swift</i>	–
58977.82978	0.69454	> 18.85	<i>v</i>	<i>Swift</i>	–
58984.30065	0.06308	> 18.54	<i>v</i>	<i>Swift</i>	–
58990.81583	0.99696	19.32 ^{+0.48} _{-0.33}	<i>v</i>	<i>Swift</i>	–
58998.54952	0.29946	19.56 ^{+0.55} _{-0.36}	<i>v</i>	<i>Swift</i>	–
59005.58852	0.36204	> 19.14	<i>v</i>	<i>Swift</i>	–
59012.85190	0.13290	> 19.20	<i>v</i>	<i>Swift</i>	–
59019.29892	0.19909	> 19.39	<i>v</i>	<i>Swift</i>	–
59026.49603	0.36396	> 19.11	<i>v</i>	<i>Swift</i>	–
59034.82707	1.59350	> 19.30	<i>v</i>	<i>Swift</i>	–
59054.78952	0.23353	> 19.86	<i>v</i>	<i>Swift</i>	–
59060.65864	0.33888	> 19.18	<i>v</i>	<i>Swift</i>	–
59071.67341	3.32464	> 19.50	<i>v</i>	<i>Swift</i>	–
59076.66080	0.52967	> 19.08	<i>v</i>	<i>Swift</i>	–
59081.69581	1.85366	> 18.78	<i>v</i>	<i>Swift</i>	–
59087.21008	1.59133	> 19.10	<i>v</i>	<i>Swift</i>	–
59091.79808	1.73226	> 19.37	<i>v</i>	<i>Swift</i>	–
59097.90413	0.59843	> 19.07	<i>v</i>	<i>Swift</i>	–
59102.46257	0.43191	> 19.40	<i>v</i>	<i>Swift</i>	–
59116.48845	0.40562	> 19.13	<i>v</i>	<i>Swift</i>	–
59133.31357	0.30064	> 19.37	<i>v</i>	<i>Swift</i>	–
59152.84635	0.03491	> 18.68	<i>v</i>	<i>Swift</i>	–
59162.16786	0.67411	> 19.05	<i>v</i>	<i>Swift</i>	–
59166.84168	0.62755	> 18.81	<i>v</i>	<i>Swift</i>	–
59172.61692	0.36363	> 19.64	<i>v</i>	<i>Swift</i>	–
59186.69754	0.23546	> 19.07	<i>v</i>	<i>Swift</i>	–
59200.54414	0.27191	> 19.43	<i>v</i>	<i>Swift</i>	–
59214.25326	0.10185	> 18.93	<i>v</i>	<i>Swift</i>	–
59300.14463	2.22472	> 18.79	<i>v</i>	<i>Swift</i>	–
59325.79693	0.13248	> 19.32	<i>v</i>	<i>Swift</i>	–
59353.51931	0.43237	> 19.59	<i>v</i>	<i>Swift</i>	–
59381.98648	0.96558	> 19.37	<i>v</i>	<i>Swift</i>	–
59409.46649	0.36167	> 19.48	<i>v</i>	<i>Swift</i>	–
59437.70631	0.27157	> 19.51	<i>v</i>	<i>Swift</i>	–
58758.67991	0.00046	19.40 ^{+0.37} _{-0.28}	<i>b</i>	<i>Swift</i>	–
58760.43780	0.16744	19.55 ^{+0.31} _{-0.24}	<i>b</i>	<i>Swift</i>	–

58766.12436	0.06465	$19.80^{+0.28}_{-0.22}$	<i>b</i>	<i>Swift</i>	—
58773.25637	0.09751	$19.45^{+0.19}_{-0.16}$	<i>b</i>	<i>Swift</i>	—
58787.59860	0.10012	$19.18^{+0.32}_{-0.25}$	<i>b</i>	<i>Swift</i>	—
58791.15074	0.79620	$20.10^{+0.36}_{-0.27}$	<i>b</i>	<i>Swift</i>	—
58801.34234	0.29722	$19.69^{+0.40}_{-0.29}$	<i>b</i>	<i>Swift</i>	—
58808.94091	0.00029	> 18.65	<i>b</i>	<i>Swift</i>	—
58815.54647	0.43277	> 19.36	<i>b</i>	<i>Swift</i>	—
58822.48861	0.47004	$20.09^{+0.57}_{-0.37}$	<i>b</i>	<i>Swift</i>	—
58829.19654	0.13279	$19.95^{+0.53}_{-0.36}$	<i>b</i>	<i>Swift</i>	—
58836.50415	0.39892	$19.27^{+0.28}_{-0.22}$	<i>b</i>	<i>Swift</i>	—
58843.44253	0.10099	$19.59^{+0.34}_{-0.26}$	<i>b</i>	<i>Swift</i>	—
58919.63885	0.33105	$19.77^{+0.72}_{-0.43}$	<i>b</i>	<i>Swift</i>	—
58921.29220	0.06712	> 19.10	<i>b</i>	<i>Swift</i>	—
58935.39978	0.29868	> 19.11	<i>b</i>	<i>Swift</i>	—
58942.17691	0.16381	> 19.03	<i>b</i>	<i>Swift</i>	—
58949.83996	0.00040	> 18.98	<i>b</i>	<i>Swift</i>	—
58956.58184	0.36151	$20.07^{+0.50}_{-0.34}$	<i>b</i>	<i>Swift</i>	—
58963.29520	0.10129	> 19.81	<i>b</i>	<i>Swift</i>	—
58970.36193	0.19847	$20.22^{+0.75}_{-0.44}$	<i>b</i>	<i>Swift</i>	—
58976.75721	0.03382	$19.93^{+0.30}_{-0.23}$	<i>b</i>	<i>Swift</i>	—
58977.82715	0.69416	$20.11^{+0.59}_{-0.38}$	<i>b</i>	<i>Swift</i>	—
58984.26557	0.09500	$19.95^{+0.41}_{-0.30}$	<i>b</i>	<i>Swift</i>	—
58990.80882	0.99638	> 20.05	<i>b</i>	<i>Swift</i>	—
58998.54137	0.29942	$20.68^{+0.63}_{-0.40}$	<i>b</i>	<i>Swift</i>	—
59005.58619	0.36235	$20.39^{+0.43}_{-0.31}$	<i>b</i>	<i>Swift</i>	—
59012.84402	0.13290	$20.18^{+0.45}_{-0.32}$	<i>b</i>	<i>Swift</i>	—
59019.29437	0.19828	> 19.72	<i>b</i>	<i>Swift</i>	—
59026.49056	0.36150	$20.68^{+0.59}_{-0.38}$	<i>b</i>	<i>Swift</i>	—
59034.82263	1.59611	$20.42^{+0.50}_{-0.34}$	<i>b</i>	<i>Swift</i>	—
59054.78463	0.23364	> 20.18	<i>b</i>	<i>Swift</i>	—
59060.65477	0.33857	> 19.83	<i>b</i>	<i>Swift</i>	—
59071.66996	3.32522	$21.05^{+0.72}_{-0.43}$	<i>b</i>	<i>Swift</i>	—
59076.65815	0.52984	> 19.90	<i>b</i>	<i>Swift</i>	—
59081.69338	1.85378	> 19.76	<i>b</i>	<i>Swift</i>	—
59087.20397	1.59347	$20.64^{+0.68}_{-0.41}$	<i>b</i>	<i>Swift</i>	—
59091.79305	1.73048	$20.69^{+0.72}_{-0.43}$	<i>b</i>	<i>Swift</i>	—
59098.13531	0.83517	$20.61^{+0.48}_{-0.33}$	<i>b</i>	<i>Swift</i>	—
59102.45759	0.43209	$20.36^{+0.38}_{-0.28}$	<i>b</i>	<i>Swift</i>	—
59108.71876	0.00118	> 20.09	<i>b</i>	<i>Swift</i>	—
59116.48588	0.40599	$20.77^{+0.62}_{-0.39}$	<i>b</i>	<i>Swift</i>	—
59133.30920	0.30032	> 19.86	<i>b</i>	<i>Swift</i>	—
59153.34541	0.53662	> 19.77	<i>b</i>	<i>Swift</i>	—
59162.16531	0.67358	> 19.42	<i>b</i>	<i>Swift</i>	—
59166.83896	0.62842	> 19.61	<i>b</i>	<i>Swift</i>	—
59172.61206	0.36545	> 19.69	<i>b</i>	<i>Swift</i>	—
59186.69305	0.23786	> 19.62	<i>b</i>	<i>Swift</i>	—
59200.53793	0.27023	> 19.97	<i>b</i>	<i>Swift</i>	—
59214.24674	0.10175	> 20.10	<i>b</i>	<i>Swift</i>	—
59299.74921	2.61736	> 19.66	<i>b</i>	<i>Swift</i>	—
59325.79085	0.13404	> 20.41	<i>b</i>	<i>Swift</i>	—
59353.51215	0.43141	> 20.14	<i>b</i>	<i>Swift</i>	—
59381.98167	0.96269	$21.06^{+0.61}_{-0.39}$	<i>b</i>	<i>Swift</i>	—
59409.46071	0.36403	> 20.23	<i>b</i>	<i>Swift</i>	—
59437.70091	0.27164	> 20.25	<i>b</i>	<i>Swift</i>	—
58756.77361	0.00043	$19.40^{+0.21}_{-0.17}$	<i>u</i>	<i>Swift</i>	—
58758.67894	0.00046	$19.58^{+0.23}_{-0.19}$	<i>u</i>	<i>Swift</i>	—
58760.43698	0.16755	$19.57^{+0.18}_{-0.15}$	<i>u</i>	<i>Swift</i>	—
58766.12374	0.06454	$19.75^{+0.14}_{-0.13}$	<i>u</i>	<i>Swift</i>	—
58773.25552	0.09777	$19.70^{+0.12}_{-0.11}$	<i>u</i>	<i>Swift</i>	—
58780.20476	0.00054	$19.62^{+0.22}_{-0.18}$	<i>u</i>	<i>Swift</i>	—
58787.59809	0.10015	$19.50^{+0.22}_{-0.18}$	<i>u</i>	<i>Swift</i>	—

58791.14985	0.79638	$19.58^{+0.12}_{-0.11}$	<i>u</i>	<i>Swift</i>	—
58801.34179	0.29728	$20.23^{+0.32}_{-0.24}$	<i>u</i>	<i>Swift</i>	—
58808.94026	0.00029	$19.85^{+0.61}_{-0.39}$	<i>u</i>	<i>Swift</i>	—
58815.54558	0.43261	$19.88^{+0.23}_{-0.19}$	<i>u</i>	<i>Swift</i>	—
58822.48767	0.46992	$19.76^{+0.20}_{-0.17}$	<i>u</i>	<i>Swift</i>	—
58829.19554	0.13295	$19.96^{+0.25}_{-0.20}$	<i>u</i>	<i>Swift</i>	—
58836.50298	0.39887	$19.63^{+0.20}_{-0.17}$	<i>u</i>	<i>Swift</i>	—
58843.44163	0.10114	$19.76^{+0.19}_{-0.17}$	<i>u</i>	<i>Swift</i>	—
58919.63845	0.33098	$20.12^{+0.43}_{-0.31}$	<i>u</i>	<i>Swift</i>	—
58921.29147	0.06715	$20.47^{+0.47}_{-0.33}$	<i>u</i>	<i>Swift</i>	—
58935.39892	0.29864	> 19.78	<i>u</i>	<i>Swift</i>	—
58942.17614	0.16357	$20.28^{+0.44}_{-0.31}$	<i>u</i>	<i>Swift</i>	—
58949.81379	0.02572	$20.12^{+0.41}_{-0.30}$	<i>u</i>	<i>Swift</i>	—
58956.58124	0.36180	$20.04^{+0.23}_{-0.19}$	<i>u</i>	<i>Swift</i>	—
58963.29455	0.10156	$20.56^{+0.41}_{-0.30}$	<i>u</i>	<i>Swift</i>	—
58970.36138	0.19842	$19.96^{+0.26}_{-0.21}$	<i>u</i>	<i>Swift</i>	—
58976.75562	0.03386	$20.54^{+0.25}_{-0.20}$	<i>u</i>	<i>Swift</i>	—
58977.82668	0.69410	$20.36^{+0.34}_{-0.26}$	<i>u</i>	<i>Swift</i>	—
58984.26465	0.09527	$20.55^{+0.35}_{-0.27}$	<i>u</i>	<i>Swift</i>	—
58990.80739	0.99627	$20.87^{+0.33}_{-0.25}$	<i>u</i>	<i>Swift</i>	—
58998.53971	0.29942	$20.58^{+0.25}_{-0.20}$	<i>u</i>	<i>Swift</i>	—
59005.58569	0.36241	$20.59^{+0.24}_{-0.20}$	<i>u</i>	<i>Swift</i>	—
59012.84241	0.13290	$20.52^{+0.24}_{-0.20}$	<i>u</i>	<i>Swift</i>	—
59019.29342	0.19811	$20.53^{+0.28}_{-0.22}$	<i>u</i>	<i>Swift</i>	—
59026.48943	0.36102	$20.79^{+0.29}_{-0.23}$	<i>u</i>	<i>Swift</i>	—
59034.82171	1.59663	$20.96^{+0.38}_{-0.28}$	<i>u</i>	<i>Swift</i>	—
59054.78362	0.23365	$21.27^{+0.40}_{-0.29}$	<i>u</i>	<i>Swift</i>	—
59060.65397	0.33850	$21.11^{+0.50}_{-0.34}$	<i>u</i>	<i>Swift</i>	—
59071.66923	3.32533	> 20.98	<i>u</i>	<i>Swift</i>	—
59076.65759	0.52987	$20.95^{+0.37}_{-0.28}$	<i>u</i>	<i>Swift</i>	—
59081.69286	1.85381	$21.07^{+0.47}_{-0.33}$	<i>u</i>	<i>Swift</i>	—
59087.20272	1.59389	> 20.57	<i>u</i>	<i>Swift</i>	—
59091.79201	1.73012	$21.17^{+0.49}_{-0.34}$	<i>u</i>	<i>Swift</i>	—
59098.13429	0.83530	$21.02^{+0.32}_{-0.25}$	<i>u</i>	<i>Swift</i>	—
59102.45657	0.43212	$21.23^{+0.41}_{-0.29}$	<i>u</i>	<i>Swift</i>	—
59108.71635	0.00118	$21.35^{+0.66}_{-0.41}$	<i>u</i>	<i>Swift</i>	—
59116.48534	0.40606	$21.27^{+0.45}_{-0.32}$	<i>u</i>	<i>Swift</i>	—
59133.30829	0.30025	$20.89^{+0.37}_{-0.28}$	<i>u</i>	<i>Swift</i>	—
59153.34460	0.53636	$21.37^{+0.68}_{-0.42}$	<i>u</i>	<i>Swift</i>	—
59162.16477	0.67348	$20.87^{+0.62}_{-0.39}$	<i>u</i>	<i>Swift</i>	—
59166.83839	0.62859	> 20.29	<i>u</i>	<i>Swift</i>	—
59172.61106	0.36581	$20.76^{+0.38}_{-0.28}$	<i>u</i>	<i>Swift</i>	—
59186.69212	0.23834	$20.70^{+0.43}_{-0.31}$	<i>u</i>	<i>Swift</i>	—
59200.53604	0.26927	$20.72^{+0.32}_{-0.25}$	<i>u</i>	<i>Swift</i>	—
59214.24541	0.10173	> 20.70	<i>u</i>	<i>Swift</i>	—
59299.74830	2.61769	$21.14^{+0.58}_{-0.38}$	<i>u</i>	<i>Swift</i>	—
59325.78959	0.13435	$21.39^{+0.37}_{-0.28}$	<i>u</i>	<i>Swift</i>	—
59353.51069	0.43122	> 20.76	<i>u</i>	<i>Swift</i>	—
59381.98068	0.96211	$21.51^{+0.40}_{-0.29}$	<i>u</i>	<i>Swift</i>	—
59409.45952	0.36451	$21.75^{+0.53}_{-0.36}$	<i>u</i>	<i>Swift</i>	—
59437.69981	0.27165	$21.57^{+0.45}_{-0.32}$	<i>u</i>	<i>Swift</i>	—
59470.18666	1.55946	$22.02^{+0.38}_{-0.28}$	<i>u</i>	<i>Swift</i>	—
59497.00830	0.96442	$21.88^{+0.32}_{-0.25}$	<i>u</i>	<i>Swift</i>	—
59528.82470	0.73400	> 21.19	<i>u</i>	<i>Swift</i>	—
59558.39374	0.36575	> 21.57	<i>u</i>	<i>Swift</i>	—
59582.28177	0.16837	> 21.06	<i>u</i>	<i>Swift</i>	—
59652.35462	2.48827	> 21.09	<i>u</i>	<i>Swift</i>	—
58758.67750	0.00092	$19.73^{+0.18}_{-0.15}$	<i>www1</i>	<i>Swift</i>	—
58760.43573	0.16809	$19.86^{+0.15}_{-0.13}$	<i>www1</i>	<i>Swift</i>	—
58766.12285	0.06463	$19.53^{+0.09}_{-0.08}$	<i>www1</i>	<i>Swift</i>	—
58773.25413	0.09856	$19.70^{+0.09}_{-0.08}$	<i>www1</i>	<i>Swift</i>	—

58780.16931	0.03486	19.79 ^{+0.10} _{-0.09}	ww1	Swift	-
58787.59735	0.10042	19.59 ^{+0.17} _{-0.14}	ww1	Swift	-
58791.14846	0.79706	19.79 ^{+0.10} _{-0.09}	ww1	Swift	-
58801.34097	0.29761	20.09 ^{+0.16} _{-0.14}	ww1	Swift	-
58808.93934	0.00058	19.73 ^{+0.31} _{-0.24}	ww1	Swift	-
58813.98795	0.00206	20.29 ^{+0.19} _{-0.16}	ww1	Swift	-
58814.26177	0.00254	20.39 ^{+0.17} _{-0.14}	ww1	Swift	-
58815.44657	0.00247	20.17 ^{+0.16} _{-0.14}	ww1	Swift	-
58815.57782	0.39932	20.38 ^{+0.20} _{-0.17}	ww1	Swift	-
58816.65269	0.00260	20.22 ^{+0.14} _{-0.13}	ww1	Swift	-
58817.31819	0.00238	20.45 ^{+0.18} _{-0.15}	ww1	Swift	-
58818.24210	0.00347	20.09 ^{+0.12} _{-0.11}	ww1	Swift	-
58819.29672	0.00301	20.30 ^{+0.16} _{-0.14}	ww1	Swift	-
58820.02573	0.00039	20.20 ^{+0.52} _{-0.35}	ww1	Swift	-
58820.10494	0.00173	19.94 ^{+0.15} _{-0.13}	ww1	Swift	-
58820.16116	0.00246	20.29 ^{+0.18} _{-0.15}	ww1	Swift	-
58820.23554	0.00308	20.27 ^{+0.14} _{-0.12}	ww1	Swift	-
58820.36324	0.00246	20.16 ^{+0.15} _{-0.13}	ww1	Swift	-
58820.43264	0.00321	20.28 ^{+0.14} _{-0.13}	ww1	Swift	-
58820.50219	0.00310	20.25 ^{+0.14} _{-0.12}	ww1	Swift	-
58820.56871	0.00325	20.31 ^{+0.14} _{-0.12}	ww1	Swift	-
58820.63438	0.00286	20.07 ^{+0.13} _{-0.11}	ww1	Swift	-
58820.70349	0.00319	20.37 ^{+0.14} _{-0.13}	ww1	Swift	-
58820.77275	0.00337	20.11 ^{+0.12} _{-0.11}	ww1	Swift	-
58820.82374	0.00238	20.23 ^{+0.19} _{-0.16}	ww1	Swift	-
58820.89275	0.00281	20.32 ^{+0.17} _{-0.15}	ww1	Swift	-
58820.97266	0.00276	20.35 ^{+0.15} _{-0.13}	ww1	Swift	-
58822.48634	0.47019	20.25 ^{+0.18} _{-0.16}	ww1	Swift	-
58829.19400	0.13366	19.88 ^{+0.11} _{-0.10}	ww1	Swift	-
58836.50128	0.39934	19.98 ^{+0.13} _{-0.12}	ww1	Swift	-
58843.44022	0.10179	19.78 ^{+0.10} _{-0.09}	ww1	Swift	-
58919.63779	0.33118	20.40 ^{+0.18} _{-0.15}	ww1	Swift	-
58921.29004	0.06790	20.26 ^{+0.14} _{-0.13}	ww1	Swift	-
58935.39729	0.29935	20.39 ^{+0.18} _{-0.16}	ww1	Swift	-
58942.17490	0.16380	20.53 ^{+0.18} _{-0.15}	ww1	Swift	-
58949.81187	0.02679	20.45 ^{+0.18} _{-0.15}	ww1	Swift	-
58956.57981	0.36292	20.50 ^{+0.15} _{-0.14}	ww1	Swift	-
58963.29305	0.10271	20.48 ^{+0.15} _{-0.14}	ww1	Swift	-
58970.36037	0.19883	20.44 ^{+0.16} _{-0.14}	ww1	Swift	-
58976.75324	0.03470	20.76 ^{+0.18} _{-0.15}	ww1	Swift	-
58977.82585	0.69438	20.80 ^{+0.19} _{-0.16}	ww1	Swift	-
58984.26318	0.09610	20.59 ^{+0.18} _{-0.15}	ww1	Swift	-
58990.80533	0.99678	20.55 ^{+0.13} _{-0.11}	ww1	Swift	-
58998.53726	0.30021	21.10 ^{+0.23} _{-0.19}	ww1	Swift	-
59005.58495	0.36272	20.73 ^{+0.17} _{-0.15}	ww1	Swift	-
59012.84003	0.13368	20.90 ^{+0.20} _{-0.17}	ww1	Swift	-
59019.29211	0.19832	20.66 ^{+0.19} _{-0.16}	ww1	Swift	-
59026.48801	0.36082	20.74 ^{+0.16} _{-0.14}	ww1	Swift	-
59034.82011	1.59784	21.30 ^{+0.27} _{-0.21}	ww1	Swift	-
59054.78212	0.23416	21.11 ^{+0.18} _{-0.16}	ww1	Swift	-
59060.65282	0.33879	20.85 ^{+0.22} _{-0.18}	ww1	Swift	-
59068.77368	0.43139	20.94 ^{+0.16} _{-0.14}	ww1	Swift	-
59074.99342	0.00055	21.21 ^{+0.74} _{-0.44}	ww1	Swift	-
59076.65677	0.53017	21.16 ^{+0.24} _{-0.20}	ww1	Swift	-
59081.69210	1.85407	21.37 ^{+0.32} _{-0.25}	ww1	Swift	-
59087.20066	1.59513	21.53 ^{+0.30} _{-0.24}	ww1	Swift	-
59091.79067	1.73007	21.78 ^{+0.43} _{-0.30}	ww1	Swift	-
59098.13274	0.83597	21.85 ^{+0.34} _{-0.26}	ww1	Swift	-
59102.45505	0.43266	21.39 ^{+0.24} _{-0.20}	ww1	Swift	-
59108.71275	0.00236	21.91 ^{+0.55} _{-0.36}	ww1	Swift	-
59116.48452	0.40641	21.60 ^{+0.31} _{-0.24}	ww1	Swift	-

59133.30700	0.30058	21.47 ^{+0.29} _{-0.23}	<i>ww1</i>	<i>Swift</i>	-
59153.34354	0.53637	21.78 ^{+0.48} _{-0.33}	<i>ww1</i>	<i>Swift</i>	-
59162.16404	0.67357	21.59 ^{+0.49} _{-0.37}	<i>ww1</i>	<i>Swift</i>	-
59166.83748	0.62911	21.14 ^{+0.37} _{-0.27}	<i>ww1</i>	<i>Swift</i>	-
59172.60940	0.36683	20.79 ^{+0.17} _{-0.15}	<i>ww1</i>	<i>Swift</i>	-
59186.69052	0.23950	21.13 ^{+0.26} _{-0.21}	<i>ww1</i>	<i>Swift</i>	-
59200.53435	0.26937	21.07 ^{+0.21} _{-0.17}	<i>ww1</i>	<i>Swift</i>	-
59214.24345	0.10235	21.98 ^{+0.45} _{-0.32}	<i>ww1</i>	<i>Swift</i>	-
59299.74679	2.61862	22.07 ^{+0.50} _{-0.34}	<i>ww1</i>	<i>Swift</i>	-
59325.78760	0.13541	21.88 ^{+0.34} _{-0.26}	<i>ww1</i>	<i>Swift</i>	-
59353.47348	0.46678	21.65 ^{+0.29} _{-0.23}	<i>ww1</i>	<i>Swift</i>	-
59381.97950	0.96170	22.04 ^{+0.33} _{-0.25}	<i>ww1</i>	<i>Swift</i>	-
59409.45753	0.36578	21.70 ^{+0.25} _{-0.20}	<i>ww1</i>	<i>Swift</i>	-
59437.69817	0.27220	22.15 ^{+0.38} _{-0.28}	<i>ww1</i>	<i>Swift</i>	-
59470.19564	1.55752	22.63 ^{+0.47} _{-0.33}	<i>ww1</i>	<i>Swift</i>	-
59497.01559	0.96466	22.32 ^{+0.31} _{-0.24}	<i>ww1</i>	<i>Swift</i>	-
59528.82910	0.73239	22.28 ^{+0.37} _{-0.27}	<i>ww1</i>	<i>Swift</i>	-
59558.40521	0.36809	22.55 ^{+0.44} _{-0.31}	<i>ww1</i>	<i>Swift</i>	-
59582.29516	0.16910	> 21.67	<i>ww1</i>	<i>Swift</i>	-
59652.36026	2.49039	22.21 ^{+0.58} _{-0.38}	<i>ww1</i>	<i>Swift</i>	-
59687.97614	2.89604	22.85 ^{+0.47} _{-0.33}	<i>ww1</i>	<i>Swift</i>	-
58758.68662	0.00146	19.78 ^{+0.16} _{-0.14}	<i>wvm2</i>	<i>Swift</i>	-
58760.44331	0.16753	19.98 ^{+0.14} _{-0.12}	<i>wvm2</i>	<i>Swift</i>	-
58766.12912	0.06645	19.85 ^{+0.09} _{-0.09}	<i>wvm2</i>	<i>Swift</i>	-
58773.26209	0.09667	19.86 ^{+0.09} _{-0.08}	<i>wvm2</i>	<i>Swift</i>	-
58780.16607	0.03485	19.81 ^{+0.11} _{-0.10}	<i>wvm2</i>	<i>Swift</i>	-
58787.60203	0.10049	20.13 ^{+0.18} _{-0.16}	<i>wvm2</i>	<i>Swift</i>	-
58791.15664	0.79587	20.00 ^{+0.10} _{-0.10}	<i>wvm2</i>	<i>Swift</i>	-
58801.08494	0.03633	19.87 ^{+0.14} _{-0.12}	<i>wvm2</i>	<i>Swift</i>	-
58808.94528	0.00098	21.03 ^{+0.47} _{-0.33}	<i>wvm2</i>	<i>Swift</i>	-
58815.55292	0.43501	20.41 ^{+0.12} _{-0.11}	<i>wvm2</i>	<i>Swift</i>	-
58822.49525	0.47185	20.47 ^{+0.12} _{-0.11}	<i>wvm2</i>	<i>Swift</i>	-
58829.20317	0.13267	20.17 ^{+0.10} _{-0.09}	<i>wvm2</i>	<i>Swift</i>	-
58836.51200	0.40023	20.17 ^{+0.11} _{-0.10}	<i>wvm2</i>	<i>Swift</i>	-
58843.44837	0.10067	19.78 ^{+0.09} _{-0.09}	<i>wvm2</i>	<i>Swift</i>	-
58919.64300	0.33311	20.43 ^{+0.10} _{-0.09}	<i>wvm2</i>	<i>Swift</i>	-
58921.29933	0.06915	20.44 ^{+0.10} _{-0.09}	<i>wvm2</i>	<i>Swift</i>	-
58935.40872	0.30211	20.33 ^{+0.09} _{-0.09}	<i>wvm2</i>	<i>Swift</i>	-
58942.15225	0.13567	20.45 ^{+0.12} _{-0.10}	<i>wvm2</i>	<i>Swift</i>	-
58956.58698	0.36066	20.39 ^{+0.09} _{-0.08}	<i>wvm2</i>	<i>Swift</i>	-
58963.30063	0.10048	20.48 ^{+0.11} _{-0.10}	<i>wvm2</i>	<i>Swift</i>	-
58970.36763	0.20086	20.57 ^{+0.11} _{-0.10}	<i>wvm2</i>	<i>Swift</i>	-
58976.76814	0.03506	20.56 ^{+0.15} _{-0.13}	<i>wvm2</i>	<i>Swift</i>	-
58977.83157	0.69593	20.54 ^{+0.10} _{-0.09}	<i>wvm2</i>	<i>Swift</i>	-
58984.30219	0.06350	20.79 ^{+0.23} _{-0.19}	<i>wvm2</i>	<i>Swift</i>	-
58990.81898	0.99880	20.61 ^{+0.12} _{-0.10}	<i>wvm2</i>	<i>Swift</i>	-
58998.55279	0.30110	21.01 ^{+0.19} _{-0.16}	<i>wvm2</i>	<i>Swift</i>	-
59005.58942	0.36238	20.74 ^{+0.16} _{-0.14}	<i>wvm2</i>	<i>Swift</i>	-
59012.85565	0.13504	20.95 ^{+0.17} _{-0.14}	<i>wvm2</i>	<i>Swift</i>	-
59019.30086	0.20025	21.38 ^{+0.28} _{-0.22}	<i>wvm2</i>	<i>Swift</i>	-
59026.49850	0.36580	20.90 ^{+0.16} _{-0.14}	<i>wvm2</i>	<i>Swift</i>	-
59034.82847	1.59347	20.92 ^{+0.23} _{-0.19}	<i>wvm2</i>	<i>Swift</i>	-
59054.79156	0.23455	20.92 ^{+0.14} _{-0.12}	<i>wvm2</i>	<i>Swift</i>	-
59060.66010	0.33961	21.50 ^{+0.30} _{-0.24}	<i>wvm2</i>	<i>Swift</i>	-
59071.67466	3.32505	21.33 ^{+0.16} _{-0.14}	<i>wvm2</i>	<i>Swift</i>	-
59076.66190	0.53018	21.58 ^{+0.26} _{-0.21}	<i>wvm2</i>	<i>Swift</i>	-
59081.69689	1.85421	21.64 ^{+0.32} _{-0.25}	<i>wvm2</i>	<i>Swift</i>	-
59087.21215	1.59173	22.09 ^{+0.40} _{-0.29}	<i>wvm2</i>	<i>Swift</i>	-
59091.80046	1.73398	22.05 ^{+0.42} _{-0.30}	<i>wvm2</i>	<i>Swift</i>	-
59097.90605	0.59922	21.79 ^{+0.28} _{-0.27}	<i>wvm2</i>	<i>Swift</i>	-
59102.46432	0.43261	22.13 ^{+0.41} _{-0.29}	<i>wvm2</i>	<i>Swift</i>	-

59116.48950	0.40605	21.53 ^{+0.21} _{-0.18}	wvm2	Swift	-
59133.31542	0.30166	22.33 ^{+0.37} _{-0.28}	wvm2	Swift	-
59152.84822	0.03621	21.57 ^{+0.39} _{-0.29}	wvm2	Swift	-
59162.16882	0.67464	21.61 ^{+0.30} _{-0.23}	wvm2	Swift	-
59166.84271	0.62784	21.23 ^{+0.29} _{-0.23}	wvm2	Swift	-
59172.61851	0.36384	21.00 ^{+0.14} _{-0.12}	wvm2	Swift	-
59186.69896	0.23547	21.35 ^{+0.18} _{-0.16}	wvm2	Swift	-
59200.54615	0.27300	21.35 ^{+0.19} _{-0.16}	wvm2	Swift	-
59214.25573	0.10301	21.17 ^{+0.15} _{-0.13}	wvm2	Swift	-
59300.14598	2.22525	21.83 ^{+0.25} _{-0.20}	wvm2	Swift	-
59325.79917	0.13317	> 22.15	wvm2	Swift	-
59353.48095	0.47361	22.24 ^{+0.37} _{-0.28}	wvm2	Swift	-
59381.98898	0.96766	21.71 ^{+0.22} _{-0.18}	wvm2	Swift	-
59409.46837	0.36189	22.17 ^{+0.28} _{-0.22}	wvm2	Swift	-
59437.70840	0.27254	21.99 ^{+0.23} _{-0.19}	wvm2	Swift	-
59470.19263	1.55814	22.34 ^{+0.32} _{-0.25}	wvm2	Swift	-
59497.01313	0.96454	22.01 ^{+0.22} _{-0.18}	wvm2	Swift	-
59528.82758	0.73287	22.55 ^{+0.44} _{-0.31}	wvm2	Swift	-
59558.40141	0.36732	22.32 ^{+0.29} _{-0.23}	wvm2	Swift	-
59582.29084	0.16900	22.25 ^{+0.38} _{-0.28}	wvm2	Swift	-
59652.35844	2.48974	22.76 ^{+0.53} _{-0.36}	wvm2	Swift	-
59687.97400	2.89505	22.64 ^{+0.25} _{-0.20}	wvm2	Swift	-
58758.68229	0.00185	20.03 ^{+0.13} _{-0.12}	wvw2	Swift	-
58760.43962	0.16831	19.92 ^{+0.09} _{-0.09}	wvw2	Swift	-
58766.12616	0.06593	19.78 ^{+0.07} _{-0.06}	wvw2	Swift	-
58773.25805	0.09806	19.82 ^{+0.06} _{-0.06}	wvw2	Swift	-
58780.12636	0.00158	19.87 ^{+0.13} _{-0.12}	wvw2	Swift	-
58787.59976	0.10073	20.12 ^{+0.14} _{-0.12}	wvw2	Swift	-
58791.15262	0.79701	20.16 ^{+0.08} _{-0.07}	wvw2	Swift	-
58801.34273	0.29700	20.24 ^{+0.12} _{-0.11}	wvw2	Swift	-
58808.94244	0.00117	20.42 ^{+0.23} _{-0.19}	wvw2	Swift	-
58815.54885	0.43442	20.59 ^{+0.10} _{-0.09}	wvw2	Swift	-
58822.49109	0.47167	20.53 ^{+0.10} _{-0.09}	wvw2	Swift	-
58829.19872	0.13380	20.29 ^{+0.08} _{-0.07}	wvw2	Swift	-
58836.50709	0.40073	20.18 ^{+0.08} _{-0.07}	wvw2	Swift	-
58843.44451	0.10191	20.01 ^{+0.07} _{-0.06}	wvw2	Swift	-
58919.64010	0.33196	20.51 ^{+0.12} _{-0.11}	wvw2	Swift	-
58921.29420	0.06836	20.40 ^{+0.10} _{-0.09}	wvw2	Swift	-
58935.40237	0.30045	20.37 ^{+0.11} _{-0.10}	wvw2	Swift	-
58942.17961	0.16597	20.75 ^{+0.12} _{-0.11}	wvw2	Swift	-
58949.84242	0.00200	20.66 ^{+0.20} _{-0.17}	wvw2	Swift	-
58956.58299	0.36177	20.62 ^{+0.11} _{-0.10}	wvw2	Swift	-
58963.29649	0.10165	20.37 ^{+0.10} _{-0.09}	wvw2	Swift	-
58970.36360	0.19962	20.56 ^{+0.12} _{-0.10}	wvw2	Swift	-
58976.76106	0.03602	20.75 ^{+0.11} _{-0.10}	wvw2	Swift	-
58977.82860	0.69519	20.70 ^{+0.12} _{-0.11}	wvw2	Swift	-
58984.26742	0.09564	21.01 ^{+0.15} _{-0.13}	wvw2	Swift	-
58990.81250	0.99873	20.76 ^{+0.09} _{-0.09}	wvw2	Swift	-
58998.54546	0.30185	21.01 ^{+0.12} _{-0.11}	wvw2	Swift	-
59005.58727	0.36286	20.87 ^{+0.12} _{-0.10}	wvw2	Swift	-
59012.84796	0.13523	21.12 ^{+0.13} _{-0.12}	wvw2	Swift	-
59019.29689	0.20001	20.85 ^{+0.13} _{-0.12}	wvw2	Swift	-
59026.49403	0.36433	20.91 ^{+0.11} _{-0.10}	wvw2	Swift	-
59034.82408	1.59610	21.01 ^{+0.17} _{-0.14}	wvw2	Swift	-
59054.78705	0.23502	21.33 ^{+0.13} _{-0.11}	wvw2	Swift	-
59060.65681	0.33985	21.28 ^{+0.16} _{-0.14}	wvw2	Swift	-
59071.67152	3.32593	21.50 ^{+0.13} _{-0.11}	wvw2	Swift	-
59076.65943	0.53051	21.37 ^{+0.15} _{-0.13}	wvw2	Swift	-
59081.69456	1.85442	21.50 ^{+0.19} _{-0.16}	wvw2	Swift	-
59087.20638	1.59420	21.55 ^{+0.18} _{-0.15}	wvw2	Swift	-
59091.79610	1.73284	21.63 ^{+0.19} _{-0.16}	wvw2	Swift	-

59098.13731	0.83602	$21.71^{+0.16}_{-0.14}$	<i>ww2</i>	<i>Swift</i>	—
59102.46004	0.43346	$21.79^{+0.17}_{-0.15}$	<i>ww2</i>	<i>Swift</i>	—
59108.72391	0.00390	$22.14^{+0.35}_{-0.26}$	<i>ww2</i>	<i>Swift</i>	—
59116.48706	0.40654	$21.73^{+0.17}_{-0.15}$	<i>ww2</i>	<i>Swift</i>	—
59133.31149	0.30176	$21.85^{+0.17}_{-0.15}$	<i>ww2</i>	<i>Swift</i>	—
59153.34655	0.53719	$21.61^{+0.23}_{-0.19}$	<i>ww2</i>	<i>Swift</i>	—
59162.16675	0.67457	$21.50^{+0.20}_{-0.17}$	<i>ww2</i>	<i>Swift</i>	—
59166.84007	0.62876	$21.36^{+0.22}_{-0.18}$	<i>ww2</i>	<i>Swift</i>	—
59172.61395	0.36597	$21.14^{+0.11}_{-0.12}$	<i>ww2</i>	<i>Swift</i>	—
59186.69458	0.23797	$21.19^{+0.12}_{-0.11}$	<i>ww2</i>	<i>Swift</i>	—
59200.54155	0.27290	$21.25^{+0.11}_{-0.10}$	<i>ww2</i>	<i>Swift</i>	—
59214.25004	0.10372	$21.37^{+0.12}_{-0.11}$	<i>ww2</i>	<i>Swift</i>	—
59299.75095	2.61782	$22.15^{+0.26}_{-0.21}$	<i>ww2</i>	<i>Swift</i>	—
59325.79343	0.13505	$22.08^{+0.21}_{-0.17}$	<i>ww2</i>	<i>Swift</i>	—
59353.47849	0.47154	$22.06^{+0.23}_{-0.19}$	<i>ww2</i>	<i>Swift</i>	—
59381.98494	0.96554	$22.37^{+0.26}_{-0.21}$	<i>ww2</i>	<i>Swift</i>	—
59409.46290	0.36455	$22.27^{+0.20}_{-0.17}$	<i>ww2</i>	<i>Swift</i>	—
59437.70360	0.27319	$22.24^{+0.19}_{-0.16}$	<i>ww2</i>	<i>Swift</i>	—
59470.18966	1.55880	$22.51^{+0.29}_{-0.23}$	<i>ww2</i>	<i>Swift</i>	—
59497.01072	0.96448	$22.68^{+0.30}_{-0.24}$	<i>ww2</i>	<i>Swift</i>	—
59528.82616	0.73344	$22.55^{+0.35}_{-0.27}$	<i>ww2</i>	<i>Swift</i>	—
59558.39759	0.36654	$22.29^{+0.24}_{-0.20}$	<i>ww2</i>	<i>Swift</i>	—
59582.28632	0.16869	$22.32^{+0.34}_{-0.26}$	<i>ww2</i>	<i>Swift</i>	—
59652.35654	2.48900	$22.85^{+0.58}_{-0.38}$	<i>ww2</i>	<i>Swift</i>	—
59687.97175	2.89395	$22.60^{+0.20}_{-0.17}$	<i>ww2</i>	<i>Swift</i>	—
59169.23517	0.0136	21.86 ± 0.24	F169M	<i>AstroSat</i>	—
59176.60971	0.0111	21.72 ± 0.25	F169M	<i>AstroSat</i>	—
59192.51029	0.0114	22.15 ± 0.30	F169M	<i>AstroSat</i>	—
59176.67736	0.0132	21.84 ± 0.40	F172M	<i>AstroSat</i>	—
59192.64563	0.0113	22.07 ± 0.49	F172M	<i>AstroSat</i>	—
55324.99868	0.62841	16.83 ± 0.15	W1	<i>WISE</i>	—
55504.33386	0.56214	16.87 ± 0.14	W1	<i>WISE</i>	—
56787.28494	0.55940	16.90 ± 0.21	W1	<i>WISE</i>	—
57966.78907	280.142	16.70 ± 0.29	W1	<i>WISE</i>	—
58409.98672	1.93012	16.69 ± 0.16	W1	<i>WISE</i>	—
58611.61711	0.62147	16.39 ± 0.26	W1	<i>WISE</i>	—
58775.56522	0.49063	15.72 ± 0.18	W1	<i>WISE</i>	—
58975.75518	0.55583	16.00 ± 0.20	W1	<i>WISE</i>	—
59143.18162	4.08684	16.20 ± 0.29	W1	<i>WISE</i>	—
59506.69516	0.62078	16.54 ± 0.25	W1	<i>WISE</i>	—
56055.67957	731.3093	16.61 ± 0.30	W2	<i>WISE</i>	—
58775.56522	0.49063	15.16 ± 0.21	W2	<i>WISE</i>	—
56915.14	—	22.82 ± 0.07	g	DES	—
57656.10	—	22.68 ± 0.05	g	DES	—
56915.14	—	22.80 ± 0.07	g	DES	—
56924.12	—	22.70 ± 0.05	g	DES	—
57283.16	—	22.87 ± 0.08	g	DES	—
56953.18	—	22.97 ± 0.09	g	DES	—
56953.18	—	22.95 ± 0.09	g	DES	—
57251.23	—	23.06 ± 0.12	g	DES	—
56924.12	—	22.71 ± 0.05	g	DES	—
58758.9588	—	19.60	g	<i>J-GEM</i>	GCN 25941
58787.06513	0.00510	19.38 ± 0.09	g'	<i>GROND</i>	—
59428.17707	0.00898	21.07 ± 0.08	g'	<i>GROND</i>	—
59430.16758	0.00898	21.05 ± 0.07	g'	<i>GROND</i>	—
59438.34115	0.00409	21.18 ± 0.06	g'	<i>GROND</i>	—
59470.14427	0.00394	21.24 ± 0.06	g'	<i>GROND</i>	—
59498.01320	0.00890	21.14 ± 0.04	g'	<i>GROND</i>	—
59529.02932	0.00902	21.22 ± 0.05	g'	<i>GROND</i>	—
59558.03155	0.00406	21.08 ± 0.10	g'	<i>GROND</i>	—
59725.33557	0.00895	21.27 ± 0.08	g'	<i>GROND</i>	—

57283.15	–	21.20 ± 0.09	r	DES	–
57656.10	–	21.19 ± 0.05	r	DES	–
56926.11	–	21.22 ± 0.05	r	DES	–
56888.22	–	21.25 ± 0.05	r	DES	–
56926.11	–	21.22 ± 0.05	r	DES	–
56888.22	–	21.25 ± 0.09	r	DES	–
56924.12	–	21.21 ± 0.02	r	DES	–
56898.18	–	20.94 ± 0.09	r	DES	–
56924.12	–	21.22 ± 0.02	r	DES	–
56898.18	–	20.95 ± 0.09	r	DES	–
58758.9588	–	19.30	r	<i>J-GEM</i>	GCN 25941
58761.19808	0.031	19.35 ± 0.06	r	<i>Chilescope</i>	GCN 25963
58787.06436	0.00433	19.58 ± 0.03	r'	<i>GROND</i>	–
59428.17707	0.00898	20.79 ± 0.01	r'	<i>GROND</i>	–
59430.16758	0.00898	20.76 ± 0.03	r'	<i>GROND</i>	–
59438.34115	0.00409	20.83 ± 0.04	r'	<i>GROND</i>	–
59470.14427	0.00394	20.88 ± 0.04	r'	<i>GROND</i>	–
59498.01320	0.00890	20.78 ± 0.03	r'	<i>GROND</i>	–
59529.02932	0.00902	20.82 ± 0.03	r'	<i>GROND</i>	–
59558.03155	0.00406	20.86 ± 0.06	r'	<i>GROND</i>	–
59725.33557	0.00895	20.91 ± 0.03	r'	<i>GROND</i>	–
58429.09	–	20.59 ± 0.03	i	DES	–
56927.12	–	20.61 ± 0.03	i	DES	–
56927.12	–	20.61 ± 0.03	i	DES	–
56916.13	–	20.61 ± 0.04	i	DES	–
56924.12	–	20.63 ± 0.04	i	DES	–
57656.10	–	20.61 ± 0.03	i	DES	–
56924.12	–	20.63 ± 0.03	i	DES	–
56916.13	–	20.61 ± 0.04	i	DES	–
57299.10	–	20.63 ± 0.05	i	DES	–
58758.9588	–	19.30	i	<i>J-GEM</i>	GCN 25941
58787.06436	0.00433	19.37 ± 0.03	i'	<i>GROND</i>	–
59428.17707	0.00898	20.26 ± 0.01	i'	<i>GROND</i>	–
59430.16758	0.00898	20.25 ± 0.03	i'	<i>GROND</i>	–
59438.34115	0.00409	20.25 ± 0.05	i'	<i>GROND</i>	–
59470.14427	0.00394	20.35 ± 0.04	i'	<i>GROND</i>	–
59498.01320	0.00890	20.26 ± 0.03	i'	<i>GROND</i>	–
59529.02932	0.00902	20.28 ± 0.04	i'	<i>GROND</i>	–
59558.03155	0.00406	20.16 ± 0.06	i'	<i>GROND</i>	–
59725.33557	0.00895	20.35 ± 0.04	i'	<i>GROND</i>	–
56886.23	–	20.34 ± 0.04	z	DES	–
57643.17	–	20.34 ± 0.04	z	DES	–
57294.11	–	20.36 ± 0.04	z	DES	–
56886.23	–	20.34 ± 0.04	z	DES	–
56904.16	–	20.27 ± 0.03	z	DES	–
56932.15	–	20.32 ± 0.04	z	DES	–
56904.16	–	20.27 ± 0.03	z	DES	–
56932.15	–	20.32 ± 0.04	z	DES	–
58409.03	–	20.33 ± 0.03	z	DES	–
58787.06436	0.00433	19.29 ± 0.04	z'	<i>GROND</i>	–
59428.17707	0.00898	20.09 ± 0.02	z'	<i>GROND</i>	–
59430.16758	0.00898	20.04 ± 0.02	z'	<i>GROND</i>	–
59438.34115	0.00409	20.07 ± 0.06	z'	<i>GROND</i>	–
59470.14427	0.00394	20.08 ± 0.04	z'	<i>GROND</i>	–
59498.01320	0.00890	20.00 ± 0.07	z'	<i>GROND</i>	–
59529.02932	0.00902	20.12 ± 0.03	z'	<i>GROND</i>	–
59725.33557	0.00895	20.18 ± 0.03	z'	<i>GROND</i>	–
56931.12	–	20.18 ± 0.07	Y	DES	–
57291.09	–	20.26 ± 0.09	Y	DES	–
57999.12	–	20.40 ± 0.14	Y	DES	–
57286.11	–	20.28 ± 0.21	Y	DES	–
56886.23	–	20.28 ± 0.10	Y	DES	–

57288.11	–	20.39 ± 0.40	Y	DES	–
57293.10	–	20.09 ± 0.07	Y	DES	–
58787.06541	0.00537	19.19 ± 0.08	J	<i>GROND</i>	–
59428.17707	0.00898	19.80 ± 0.07	J	<i>GROND</i>	–
59430.16758	0.00898	19.79 ± 0.09	J	<i>GROND</i>	–
59438.34137	0.00430	19.71 ± 0.12	J	<i>GROND</i>	–
59470.14448	0.00414	20.13 ± 0.15	J	<i>GROND</i>	–
59498.01340	0.00907	19.84 ± 0.10	J	<i>GROND</i>	–
59529.02953	0.00921	20.00 ± 0.12	J	<i>GROND</i>	–
59558.03179	0.00425	20.40 ± 0.30	J	<i>GROND</i>	–
59725.33575	0.00914	19.74 ± 0.10	J	<i>GROND</i>	–
58787.06541	0.00537	18.86 ± 0.10	H	<i>GROND</i>	–
59430.16758	0.00898	19.27 ± 0.09	H	<i>GROND</i>	–
59438.34137	0.00430	19.21 ± 0.13	H	<i>GROND</i>	–
59470.14448	0.00414	19.34 ± 0.12	H	<i>GROND</i>	–
59529.02953	0.00921	19.55 ± 0.13	H	<i>GROND</i>	–
59558.03179	0.00425	19.42 ± 0.18	H	<i>GROND</i>	–
59725.33575	0.00914	19.48 ± 0.12	H	<i>GROND</i>	–
58787.06464	0.00460	18.69 ± 0.19	K	<i>GROND</i>	–
59428.17707	0.00898	19.56 ± 0.34	K	<i>GROND</i>	–
59430.16778	0.00917	19.82 ± 0.47	K	<i>GROND</i>	–
59438.34137	0.00430	19.42 ± 0.34	K	<i>GROND</i>	–
59470.14448	0.00414	18.95 ± 0.18	K	<i>GROND</i>	–
59498.01340	0.00907	19.17 ± 0.21	K	<i>GROND</i>	–
59529.02953	0.00921	19.45 ± 0.31	K	<i>GROND</i>	–
59725.33575	0.00914	19.30 ± 0.21	K	<i>GROND</i>	–